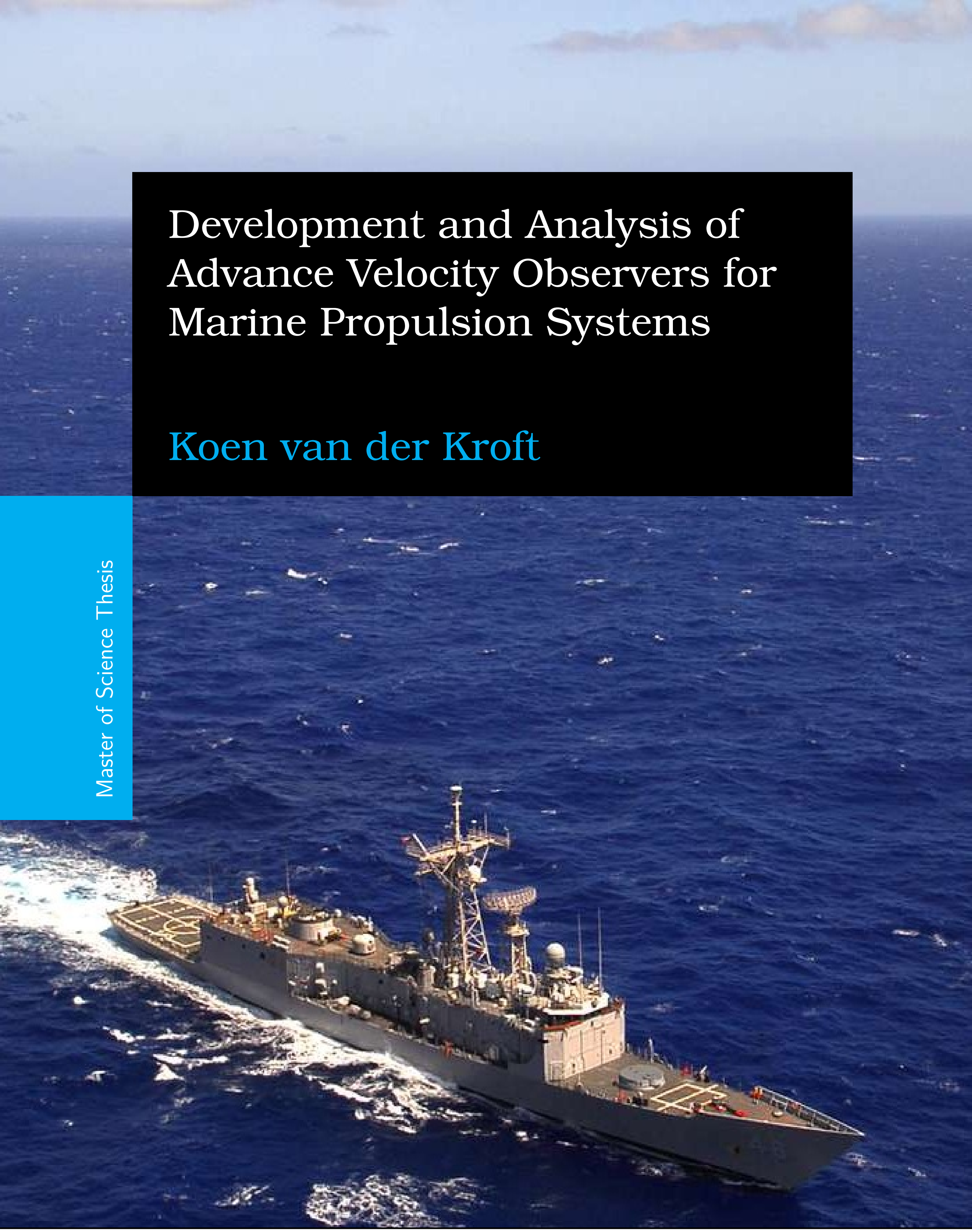

Development and Analysis of Advance Velocity Observers for Marine Propulsion Systems

Koen van der Kroft

Master of Science Thesis

Delft University of Technology

Delft Center for Systems and Control

Development and Analysis of Advance Velocity Observers for Marine Propulsion Systems

MASTER OF SCIENCE THESIS

For the degree of Master of Science in Systems and Control at Delft University of Technology

Koen van der Kroft

February 7, 2020

UNDER EMBARGO

Faculty of Mechanical, Maritime and Materials Engineering (3mE) · Delft University of Technology

Cover: Michael N. Tialemasunu 2009, The Oliver Hazard Perry-class frigate USS Rentz (FFG 46) participates in the Undersea Warfare Exercise (USWEX 09), U.S. Navy

Abstract

Marine propulsion systems with diesel engines face continuous variations in propeller shaft speed and torque during operation, due to waves and changing rudder and water inflow angles. Traditional propulsion control systems do not take these variations into account, and attempt to maintain a constant shaft speed. These changing torques, in combination with inefficient control efforts, can increase mechanical wear and tear on the diesel engine, and reduce efficiency. More advanced control algorithms relying on the axial flow velocity of water through the propeller have shown great promise. Unfortunately, this velocity, also known as the advance velocity, is very difficult or impossible to measure. Therefore, it is possible to use state observers to estimate the advance velocity using available measurements of shaft speed and torque. However, the current state of the art regarding advance velocity estimation is very limited.

In this paper, a complete model of a ship propulsion system is created. Several different observer structures are applied to the propulsion model to estimate the advance velocity. These include a Luenberger observer, a Shaft Kalman Filter (SKF), a Power Balance Estimator (PBE), a Measured Shaft Acceleration (MSA) observer with and without measurements of shaft acceleration, an Immersion and Invariance (I&I) observer and a Random Walk Kalman Filter (RWKF). The performance of these advance velocity observers using different observer gains is compared using several load cases. These load cases are used to assess time domain accuracy with and without measurement noise, and robustness to errors in a priori information regarding the propulsion system.

The findings indicate a clear trade off between noiseless accuracy, and robustness to noise. If an observer has high observer gains, it is more accurate when no noise is present, but more sensitive to measurement noise, and vice versa. Furthermore, higher gains also lead to more robustness to errors in a priori information. The errors that lead to the most significant estimation errors were errors in the Open Water Propeller Diagrams (OWPD), with errors in the shaft inertia proving to be much less significant. That being said, if accurate shaft acceleration is available, the MSA observer is most effective. If this data is unavailable or inaccurate, a choice must be made. If measurement noise robustness is paramount, the RWKF or an I&I observer with low gains is most effective. If absolute accuracy is most important, and the measured variables are virtually free of noise, an I&I observer with high gains is the best choice. The RWKF provided a very good compromise between noise robustness and noiseless accuracy, but requires a large amount of a priori information.

Suggestions for future research include testing the observers in both cavitation tunnels and full scale propulsion systems, and implementing multivariable propulsion control using the estimated advance velocity.

Table of Contents

List of Figures

List of Tables

Preface

This thesis is the final part of the Master of Science programme "Systems and Control" at the Delft University of Technology. The presented work is a combined effort of the Delft Center for Systems and Control (DCSC) and the Department of Maritime and Transport Technology (M&TT), at the faculty of Mechanical, Maritime and Materials Engineering (3mE).

The thesis committee consists of the following members:

- Prof. dr. ir. J.W. van Wingerden
- Dr. ir. A. Vrijdag
- Ir. D.C. van der Hoek
- Ir. L.J.G. Huijgens

I would like to take this opportunity to thank my family and friends for their support, feedback, criticism and encouragement during the creation of this thesis. Furthermore, I would like to explicitly state my gratitude towards Arthur Vrijdag and Jan-Willem van Wingerden, who were always ready and willing to provide valuable guidance and feedback. Their support has greatly improved both the quality of the presented work and my personal experience writing this thesis.

Delft, University of Technology
February 7, 2020

Koen van der Kroft

Chapter 1

Introduction

Traditionally, the speed of diesel powered ships with Fixed Pitch Propellers (FPP) has been controlled in a simple manner; the desired propeller shaft speed is set at the bridge, and maintained by an engine speed governor. This engine speed governor observes the error between the desired shaft speed and the measured shaft speed, and uses a PID controller to determine the input to the diesel engine, being the fuel rack position [2][3][4]. Although simple and effective, this method of controlling the ship speed has certain drawbacks. The shaft speed is constantly changing, due to waves, changing rudder angles and a constantly varying angle of the propeller with respect to the water. It is even possible for waves to become extreme enough to partially or completely lift the propeller out of the water, resulting in propeller ventilation. This propeller ventilation results in partial or complete loss of thrust and load torque. These variations in shaft speed and torque can put large strains on a diesel engine through thermal overloading [4][5][6][7][8]. This is especially true if an engine governor is attempting to reject the disturbances on the shaft speed, and keep the shaft speed constant [2][4][7][9]. Stapersma et al. (2004) stated that PID shaft speed control is at risk of over-fueling the engine, which leads to increased mechanical wear and tear on the diesel engine. Increased mechanical wear and tear means the time between engine overhauls is decreased, leading to more expensive and less efficient operation.

If the ship is equipped with a Controllable Pitch Propeller (CPP), the control efforts become more convoluted. This is due to the fact that the system now contains two inputs, being the fuel rack position of the diesel engine and the pitch of the propeller. The traditional manner of controlling this multivariable system is the combinator curve. This is a curve with fixed combinations of propeller pitch and shaft speed, based on different power levels [2][10][11]. The power level is set at the bridge, and the propeller pitch and shaft speed are obtained from the combinator curve. Again, a PID controller is used to maintain the shaft speed as commanded by the combinator curve. Although this provides a simple form of multivariable control, this form of ship speed control also contains several downsides. For one, since the PID shaft speed controller is still being used, this form of control could also lead to diesel engine overloading. Furthermore, there are many different combinations of propeller pitch and shaft speed that lead to the same ship speed. Some of these are more efficient than others. By definition, the combinator curve only considers one combination of shaft speed and propeller pitch for a certain power level [10]. This could lead to inefficiencies and conservative control, since the combinator curve significantly limits control freedom [11][12]. Furthermore, the use of a combinator curve could lead to poor propeller cavitation behaviour, since the combinator curve does not take into account the propeller inflow angle.

In order to solve these problems, the field of marine propulsion has shown an increasing interest in control theory. In particular, advance velocity observers have been the subject of research. The advance velocity of a propeller is the axial speed of the water through the propeller disk. The operation of the propeller is greatly dependent on this variable. Unfortunately, the advance velocity is difficult or impossible to measure without cumbersome and expensive additional instrumentation, according to Whitcomb et al. (1999). To this end, state observers can be used. State observers are algorithms from the field of control theory. These algorithms use sensor data of the system to obtain estimates of variables that are impossible or difficult to measure. In this case, measurements of e.g. shaft speed and torque could be used to estimate the advance velocity.

Smogeli et al. (2006) have found that new control strategies involving advance velocity observers have the potential to increase thrust, reduce mechanical wear and tear and limit power transients. Smogeli et al. (2004) have successfully applied an advance velocity observer to a propulsion system. This observer used measurements of shaft speed and torque to estimate the propeller torque and advance velocity. To this end, a Luenberger observer was used with a first order Markov process to model the unknown propeller torque. Furthermore, this paper describes several control schemes to improve system performance, all using the observed advance velocity. Unfortunately, this was only performed for Fixed Pitch Propellers (FPP), but the theory could be extended to CPP.

Guibert et al. (2005) applied an Extended Kalman Filter to a propulsion system with electric motors instead of diesel engines. Again, measurements of shaft speed and torque were used, and an estimate of the advance velocity was obtained. Furthermore, several promising control schemes were implemented, again all based on the estimated advance velocity. Although this research was performed for Fixed Pitch Propellers and electric motors, the theory could be extended to CPP and diesel engines.

Bakkeheim et al. (2007) implemented a Luenberger observer similar to the observer designed in Smogeli et al. (2004), and used the estimated advance velocity to calculate the torque losses in the propeller. The estimated torque loss was then used for a reference generator, to generate a reference signal for a PID shaft speed controller. This ensured that, for instance, when propeller ventilation occurred, the desired shaft speed could be adjusted. This could reduce the effect of engine overloading when propeller ventilation occurs. Again, this was performed for electric motors and FPP, but an extension could be made to CPP and diesel engines.

The problem of advance velocity estimation is not unique to the field of marine propulsion systems. Many of the same challenges exist in the field of wind turbines. As shown in Ostergaard et al. (2007), the modeling required for wind turbines is largely identical to the modeling for ship propulsion systems. Similar to marine propulsion systems, in wind turbine systems the advance velocity (also known as "effective wind speed") is a critical parameter, that describes the operation of the turbine. Soltani et al. (2013) states that although there is a wind speed sensor on top of the turbine nacelle, it is not advised to use this for the effective wind speed measurement. They state that this is due to the fact that this sensor provides a point measurement, and it is heavily disturbed by the turbine itself. The similarities between the modeling required and the problems faced in wind turbine systems and ship propulsion systems, means that it is possible to apply effective wind speed estimation techniques to advance velocity estimation problems.

Ortega et al. (2012) applied an Immersion and Invariance (I&I) observer to a wind turbine system. This observer uses a scaled shaft speed, and a single tuning gain. This makes the observer very easy to tune when compared to a Kalman Filter or a Luenberger observer. This observer structure provided very promising results, and could be applied to marine propulsion systems.

Selvam et al. (2009) applied a Kalman Filter with a discrete Random Walk model to a wind turbine system. This revolutionary observer structure provided promising results. In this paper, it was applied in combination with individual pitch control, to reduce the load on the wind turbine blades and tower. Unfortunately, individual pitch control is not possible for most Controllable Pitch Propellers, but nonetheless, the observer structure could be applied to ship propulsion systems.

Concluding, the application of advance velocity observers has been studied in the fields of both marine propulsion and wind turbine systems. However, no effective application of advance velocity observers to marine propulsion systems with Controllable Pitch Propellers has been found in the literature. Furthermore, the applied observers are limited to Luenberger observers and Kalman Filters. Moreover, several promising observer structures have been applied in the field of wind turbine systems, which could be also applied to ship propulsion systems.

The fact that advanced control schemes relying on the advance velocity show great promise, combined with the fact that only simple advance velocity estimation has been applied to Fixed Pitch Propellers, has lead to the following research question:

What is the most effective observer structure for estimating the advance velocity of a marine propulsion system with a controllable pitch propeller?

Next, the scope of the research will be defined. This thesis will only focus on marine propulsion systems with a diesel engine and a Controllable Pitch Propeller. No electric motors or Fixed Pitch Propellers will be considered. Only conventional Controllable Pitch Propellers will be examined, meaning no waterjets, thrusters or Voith-Schneider propellers are covered in this thesis. The CPP is assumed to be functioning in the first quadrant at all times, meaning the shaft speed and advance velocity will always remain positive. Furthermore, no propeller ventilation will be regarded; the entire propeller will remain submerged at all times. Since the hydrodynamic effects of the rudder on the propeller are extremely complex, only axial disturbances in the advance velocity and in the ship resistance will be considered. Finally, this thesis will focus only on the synthesis and evaluation of advance velocity observers. No control will be applied.

1-1 Thesis Outline

Chapter 2 will cover the modeling of the ship propulsion system. This includes the modeling of all components of the plant, including but not limited to the propeller, engine, gearbox and ship resistance. Furthermore, this chapter contains the linearization of the non-linear marine propulsion plant. After the linearization, the linearized plant will be analyzed in the frequency domain, and verified using an existing model.

Chapter 3 will focus on the synthesis of different types of advance velocity observers. This includes the following observer structures: Luenberger Observer, Shaft Kalman Filter, Power Balance Estimator, Measured Shaft Acceleration Observer, I&I observer and Random Walk Kalman Filter (RWKF). For each observer structure, the method, properties and tuning will be discussed. Also, each observer will be analyzed in the frequency domain.

Chapter 4 will cover the performance of the observers in the time domain. Several different load cases are presented, and each observer will be subjected to different inputs and disturbances. In this chapter, a juxtaposition of the performance of the observers is shown, in order to determine the strengths and weaknesses of each observer structure.

Chapter 5 will contain the Observer Sensitivity Analysis. In this chapter, several errors are introduced in the models used by the observers. The different errors will lead to inaccuracies, and the sensitivity of the different observers to these errors will be assessed.

Finally, Chapter 6 will contain the Conclusion and offer suggestions for future research in the Recommendations.

Chapter 2

Modeling

Before any observer synthesis can be performed, first a model of the system must be created. In order to obtain a clear representation of the system without influences from control, the uncontrolled plant will be modeled. After this, different observers can be applied. In this chapter, the modeling of the uncontrolled plant will be covered. Figure 2-1 shows a schematic of the propulsion system:

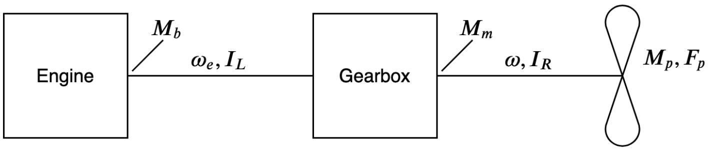

Figure 2-1: Schematic of propulsion system

This shows the engine, connected by a shaft to the gearbox, which is connected to the propeller by a second shaft. Figure 2-1 also shows the symbol conventions which will be used throughout the thesis. In order to give an overview of the model, Figure 2-2 shows the block diagram of the ship propulsion model, including the interconnections between the different elements of the system.

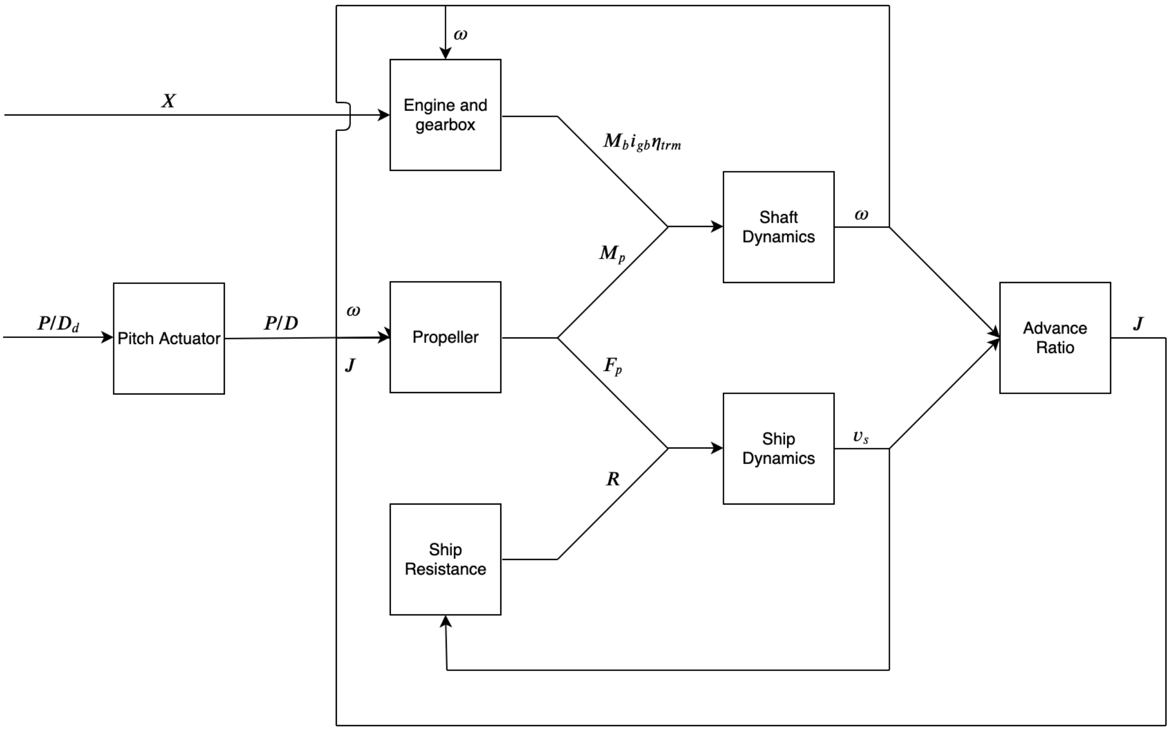

Figure 2-2: Block diagram of ship propulsion system

In the following sections, the individual elements of the system will be highlighted. Firstly, the differential equations will be described in Section 2-1. Secondly, the propeller will be discussed in Section 2-2. Next, in Section 2-3, the ship resistance is modeled. Section 2-4 covers the modeling of the engine and gearbox. In Section 2-5, the measurements of shaft torque are explained. After the individual elements have been discussed, Section 2-6 combines the elements into one model, which is linearized in Section 2-7. Finally, Section 2-8 provides a verification of the created model.

2-1 Differential Equations

In essence, the ship propulsion system consists of two differential equations. One describes the motion of the propeller shaft, and the other describes the translating motion of the ship itself. The motion of the propeller shaft is described by the following differential equation [1][3][20]:

$$\dot{\omega} = \frac{M_b i_{gb} \eta_{trm} - M_p}{I} \tag{2-1}$$

Here, ω describes the shaft speed, such that $\dot{\omega}$ describes the shaft acceleration. M_b is the brake engine torque, and M_p is the torque required by the propeller. i_{gb} describes the gearbox ratio, and η_{trm} is the transmission efficiency. These are further explained in Section 2-4. I is the rotational moment of inertia of the shaft. This equation is defined where the propeller is attached to the shaft, after the gearbox, as seen in Figure 2-1. The second differential equation describes the translation of the ship itself [11][20][21][22][23][24][25]:

$$\dot{v}_s = \frac{F_p - R}{m_s} \tag{2-2}$$

Here, v_s describes the ship speed, F_p is the thrust delivered by the propeller(s) and R is the resistance on the ship imposed by the water. m_s is the mass of the ship, including added mass (mass of water being dragged behind ship). In the next section, the different elements that provide the terms for these differential equations will be highlighted.

2-2 Propeller

The first element of the ship propulsion system that will be highlighted is the propeller. The propeller is perhaps the most important part of the system, transforming rotating motion into thrust. In order to model the behavior of the propeller, the Open Water Propeller Diagrams (OWPD) are used in conjunction with several equations, which will be examined first. The first two equations describe the propeller torque and thrust, based on the shaft speed [4][20][26]:

$$Q = \rho D^5 \left(\frac{\omega}{2\pi}\right)^2 K_Q(J(\omega, v_a), {}^P\!/\!{}_D) \tag{2-3}$$

$$T = \rho D^4 \left(\frac{\omega}{2\pi}\right)^2 K_T(J(\omega, v_a), {}^P\!/\!{}_D) \tag{2-4}$$

Here, Q describes the open water torque of one propeller. This must be adjusted to the actual "in-behind" torque using the relative rotative efficiency. T describes the open water thrust provided by one propeller. In order to adjust this to the actual "in-behind" thrust of multiple propellers, this thrust must be multiplied by both the thrust deduction factor and the number of propellers [11]. This leads to the following equations:

$$M_p = \rho D^5 \left(\frac{\omega}{2\pi}\right)^2 K_Q(J(\omega, v_a), {}^P\!/\!{}_D)\eta_r^{-1} \tag{2-5}$$

$$F_p = \rho D^4 \left(\frac{\omega}{2\pi}\right)^2 K_T(J(\omega, v_a), {}^P\!/\!{}_D)k_p(1-t) \tag{2-6}$$

In these equations, ρ is the density of water, D is the diameter of the propeller. k_p describes the number of propellers. t is the thrust deduction factor, which describes how much thrust is lost due to the fact that the propeller creates suction, pulling on the hull. η_r describes the relative rotative efficiency, which indicates the change of propeller torque when the propeller is operated in a real scenario instead of during the open water tests, also known as "in-behind". K_Q and K_T are the propeller torque and thrust coefficients, respectively. The torque and thrust coefficient describe the behavior of the propeller as a function of J, the advance ratio, and the propeller pitch ratio ${}^P\!/\!{}_D$. The propeller pitch ratio describes the ratio between the pitch of the propeller blades and the propeller diameter. The advance ratio J is a measure that describes how much the propeller moves forward for each revolution, and is calculated as follows [3]:

$$J(\omega, v_a) = \frac{2\pi v_a}{\omega D} \tag{2-7}$$

Here, v_a is the advance velocity, which describes the velocity of the water through the propeller blades. This is not always identical to the ship speed, since the wake behind the ship and the movement of the water can change the advance velocity. In this thesis, only the axial component of the advance velocity with respect to the propeller is taken into account. It is possible for the advance velocity to enter the propeller disk at an angle, but modeling this is outside the scope of this thesis. A simple way to model the advance velocity is to use the wake fraction w. This fraction describes a linear relation between the ship speed and the advance velocity [20]:

$$v_a = (1 - w)v_s + u_x \tag{2-8}$$

Here, u_x is a disturbance that is applied to the advance velocity. This is introduced to account for disturbances in the advance velocity due to e.g. waves. Once the advance ratio and pitch ratio are known, it is possible to determine the propeller torque and thrust coefficients by using the open water propeller diagrams. This allows the propeller torque and thrust to be calculated.

If the propeller is a Controllable Pitch Propeller (CPP), the pitch of the propeller can be adjusted using a hydraulic actuating mechanism. In order to model the behavior of the pitch actuation mechanism, a simple first-order model is used [1][11][12][22][27]:

$$\dot{{}^{P}\!/_{D}} = \frac{1}{\tau_p}({}^{P}\!/_{D_d} - {}^{P}\!/_{D}) \tag{2-9}$$

Here, ${}^{P}\!/_{D_d}$ is the desired propeller pitch ratio, and τ_p is the time constant of the pitch actuator, determining how quick the response of the first-order system is. This covers the modeling of the propeller.

2-3 Ship resistance

This section covers the modeling of the resistance of the ship. As the ship moves through the water, the water in front of the ship must be pushed aside, which requires a force. Furthermore, the water runs along the side of the hull as the ship moves, creating drag. In order to keep the model simple, the resistance is modeled using a quadratic relation with the ship speed [25]:

$$R = d_{c_1} c_1 v_s^2 \tag{2-10}$$

Here, c_1 is the quadratic resistance coefficient. d_{c_1} is a factor describing the disturbance on the ship resistance. This can be used to model a static and/or dynamic resistance disturbance.

2-4 Engine & Gearbox

This section covers the modeling of the engine and gearbox. The choice was made to model a diesel engine, due to the overloading problems stated in Section 1. Figure 2-3 shows a typical fuel rack map for a diesel engine. This map gives the brake engine torque delivered by the engine, as a function of the fuel rack position and the engine speed. The thick black lines indicate the operating limits of the engine.

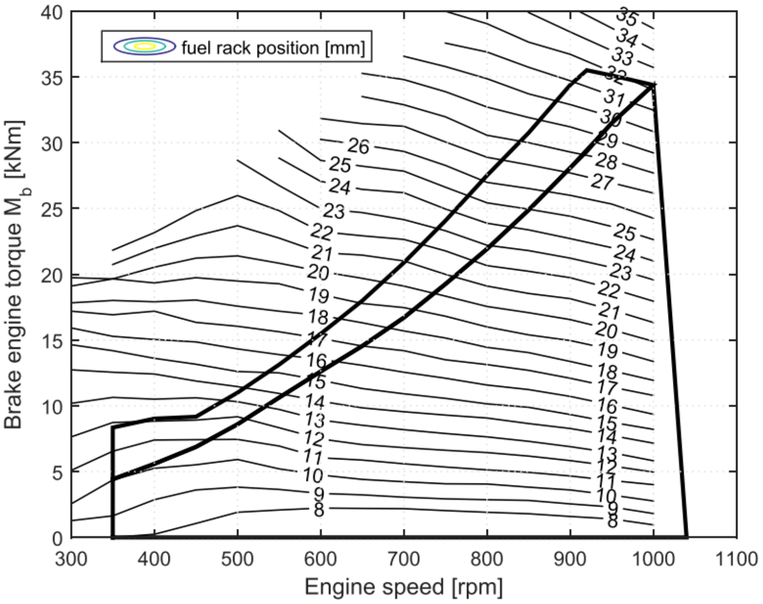

Figure 2-3: Diesel engine fuel rack map [1]

In order to keep the model of the engine simple, a straightforward relation to calculate the torque based on the shaft speed and the fuel rack position is devised. However, the shaft speed of the propeller is not the same as the engine speed. The propeller is turning at a slower rate than the engine. In order to accomplish this, a gearbox is placed between the engine and the propeller shaft, resulting in the following relation:

$$\omega_e = i_{gb}\omega \tag{2-11}$$

In this equation, i_{gb} is the gearbox ratio. The following relation is used to calculate the brake engine torque [1]:

$$M_b = \left(\frac{\delta M_b}{\delta \omega_e}\omega_e + M_{b,\omega_e}\right) + \left(\frac{\delta M_b}{\delta X}X + M_{b,X}\right) \tag{2-12}$$

This can be rewritten to:

$$M_b = \frac{\delta M_b}{\delta \omega_e}\omega_e + \frac{\delta M_b}{\delta X}X + \left(M_{b,\omega_e} + M_{b,X}\right) \tag{2-13}$$

Here, the partial derivatives of the engine torque with respect to the engine speed and fuel rack position are engine specific coefficients, describing the gradients in the fuel rack map. X describes the position of the fuel rack, which is the input to the engine. A higher fuel rack position means more fuel is injected near the end of the compression stroke. This results in more fuel being burned, and more torque and power being delivered by the engine. For simplicity, the assumption is made that both partial derivatives in Eq. (2-13) are constant, which means that the lines in Figure 2-3 are straight lines. The partial derivatives and the constant terms are named a, b and c:

$$\frac{\delta M_b}{\delta \omega_e} = a, \quad \frac{\delta M_b}{\delta X} = b, \quad \left(M_{b,\omega_e} + M_{b,X}\right) = c \tag{2-14}$$

There is a difference between the torque that is supplied by the engine before the gearbox M_b and the torque that is experienced by the shaft after the gearbox. The gearbox does not only change the speed of the shaft, it also changes the torque. The final torque delivered to the propeller after the gearbox becomes:

$$(ai_{gb}\omega + bX + c)i_{gb}\eta_{trm} \tag{2-15}$$

In this equation, η_{trm} is the transmission efficiency, describing the losses in the transmission. This is a combination of the gearbox and the shaft efficiency:

$$\eta_{trm} = \eta_{gb}\eta_s \tag{2-16}$$

This model of the engine results in the following fuel rack map:

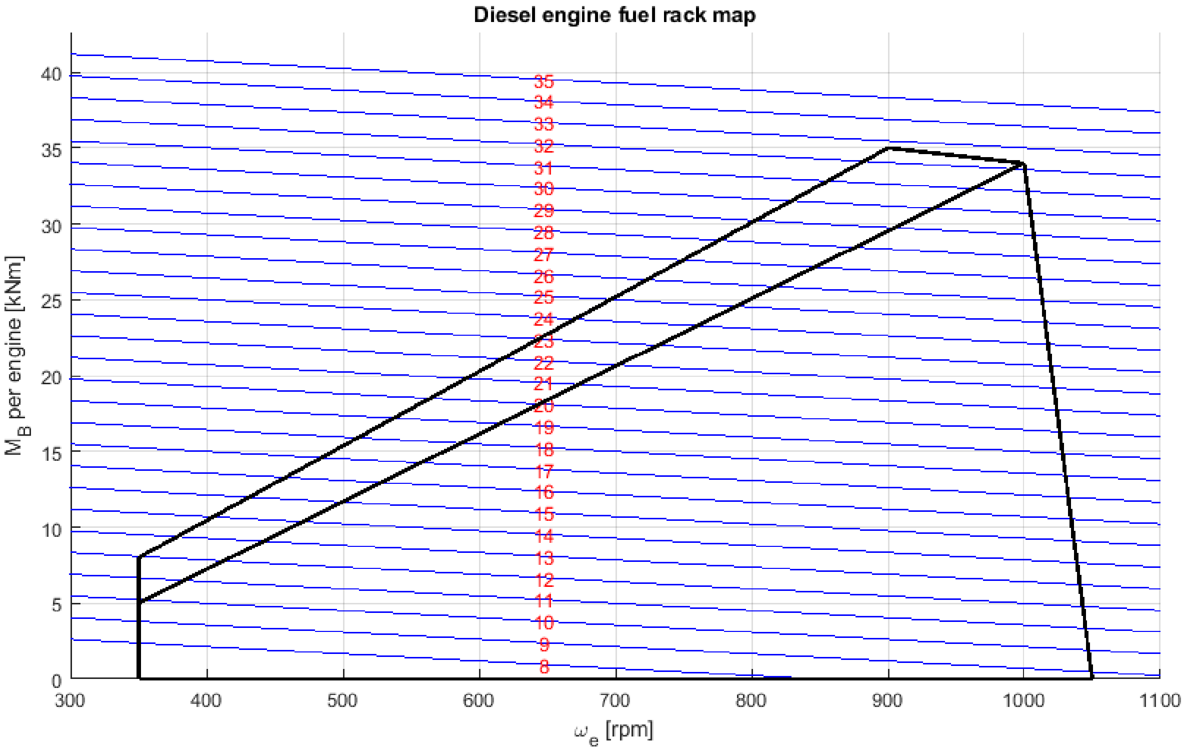

Figure 2-4: Modeled diesel engine fuel rack map

The fuel rack map resembles Figure 2-3, but the contour lines are straight according to the assumption that a, b and c are constant. The black lines were roughly copied from the original fuel rack map, to indicate the operating limits of the engine.

2-5 Measured Shaft Torque

The assumption is made that all observers covered in Chapter 3 have access to the measured shaft torque and the measured shaft speed. This is due to the fact that both shaft speed and shaft torque are commonly available measurements in ship propulsion systems, whereas measurements of e.g. thrust and shaft acceleration are much less common. Measuring shaft speed is quite straightforward. This can be accomplished with an encoder. Unfortunately, measuring the shaft torque is more difficult. The torque on the shaft can be measured with a strain gauge. However, the placement of the strain gauge has a very large impact on the measured signal. If the strain gauge is placed close to the engine, it will measure the engine torque. If it is placed close to the propeller, it will measure the propeller torque. Unfortunately, it is not possible to place the sensor close to the propeller, since the shaft leading to the propeller is usually not inside, but rather outside the hull, surrounded by water. In order to obtain a reliable measurement of shaft torque, the choice was made to place the strain gauge on the propeller shaft, close to the gearbox, between the gearbox and the propeller. This can be seen in Figure 2-1. This leads to a challenge, since this torque is not supplied by the model. In order to obtain this measured shaft torque, the propulsion system can theoretically be cut in two. The system is "cut" in the precise location where the strain gauge is placed. The left part contains the engine, the gearbox and the shaft between the engine and the gearbox. The right part contains the propeller, and the shaft between the propeller and the gearbox. Next, the torque that is applied by either side at the separation point can be evaluated. For the left side, this yields:

$$M_m = M_b i_{gb} \eta_{trm} - \dot{\omega} I_L \tag{2-17}$$

This means the torque applied by the left side of the propulsion system is a result of the break engine torque and the acceleration of the left side of the propulsion system. Here, $M_m$indicates the measured shaft torque, and I_L indicates the moment of inertia of the left side of the propulsion system. The same can be repeated for the right side:

$$M_m = \dot{\omega} I_R + M_p \tag{2-18}$$

This shows that the torque applied by the right side of the propulsion system is a result of the propeller torque and the acceleration of the right side of the propulsion system. Here, I_R indicates the moment of inertia of the right side of the propulsion system.

If these two equations are combined, and the measured shaft torque is substituted from one equation into the other, this results in Eq. (2-1). This means that the measured shaft torque M_m is the torque which is experienced by a strain gauge placed at the aforementioned location, and this measured shaft torque will be used by the observers in combination with the measured shaft speed. In order to include this variable as an output in the model, it must be rewritten in terms of the chosen states and inputs as chosen in Section 2-6. This yields:

$$M_m = \frac{I_R}{I}(a i_{gb}\omega + bX + c) i_{gb} \eta_{trm} + \frac{I_L}{I} \rho D^5 \left(\frac{\omega}{2\pi}\right)^2 K_Q(J(\omega, v_a), {}^{P}\!/\!{}_{D}) \eta_r^{-1} \tag{2-19}$$

2-6 Combined model of uncontrolled plant

Now that all individual parts have been described, the parts can be combined into the complete model of the uncontrolled plant. The uncontrolled plant is the ship propulsion system without any controller implemented. Analyses will be performed on the uncontrolled plant, to ensure all system dynamics can be analyzed, without interference by a controller. The plant contains three states: the pitch ratio, the shaft speed and the ship speed. It contains two inputs, the fuel rack position and the desired pitch ratio. The combined model becomes:

$$
\begin{aligned}
x &= \begin{bmatrix} {}^{P}\!/_{D} \\ \omega \\ v_s \end{bmatrix}, \quad u = \begin{bmatrix} {}^{P}\!/_{D_d} \\ X \end{bmatrix}, \quad y = \begin{bmatrix} {}^{P}\!/_{D} \\ \omega \\ v_s \\ M_m \end{bmatrix} \\
\dot{x} &= \begin{bmatrix} \dot{{}^{P}\!/_{D}} \\ \dot{\omega} \\ \dot{v}_s \end{bmatrix} = \begin{bmatrix} \frac{1}{\tau_p}({}^{P}\!/_{D_d} - {}^{P}\!/_{D}) \\ \frac{1}{I}((ai_{gb}\omega + bX + c)i_{gb}\eta_{trm} - \rho D^5 \left(\frac{\omega}{2\pi}\right)^2 K_Q(J(\omega, v_a), {}^{P}\!/_{D})\eta_r^{-1}) \\ \frac{1}{m_s}(\rho D^4 \left(\frac{\omega}{2\pi}\right)^2 K_T(J(\omega, v_a), {}^{P}\!/_{D})k_p(1-t) - d_{c_1}c_1 v_s^2) \end{bmatrix} \\
y &= \begin{bmatrix} {}^{P}\!/_{D} \\ \omega \\ v_s \\ \frac{I_R}{I}(ai_{gb}\omega + bX + c)i_{gb}\eta_{trm} + \frac{I_L}{I}\rho D^5 \left(\frac{\omega}{2\pi}\right)^2 K_Q(J(\omega, v_a), {}^{P}\!/_{D})\eta_r^{-1} \end{bmatrix}
\end{aligned}
\tag{2-20}
$$

This shows that the nonlinearities in the system originate from Eq. (2-5) and Eq. (2-6) describing the behavior of the propeller, from Eq. (2-10) describing the resistance of the ship, and from Eq. (2-15) describing the behavior of the engine. As the pitch actuation mechanism is modeled as a first-order system, no nonlinearities are present in the pitch actuator.

2-7 Linearization

Now that the non-linear model has been created, it is possible to linearize the model. A linear model is much easier to use for control purposes, so the linearization of the model is a logical next step. In order to obtain a linearized state-space system, the A-matrix will be obtained by taking the Jacobian of the system with respect to the states, and the B-matrix will be obtained by taking the Jacobian of the states with respect to the inputs. Furthermore, the system will also be linearized with respect to the disturbances d_{c_1} and u_x. The same steps will be repeated for the outputs, yielding matrices C and D. In Section 2-7-1, the process of linearizing the plant will be shown step by step, for each system equation. In Section 2-7-2, the linearized model is presented. Finally, in Section 2-7-3, a frequency analysis is performed on the linearized plant.

2-7-1 Linearizing the plant

The first equation describes the motion of the pitch actuator:

$$
\dot{{}^{P}\!/_{D}} = \frac{1}{\tau_p}({}^{P}\!/_{D_d} - {}^{P}\!/_{D}) \tag{2-21}
$$

The partial derivatives of $\dot{{}^{P}\!/_{D}}$ with respect to the states, inputs and disturbances are:

$$
\frac{\delta \dot{{}^{P}\!/_{D}}}{\delta {}^{P}\!/_{D}} = -\frac{1}{\tau_p}, \quad \frac{\delta \dot{{}^{P}\!/_{D}}}{\delta \omega} = 0, \quad \frac{\delta \dot{{}^{P}\!/_{D}}}{\delta v_s} = 0, \quad \frac{\delta \dot{{}^{P}\!/_{D}}}{\delta {}^{P}\!/_{D_d}} = \frac{1}{\tau_p}, \quad \frac{\delta \dot{{}^{P}\!/_{D}}}{\delta X} = 0, \quad \frac{\delta \dot{{}^{P}\!/_{D}}}{\delta d_{c_1}} = 0, \quad \frac{\delta \dot{{}^{P}\!/_{D}}}{\delta u_x} = 0 \tag{2-22}
$$

Next, the linearized version of the first system equation can be obtained by substituting the equilibrium points into the partial derivatives, multiplying the partial derivatives by their respective linear state, input or disturbance, and adding the equilibrium points substituted into the original system equation. This results in the following linearized system equation for the pitch actuator:

$$\dot{{}^{P}/_{D}}_{\Delta} = -\frac{1}{\tau_p} {}^{P}/_{D\Delta} + \frac{1}{\tau_p} {}^{P}/_{Dd\Delta} + \frac{1}{\tau_p}({}^{P}/_{Dd,eq} - {}^{P}/_{Deq}) \tag{2-23}$$

The subscript Δ indicates the variable describes a small deviation around the linearization point, and the subscript eq indicates the value is taken at an equilibrium point. This results in the following definition for all states, inputs and disturbances:

$$X = X_{eq} + X_{\Delta} \tag{2-24}$$

This means that every variable is a combination of an equilibrium value around which the linearization is performed, and a small deviation from that equilibrium value.

The same process can be repeated for the second system equation, regarding the motion of the shaft. Again, the equation describing the motion of the shaft:

$$\dot{\omega} = \frac{1}{I}((ai_{gb}\omega + bX + c)i_{gb}\eta_{trm} - \rho D^5 \left(\frac{\omega}{2\pi}\right)^2 K_Q(J(\omega, v_a), {}^{P}/_{D})\eta_r^{-1}) \tag{2-25}$$

This yields the following partial derivatives with respect to the states, inputs and disturbances:

$$\begin{aligned}
&\frac{\delta\dot{\omega}}{\delta {}^{P}/_{D}} = -\frac{1}{I}\rho D^5 \frac{1}{4\pi^2}\eta_r^{-1}\omega^2 \frac{\delta K_Q}{\delta {}^{P}/_{D}}, \quad \frac{\delta\dot{\omega}}{\delta\omega} = \frac{1}{I}\left(ai_{gb}^2\eta_{trm} - \rho D^5 \frac{1}{4\pi^2}\eta_r^{-1}\left(2\omega K_Q + \omega^2\frac{\delta K_Q}{\delta\omega}\right)\right) \\
&\frac{\delta\dot{\omega}}{\delta v_s} = -\frac{1}{I}\rho D^5 \frac{1}{4\pi^2}\eta_r^{-1}\omega^2 \frac{\delta K_Q}{\delta v_s}, \quad \frac{\delta\dot{\omega}}{\delta {}^{P}/_{D_d}} = 0, \quad \frac{\delta\dot{\omega}}{\delta X} = \frac{1}{I}bi_{gb}\eta_{trm}, \\
&\frac{\delta\dot{\omega}}{\delta d_{c_1}} = 0, \quad \frac{\delta\dot{\omega}}{\delta u_x} = -\frac{1}{I}\rho D^5 \frac{1}{4\pi^2}\eta_r^{-1}\omega^2 \frac{\delta K_Q}{\delta u_x}
\end{aligned} \tag{2-26}$$

Multiplying the partial derivatives by their respective state, input or disturbance, entering the equilibrium points and adding the equilibrium substituted in the original equation yields the linearized system equation for the motion of the shaft:

$$\begin{aligned}
\dot{\omega}_{\Delta} = &- \frac{1}{I}\rho D^5 \frac{1}{4\pi^2}\eta_r^{-1}\omega_{eq}^2 \frac{\delta K_{Q,eq}}{\delta {}^{P}/_{D}} {}^{P}/_{D\Delta} + \frac{1}{I}\left(ai_{gb}^2\eta_{trm} - \rho D^5 \frac{1}{4\pi^2}\eta_r^{-1}\left(2\omega_{eq}K_{Q,eq} + \omega_{eq}^2\frac{\delta K_{Q,eq}}{\delta\omega}\right)\right)\omega_{\Delta} \\
&- \frac{1}{I}\rho D^5 \frac{1}{4\pi^2}\eta_r^{-1}\omega_{eq}^2 \frac{\delta K_{Q,eq}}{\delta v_s} v_{s\Delta} + \frac{1}{I}bi_{gb}\eta_{trm}X_{\Delta} \\
&- \frac{1}{I}\rho D^5 \frac{1}{4\pi^2}\eta_r^{-1}\omega_{eq}^2 \frac{\delta K_{Q,eq}}{\delta u_x} u_{x\Delta} \\
&+ \frac{1}{I}\left(\left(ai_{gb}\omega_{eq} + bX_{eq} + c\right)i_{gb}\eta_{trm} - \rho D^5 \frac{1}{4\pi^2}\eta_r^{-1}\omega_{eq}^2 K_{Q,eq}\right)
\end{aligned} \tag{2-27}$$

The same process can be repeated for the equation of motion of the ship speed:

$$\dot{v}_s = \frac{1}{m_s}(\rho D^4 \left(\frac{\omega}{2\pi}\right)^2 K_T(J(\omega, v_a), {}^{P}/_{D})k_p(1-t) - d_{c_1}c_1v_s^2) \tag{2-28}$$

The partial derivatives of the ship acceleration to the states, inputs and disturbances are:

$$
\begin{aligned}
&\frac{\delta \dot{v}_s}{\delta {}^{P}\!/_{D}} = \frac{1}{m_s}\rho D^4 \frac{1}{4\pi^2} k_p (1-t)\omega^2 \frac{\delta K_T}{\delta {}^{P}\!/_{D}}, \quad \frac{\delta \dot{v}_s}{\delta \omega} = \frac{1}{m_s}\rho D^4 \frac{1}{4\pi^2} k_p (1-t)\left(2\omega K_T + \omega^2 \frac{\delta K_T}{\delta \omega}\right), \\
&\frac{\delta \dot{v}_s}{\delta v_s} = \frac{1}{m_s}\left(\rho D^4 \frac{1}{4\pi^2} k_p (1-t)\omega^2 \frac{\delta K_T}{\delta v_s} - 2 d_{c_1} c_1 v_s\right), \quad \frac{\delta \dot{v}_s}{\delta {}^{P}\!/_{D_d}} = 0, \quad \frac{\delta \dot{v}_s}{\delta X} = 0 \\
&\frac{\delta \dot{v}_s}{\delta d_{c_1}} = -\frac{1}{m_s} c_1 v_s^2, \quad \frac{\delta \dot{v}_s}{\delta u_x} = \frac{1}{m_s}\rho D^4 \frac{1}{4\pi^2} k_p (1-t)\omega^2 \frac{\delta K_T}{\delta u_x}
\end{aligned}
\tag{2-29}
$$

Again, multiplying the partial derivatives by their respective state or input, entering the equilibrium points and adding the equilibrium substituted in the original equation yields the linearized system equation for the motion of the ship:

$$
\begin{aligned}
\dot{v}_{s\Delta} =& \frac{1}{m_s}\rho D^4 \frac{1}{4\pi^2} k_p (1-t)\omega_{eq}^2 \frac{\delta K_{T,eq}}{\delta {}^{P}\!/_{D}} {}^{P}\!/_{D\Delta} + \frac{1}{m_s}\rho D^4 \frac{1}{4\pi^2} k_p (1-t)\left(2\omega_{eq} K_{T,eq} + \omega_{eq}^2 \frac{\delta K_{T,eq}}{\delta \omega}\right)\omega_\Delta \\
&+ \frac{1}{m_s}\left(\rho D^4 \frac{1}{4\pi^2} k_p (1-t)\omega_{eq}^2 \frac{\delta K_{T,eq}}{\delta v_s} - 2 d_{c_1,eq} c_1 v_{s,eq}\right) v_{s\Delta} - \frac{1}{m_s} c_1 v_{s,eq}^2 d_{c_1\Delta} \\
&+ \frac{1}{m_s}\rho D^4 \frac{1}{4\pi^2} k_p (1-t)\omega_{eq}^2 \frac{\delta K_{T,eq}}{\delta u_x} u_{x\Delta} + \frac{1}{m_s}\left(\rho D^4 \frac{1}{4\pi^2} k_p (1-t)\omega_{eq}^2 K_{T,eq} - d_{c_1,eq} c_1 v_{s,eq}^2\right)
\end{aligned}
\tag{2-30}
$$

Finally, the same process can be repeated for the output M_m, from Eq. (2-19). The partial derivatives of the measured shaft speed to the states, inputs and disturbances are:

$$
\begin{aligned}
&\frac{\delta M_m}{\delta {}^{P}\!/_{D}} = \frac{I_L}{I}\rho D^5 \frac{1}{4\pi^2}\eta_r^{-1}\omega^2 \frac{\delta K_Q}{\delta {}^{P}\!/_{D}}, \quad \frac{\delta M_m}{\delta \omega} = \frac{I_R}{I} a i_{gb}^2 \eta_{trm} + \frac{I_L}{I}\rho D^5 \frac{1}{4\pi^2}\eta_r^{-1}\left(2\omega K_Q + \omega^2 \frac{\delta K_Q}{\delta \omega}\right) \\
&\frac{\delta M_m}{\delta v_s} = \frac{I_L}{I}\rho D^5 \frac{1}{4\pi^2}\eta_r^{-1}\omega^2 \frac{\delta K_Q}{\delta v_s}, \quad \frac{\delta M_m}{\delta {}^{P}\!/_{D_d}} = 0, \quad \frac{\delta M_m}{\delta X} = \frac{I_R}{I} b i_{gb} \eta_{trm}, \\
&\frac{\delta M_m}{\delta d_{c_1}} = 0, \quad \frac{\delta M_m}{\delta u_x} = \frac{I_L}{I}\rho D^5 \frac{1}{4\pi^2}\eta_r^{-1}\omega^2 \frac{\delta K_Q}{\delta u_x}
\end{aligned}
\tag{2-31}
$$

Multiplying the partial derivatives by their respective state, input or disturbance, entering the equilibrium points and adding the equilibrium substituted in the original equation yields the linearized system equation for the measured shaft torque:

$$
\begin{aligned}
M_{m\Delta} =& \frac{I_L}{I}\rho D^5 \frac{1}{4\pi^2}\eta_r^{-1}\omega_{eq}^2 \frac{\delta K_{Q,eq}}{\delta {}^{P}\!/_{D}} {}^{P}\!/_{D\Delta} + \left(\frac{I_R}{I} a i_{gb}^2 \eta_{trm} + \frac{I_L}{I}\rho D^5 \frac{1}{4\pi^2}\eta_r^{-1}\left(2\omega_{eq} K_{Q,eq} + \omega_{eq}^2 \frac{\delta K_{Q,eq}}{\delta \omega}\right)\right)\omega_\Delta \\
&\frac{I_L}{I}\rho D^5 \frac{1}{4\pi^2}\eta_r^{-1}\omega_{eq}^2 \frac{\delta K_{Q,eq}}{\delta v_s} v_{s\Delta} + \frac{I_R}{I} b i_{gb} \eta_{trm} X_\Delta + \frac{I_L}{I}\rho D^5 \frac{1}{4\pi^2}\eta_r^{-1}\omega_{eq}^2 \frac{\delta K_{Q,eq}}{\delta u_x} u_{x\Delta} \\
&+ \frac{I_R}{I}\left(\left(a i_{gb}\omega_{eq} + b X_{eq} + c\right) i_{gb}\eta_{trm}\right) + \frac{I_L}{I}\rho D^5 \frac{1}{4\pi^2}\eta_r^{-1}\omega_{eq}^2 K_{Q,eq}
\end{aligned}
\tag{2-32}
$$

In Section 2-7-2, all these linearized equations will be combined into the complete linearized plant.

2-7-2 Linearized Model

Combining all three equations derived in Section 2-7-1 yields the complete linearized model of the ship propulsion system. In order to make the linearized model more readable, the following substitutions are made:

$$Y = \frac{\rho D^5 \omega_{eq}}{4\pi^2 I \eta_r} \tag{2-33}$$

$$Z = \frac{\rho D^4 k_p (1-t) \omega_{eq}}{4\pi^2 m_s} \tag{2-34}$$

The complete state-space representation of the linearized ship propulsion model:

$$x_\Delta = \begin{bmatrix} {}^P/_{D\Delta} \\ \omega_\Delta \\ v_{s\Delta} \end{bmatrix}, \quad u_\Delta = \begin{bmatrix} {}^P/_{D d\Delta} \\ X_\Delta \end{bmatrix}, \quad w_\Delta = \begin{bmatrix} d_{c_1\Delta} \\ u_{x\Delta} \end{bmatrix}, \quad y = \begin{bmatrix} {}^P/_{D\Delta} \\ \omega_\Delta \\ v_{s\Delta} \\ M_{m\Delta} \end{bmatrix}$$

$$\begin{aligned}
\dot{x}_\Delta = & \begin{bmatrix} -\frac{1}{\tau_p} & 0 & 0 \\ -Y\omega_{eq}\frac{\delta K_{Q,eq}}{\delta {}^P/_D} & -Y\left(2K_{Q,eq} + \omega_{eq}\frac{\delta K_{Q,eq}}{\delta\omega}\right) + \frac{a i_{gb}^2 \eta_{trm}}{I} & -Y\omega_{eq}\frac{\delta K_{Q,eq}}{\delta v_s} \\ Z\omega_{eq}\frac{\delta K_{T,eq}}{\delta {}^P/_D} & Z\left(2K_{T,eq} + \omega_{eq}\frac{\delta K_{T,eq}}{\delta\omega}\right) & Z\omega_{eq}\frac{\delta K_{T,eq}}{\delta v_s} - \frac{d_{c_1,eq} c_1 v_{s,eq}^2}{m_s}) \end{bmatrix} x_\Delta + \\
& \begin{bmatrix} \frac{1}{\tau_p} & 0 \\ 0 & \frac{b i_{gb} \eta_{trm}}{I} \\ 0 & 0 \end{bmatrix} u_\Delta + \begin{bmatrix} 0 & 0 \\ 0 & -Y\omega_{eq}\frac{\delta K_{Q,eq}}{\delta u_x} \\ -\frac{c_1 v_{s,eq}^2}{m_s} & Z\omega_{eq}\frac{\delta K_{T,eq}}{\delta u_x} \end{bmatrix} w_\Delta + \\
& \begin{bmatrix} \frac{{}^P/_{D d,eq} - {}^P/_{D eq}}{\tau_p} \\ -Y\omega_{eq} K_{Q,eq} + \frac{(a i_{gb}\omega_{eq} + b X_{eq} + c) i_{gb} \eta_{trm}}{I} \\ Z\omega_{eq} K_{T,eq} - \frac{d_{c_1,eq} c_1 v_{s,eq}^2}{m_s} \end{bmatrix} \\
y = & \begin{bmatrix} 1 & 0 & 0 \\ 0 & 1 & 0 \\ 0 & 0 & 1 \\ Y I_L \omega_{eq}\frac{\delta K_{Q,eq}}{\delta {}^P/_D} & Y I_L\left(2K_{Q,eq} + \omega_{eq}\frac{\delta K_{Q,eq}}{\delta\omega}\right) + \frac{I_R a i_{gb}^2 \eta_{trm}}{I} & Y I_L \omega_{eq}\frac{\delta K_{Q,eq}}{\delta v_s} \end{bmatrix} x_\Delta + \\
& \begin{bmatrix} 0 & 0 \\ 0 & 0 \\ 0 & 0 \\ 0 & \frac{I_R b i_{gb} \eta_{trm}}{I} \end{bmatrix} u_\Delta + \begin{bmatrix} 0 & 0 \\ 0 & 0 \\ 0 & 0 \\ 0 & Y I_L \omega_{eq}\frac{\delta K_{Q,eq}}{\delta u_x} \end{bmatrix} w_\Delta + \\
& \begin{bmatrix} 0 \\ 0 \\ 0 \\ Y I_L \omega_{eq} K_{Q,eq} + \frac{I_R (a i_{gb}\omega_{eq} + b X_{eq} + c) i_{gb} \eta_{trm}}{I} \end{bmatrix}
\end{aligned} \tag{2-35}$$

The constant terms that are present at the end of the state-space representation are zero if there is no acceleration present in the chosen equilibrium. The linearization contains partial derivatives of both

K_Q and K_T to $^P/_D$, ω, v_s and u_x. The torque and thrust coefficients are a direct function of advance ratio J and pitch ratio $^P/_D$, and therefore, the partial derivatives of the torque and thrust coefficients to J and $^P/_D$ can be calculated from the open water propeller diagrams. Some additional calculations are required to obtain the partial derivatives to the shaft/ship speed and the disturbance in advance velocity. This is calculated in the following manner:

$$\frac{\delta K_{Q,T}}{\delta \omega} = \frac{\delta K_{Q,T}}{\delta J}\frac{\delta J}{\delta \omega}, \quad \frac{\delta K_{Q,T}}{\delta v_s} = \frac{\delta K_{Q,T}}{\delta J}\frac{\delta J}{\delta v_s}, \quad \frac{\delta K_{Q,T}}{\delta u_x} = \frac{\delta K_{Q,T}}{\delta J}\frac{\delta J}{\delta u_x} \tag{2-36}$$

This only leaves the calculation of the partial derivatives of the advance ratio to the shaft/ship speed and the disturbance in advance velocity. Combining Eq. (2-7) and Eq. (2-8) yields:

$$J(\omega, v_s) = \frac{2\pi((1-w)v_s + u_x)}{\omega D} \tag{2-37}$$

This results in:

$$\frac{\delta J}{\delta \omega} = \frac{-2\pi((1-w)v_s + u_x)}{\omega^2 D}, \quad \frac{\delta J}{\delta v_s} = \frac{2\pi(1-w)}{\omega D}, \quad \frac{\delta J}{\delta u_x} = \frac{2\pi}{\omega D} \tag{2-38}$$

It is possible to utilize the linearized plant in two different ways. Firstly, it is possible to choose one linearization point or equilibrium, and to use the model linearized around this one point. This results in a constant state-space system, where the system matrices do not change. This leads to accurate behavior when the system is operated around the chosen equilibrium, but can lead to large deviations when the operating point differs from the linearization point. Secondly, it is possible to constantly update the linearized model, to provide far more accurate performance. In this case, the states, inputs and disturbances are obtained from the non-linear plant, and the linearization is performed around these linearization points. Furthermore, the inputs and disturbances with subscript Δ are taken to be zero, since the system is exactly in the equilibrium point at all times. This results in a constantly changing state-space system, with very accurate performance. At any point in time, the linear state-space model is available for observers or control algorithms. This does however require accurate knowledge on the linearization points. Although some variables like shaft speed are often available, other variables such as disturbances are often unknown. To solve this, it is possible to linearize the system around the known parameters, and to choose constants for the unknown parameters.

This concludes the synthesis of the model of the uncontrolled plant and its linearization.

2-7-3 Frequency Analysis of Linearized Plant

Now that the plant has been linearized, it is possible to perform a frequency analysis, to learn how the model behaves in the frequency domain. Before the frequency analysis can be performed, several working points must be determined. These are the points around which the non-linear plant will be linearized. The working points will be chosen at the edges of the inputs of the system. Firstly, the lowest available pitch ratio of the open water propeller diagram is selected and is combined with the lowest value for the fuel rack for which the engine can operate normally. This is repeated with the lowest possible pitch ratio and the highest possible fuel rack position for that pitch. This yields two operating points. The same process can be repeated, but with the highest possible pitch ratio of the open water propeller diagram. This, again, yields two operating points for the highest and lowest possible shaft speed. When looking at the diesel engine fuel rack map in Figure 2-4, it is clear that the lowest possible engine speed is 350 *rpm*, and the highest possible engine speed is 1000 *rpm*. This is equivalent to a shaft speed of roughly 4.97 $rad\ s^{-1}$ and 14.19 $rad\ s^{-1}$ respectively, taking the gearbox ratio into account. When combining the low and high shaft speeds with the low and high pitch ratios, the following working points emerge:

Table 2-1: Working points

	P/D [-]	ω [$rad\ s^{-1}$]	X [mm]	v_s [$m\ s^{-1}$]	v_a [$m\ s^{-1}$]	M_b [$N\ m$]
A	0.6	4.94	7.03	1.96	1.86	999.1
B	0.6	14.1	14.2	5.59	5.31	8122
C	1.4	4.88	9.40	4.05	3.85	4419
D	1.4	14.2	34.7	11.8	11.2	37430

The linearization was performed for each of the four working points, resulting in four different linearized plants. The plants were visualized in a Bode plot, which can be found in Figure 2-5. Shown here are the magnitude plots from all four inputs to all four outputs. The first column of figures shows the transfer from P/D_d to the four outputs. The first figure shows the first order transfer function for the pitch actuator, as described in 2-2.

Table 2-2: Poles and zeros for $\frac{P/D}{P/D_d}$

Working Point	Poles	Zeros	DC-gain [−]
A	−0.5	−	1
B	−0.5	−	1
C	−0.5	−	1
D	−0.5	−	1

Here, the single pole is found at −0.5. This transfer function is not affected by the different working points, since the behavior of the pitch actuator is not affected by the pitch or the shaft speed. After the pitch actuator pole, a slope of $-20\ dB\ dec^{-1}$ is found. This transfer has a DC-gain of 1, meaning perfect reference tracking is obtained as long as the frequency of the input is low. The second figure contains the transfer from the desired pitch to the shaft speed.

Table 2-3: Poles and zeros for $\frac{\omega}{P/D_d}$

Working Point	Poles	Zeros	DC-gain [$rad\ s^{-1}$]
A	−0.0091, −0.1392, −0.5	−0.0061	−3.4690
B	−0.0216, −0.3373, −0.5	−0.0173	−14.0153
C	−0.0097, −0.5, −0.5576	−0.0087	−2.5493
D	−0.0265, −0.5, −1.5578	−0.0253	−8.2706

This transfer contains three poles and one zero. The pole at −0.5 originates from the pitch actuator, the smallest pole corresponds to the ship inertia, and the remaining pole corresponds to the shaft inertia.

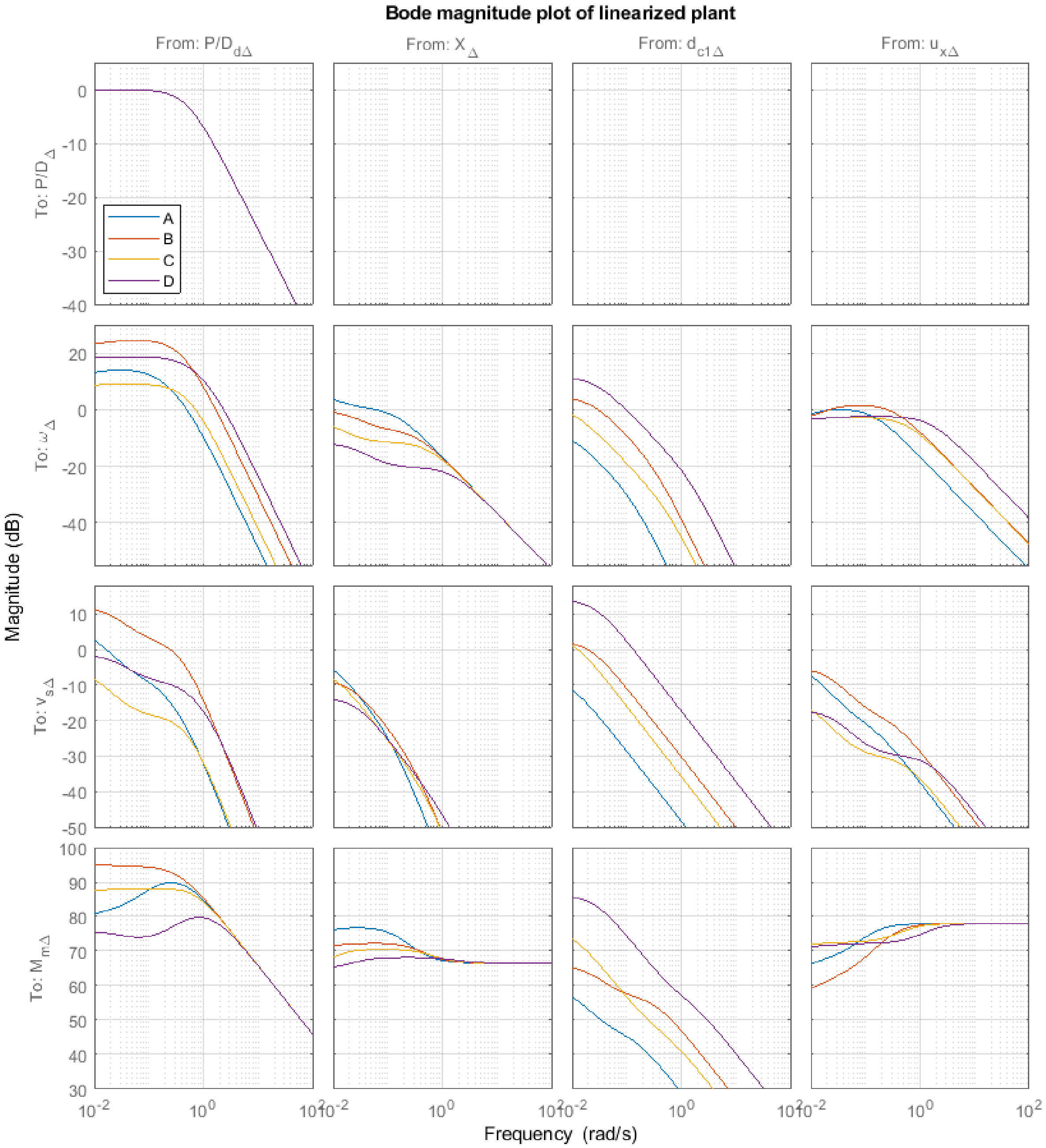

Figure 2-5: Bode plot of system linearized around four different working points

The figure shows that the DC-gain is mostly dependent on the shaft speed, with linearization point C yielding the lowest gain and point B resulting in the highest gain. This makes sense, since a change in the pitch has a higher influence on the shaft speed if the shaft speed is higher. After the pole of the pitch actuator, which is the fastest pole, the magnitude quickly drops at $-40\ dB\ dec^{-1}$. This is due to the fact that at low frequencies, below the pole of the pitch actuator, the pitch can follow the input signal perfectly. This means changes in desired pitch lead to large changes in shaft speed. However, if the frequency of the desired shaft speed is much higher than the bandwidth of the pitch actuator, the actuator cannot keep up and the pitch and therefore the shaft speed will not change as much. The third figure shows the transfer from the desired pitch to the ship speed.

Table 2-4: Poles and zeros for $\frac{v_s}{P/D_d}$

Working Point	Poles	Zeros	DC-gain $[m\ s^{-1}]$
A	−0.0091, −0.1392, −0.5	−0.0447	1.9491
B	−0.0216, −0.3373, −0.5	−0.0634	3.9197
C	−0.0097, −0.5, −0.5576	−0.0442	0.5289
D	−0.0265, −0.5, −1.5578	−0.0631	0.8432

This again contains three poles, for the ship and shaft inertia and the pitch actuator and one zero. At higher frequencies, after the relatively fast pole of the pitch actuator, the magnitude quickly drops with $-40\,dB\,dec^{-1}$ due to the dynamics of the pitch actuator. The fourth and final figure shows the transfer from the desired pitch to the measured shaft torque.

Table 2-5: Poles and zeros for $\frac{M_m}{P/D_d}$

Working Point	Poles	Zeros	DC-gain $[N\ m]$
A	−0.0091, −0.1392, −0.5	−0.0061, −0.0438	8167
B	−0.0216, −0.3373, −0.5	−0.0227, 0.4638	−56377
C	−0.0097, −0.5, −0.5576	−0.0091, −0.3545	23174
D	−0.0265, −0.5, −1.5578	−0.0364, 0.1786	−6170

This shows three poles for the ship and shaft inertia and the pitch actuator, and two zeros. The gain is much higher than for the previous figures, since the shaft torque is in $N\ m$, which has a much higher magnitude than the $rad\ s^{-1}$ of the shaft speed or the $m\,s^{-1}$ of the ship speed. After the fast pole of the pitch actuator, the gain drops with $-20\ dB\ dec^{-1}$, since the pitch actuator cannot keep up with high frequency inputs on the desired pitch.

The second column of figures shows the transfer from X to the four outputs. The first figure is empty, since there is no transfer from X to P/D; changing the fuel rack position has no effect on the pitch angle. The second figure shows the transfer from the fuel rack position to the shaft speed.

Table 2-6: Poles and zeros for $\frac{\omega}{X}$

Working Point	Poles	Zeros	DC-gain [$rad\ s^{-1}\ mm^{-1}$]
A	−0.0091, −0.1392	−0.0167	1.9298
B	−0.0216, −0.3373	−0.0476	0.9596
C	−0.0097, −0.5576	−0.0246	0.6653
D	−0.0265, −1.5578	−0.0714	0.2548

This transfer contains two poles, the higher one corresponding to the shaft inertia and the lower corresponding to the ship inertia, and one zero. After the fast pole of the shaft inertia, the magnitude drops with $-20\ dB\ dec^{-1}$, since the inertia of the shaft and ship are too high to keep up with the rapidly changing engine torque. The third figure shows the transfer from the fuel rack position to the ship speed.

Table 2-7: Poles and zeros for $\frac{v_s}{X}$

Working Point	Poles	Zeros	DC-gain [$m\ s^{-1}\ mm^{-1}$]
A	−0.0091, −0.1392	–	0.7651
B	−0.0216, −0.3373	–	0.3804
C	−0.0097, −0.5576	–	0.5527
D	−0.0265, −1.5578	–	0.2117

This contains two poles, one for the shaft and one for the ship inertia and no zeros. At frequencies higher than the pole of the shaft inertia, a slope of $-40\ dB\ dec^{-1}$ is found in the magnitude plot. The fourth and final figure shows the transfer from the fuel rack position to the measured shaft torque.

Table 2-8: Poles and zeros for $\frac{M_m}{X}$

Working Point	Poles	Zeros	DC-gain [$N\ m\ mm^{-1}$]
A	−0.0091, −0.1392	−0.0070, −0.4686	5472.7
B	−0.0216, −0.3373	−0.0196, −0.6666	3787.6
C	−0.0097, −0.5576	−0.0032, −0.8914	1105.3
D	−0.0265, −1.5578	−0.0178, −1.8938	1730.5

This transfer contains two poles for the shaft and ship inertia, and two zeros. This shows a relatively flat response, due to the presence of the two zeros. At higher frequencies, the gain from fuel rack position to shaft torque remains flat irrespective of the working point with a slope of $0\ dB\ dec^{-1}$. This is due to the fact that the engine is modeled to deliver instant torque upon changing the fuel rack position, therefore instantly changing the measured shaft torque.

The third column of figures shows the transfer from d_{c_1} to the four outputs. Again, the first figure is empty, since changing the ship resistance disturbance does not affect the pitch. The second figure shows the transfer from the ship resistance disturbance to the shaft speed.

Table 2-9: Poles and zeros for $\frac{\omega}{d_{c_1}}$

Working Point	Poles	Zeros	DC-gain $[rad\ s^{-1}]$
A	−0.0091, −0.1392	–	−0.4224
B	−0.0216, −0.3373	–	−1.7070
C	−0.0097, −0.5576	–	−1.1729
D	−0.0265, −1.5578	–	−3.8046

This again shows two poles for the shaft and ship inertia, and no zeros. The magnitude plot shows an increasing gain as the ship speed of the linearization point increases. This is due to the fact that a change in the ship resistance disturbance has a much larger effect when the ship speed is higher. In this case, increasing the ship resistance disturbance decreases the ship speed, which decreases the advance velocity, which has an effect on the shaft speed. At high frequencies, a slope of $-40\ dB\ dec^{-1}$ is found in the magnitude plot. Due to the locations of the two poles, the transfer from the ship resistance disturbance to the shaft speed is much higher at low frequencies than at high input frequencies. Since the observers will use measurements of the shaft speed, this will likely lead to a better estimation of advance velocity if the ship resistance disturbance has a lower frequency. The third figure shows the transfer from the ship resistance disturbance to the ship speed.

Table 2-10: Poles and zeros for $\frac{v_s}{d_{c_1}}$

Working Point	Poles	Zeros	DC-gain $[m\ s^{-1}]$
A	−0.0091, −0.1392	−0.1317	−0.3975
B	−0.0216, −0.3373	−0.3113	−1.3326
C	−0.0097, −0.5576	−0.5428	−1.6436
D	−0.0265, −1.5578	−1.5129	−5.1114

This transfer contains two poles and one zero. The figure shows roughly the same relations of gains as the transfer from the ship resistance disturbance to the shaft speed, due to the fact that the ship resistance disturbance has a larger effect on the ship and shaft speed if the ship speed is higher. The transfer between ship resistance disturbance and shaft speed shows a sharper decline of magnitude with higher frequency, since that transfer does not contain a zero where the transfer from ship resistance disturbance to ship speed does. This results in a slope of $-20\ dB\ dec^{-1}$ after the fastest pole. The fourth figure shows the transfer from the ship resistance disturbance to the measured shaft torque.

Table 2-11: Poles and zeros for $\frac{M_m}{d_{c_1}}$

Working Point	Poles	Zeros	DC-gain $[N\ m]$
A	−0.0091, −0.1392	−0.0438	994
B	−0.0216, −0.3373	−0.0610	1961
C	−0.0097, −0.5576	−0.2996	6816
D	−0.0265, −1.5578	−0.8060	20458

This transfer contains two poles for the shaft and ship speed, and one zero. This transfer shows a slope of $-20\ dB\ dec^{-1}$ at frequencies beyond the fastest pole of the shaft inertia. Again, at lower input frequencies a much higher gain is found due to the location of the two poles. This will lead to a higher transfer from the ship resistance disturbance to the measured shaft speed. Since the observers use measurements of the shaft speed, it is expected that a lower frequency ship resistance disturbance will lead to a more effective estimation of advance velocity.

The fourth and final column shows the transfer from u_x to the four outputs. Once again the first figure is empty, since a change in advance velocity has no effect on the propeller pitch angle. The second figure shows the transfer from the advance velocity disturbance to the shaft speed.

Table 2-12: Poles and zeros for $\frac{\omega}{u_x}$

Working Point	Poles	Zeros	DC-gain [$rad\ m^{-1}$]
A	−0.0091, −0.1392	−0.0039	0.4539
B	−0.0216, −0.3373	−0.0112	0.6435
C	−0.0097, −0.5576	−0.0081	0.6094
D	−0.0265, −1.5578	−0.0236	0.6794

This contains two poles and one zero. The DC-gain increases with increasing advance velocity of the working point. Furthermore, at a frequency of $0.1 rad\, s^{-1}$, a gain from the advance velocity disturbance to the shaft speed of roughly 0.5 dB is found. This means there is a relatively high transfer from the advance velocity disturbance to the shaft speed. At higher frequencies, for instance at $4 rad\, s^{-1}$, the gain is roughly $-20 dB$. This indicates a low transfer from advance velocity disturbance to shaft speed. This means that the shaft speed reacts much more to advance velocity disturbances with a lower frequency. Since the observers use measurements of the shaft speed to estimate the advance velocity, disturbances in v_a should be much harder to detect by the observers at higher frequencies. This is a direct result of the slope of $-20\ dB\ dec^{-1}$ after the fastest pole, being the pole corresponding to the shaft speed. The third figure shows the transfer from the advance velocity disturbance to the ship speed.

Table 2-13: Poles and zeros for $\frac{v_s}{u_x}$

Working Point	Poles	Zeros	DC-gain [−]
A	−0.0091, −0.1392	−0.0592	−0.6254
B	−0.0216, −0.3373	−0.1047	−0.5503
C	−0.0097, −0.5576	−0.0623	−0.1987
D	−0.0265, −1.5578	−0.1147	−0.1399

This contains two poles and one zero. The DC-gain is higher if the linearization point of the propeller pitch is lower. At higher frequencies, the gain is higher with a higher linearization point of the shaft speed. This makes sense, since a high shaft speed will react more to changes in the advance velocity than a low shaft speed. A slope of $-20 dB\, dec^{-1}$ is found beyond the fastest pole. The fourth and final figure shows the transfer from the advance velocity disturbance to the measured shaft torque.

Table 2-14: Poles and zeros for $\frac{M_m}{u_x}$

Working Point	Poles	Zeros	DC-gain $[N\ s]$
A	−0.0091, −0.1392	−0.0039, −0.0438	−1068.6
B	−0.0216, −0.3373	−0.0112, −0.0610	−739.1
C	−0.0097, −0.5576	−0.0081, −0.2996	−3541.4
D	−0.0265, −1.5578	−0.0236, −0.8060	−3653

This contains two poles and two zeros. This results in a flat response. This means a change in advance velocity has a large effect on the measured shaft torque, irrespective of the frequency. This is due to the presence of the two zeros. Again, the DC-gains are much higher than the other transfers, due to the different unit of the output signal.

2-8 Verification

In order to verify the model synthesized in this chapter, a parallel will be drawn to the model obtained in Vrijdag and Stapersma (2017) (henceforth referred to as "the Vrijdag paper"). In this paper, a ship propulsion model is derived, linearized and normalized. In order to compare the two linearized models, the model from the Vrijdag paper had to be slightly adjusted. Firstly, a state and input permutation was performed. Secondly, the normalization was removed. Thirdly, the shaft speed unit in the Vrijdag paper is rps, which had to be adjusted to $rad\ s^{-1}$. Finally, the Vrijdag paper does not use an advance velocity disturbance. Rather it directly applies the disturbance to the wake fraction w. A correction had to be applied to correct this difference. Next, the linear model derived in this chapter was linearized around the same inputs used in the Vrijdag paper. After these adjustments, it is possible to compare the two models using a Bode magnitude plot, which can be found in Figure 2-6.

Note that the Vrijdag paper does not include an output for the measured shaft torque. The magnitude plots will be discussed one by one in order to analyze the differences and similarities between the frequency responses. The first column in Figure 2-6 contains the transfer from the desired pitch to the three outputs. The first figure shows the transfer from the desired to the actual propeller pitch.

Table 2-15: Poles and zeros for $\frac{P/D}{P/D_d}$ of Vrijdag paper vs. this thesis

Plant	Poles	Zeros	DC-gain $[-]$
This thesis	−0.5	−	1
Vrijdag paper	−0.5	−	1

These transfers are identical, since both plants use a first order pitch actuator with the same time constant.

The second figure contains the transfer from the desired pitch to the shaft speed.

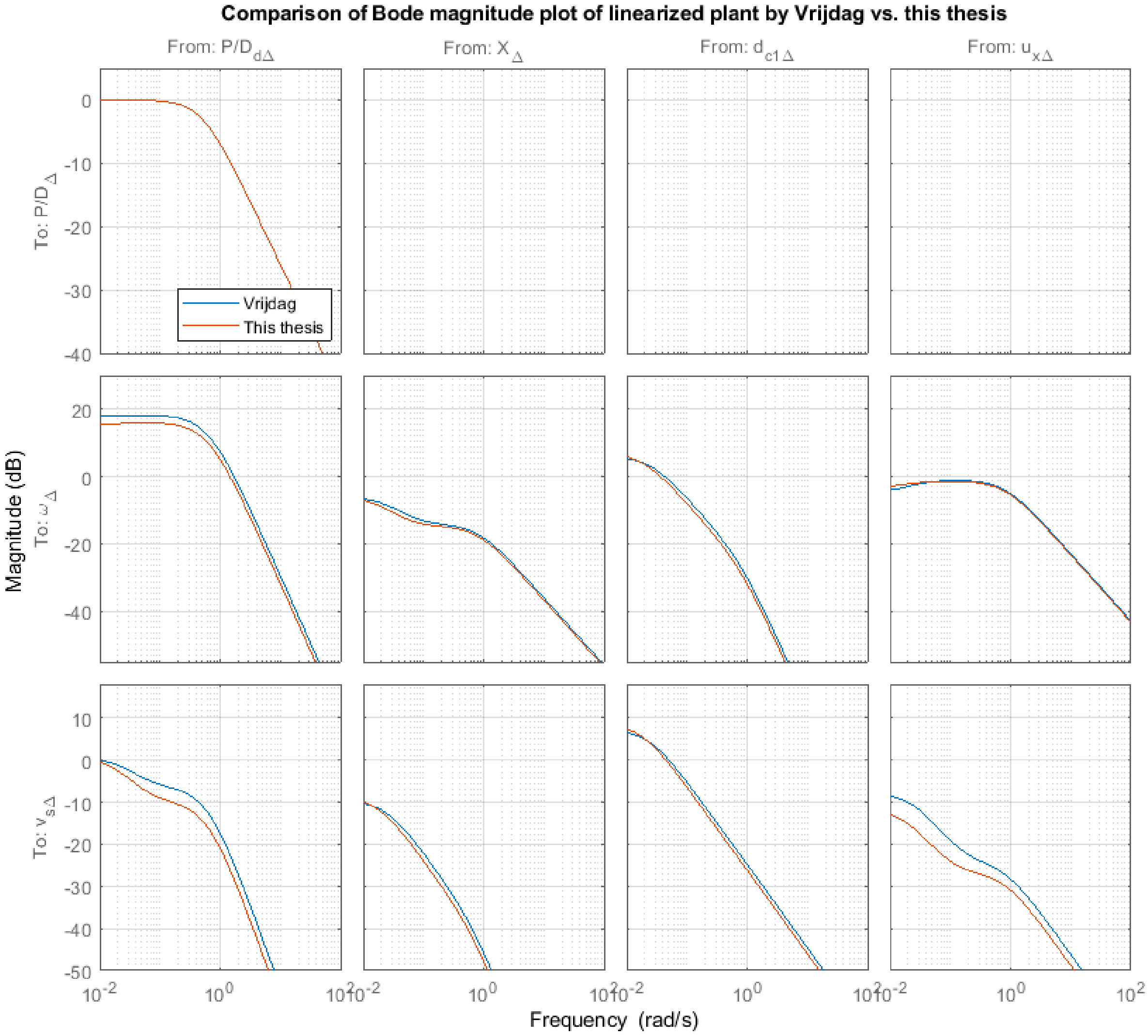

Figure 2-6: Bode plot of linearized ship propulsion system from this paper vs. Vrijdag paper [1]

Table 2-16: Poles and zeros for $\frac{\omega}{{}^{P}/_{D_d}}$ of Vrijdag paper vs. this thesis

Plant	Poles	Zeros	DC-gain [$rad\ s^{-1}$]
This thesis	−0.0180, −0.5, −0.8043	−0.0162	−5.7504
Vrijdag paper	−0.0248, −0.5, −0.8146	−0.0232	−7.7414

Both systems show three zeros, and one pole. The poles, zeros, and DC-gains are nearly identical, resulting in very similar Bode plots, and near identical system behavior.

The third figure contains the transfer from the desired pitch to the ship speed.

Table 2-17: Poles and zeros for $\frac{v_s}{{}^{P}/_{D_d}}$ of Vrijdag paper vs. this thesis

Plant	Poles	Zeros	DC-gain [$m\ s^{-1}$]
This thesis	−0.0180, −0.5, −0.8043	−0.0599	1.0597
Vrijdag paper	−0.0248, −0.5, −0.8146	−0.0546	1.0510

Again, both systems contain three poles and one zero, with near identical values.

The second column shows the transfer from the fuel rack position to the three outputs. The first figure is once again empty, since there is no transfer from the fuel rack position to the propeller pitch. The second figure contains the transfer from the fuel rack position to the shaft speed.

Table 2-18: Poles and zeros for $\frac{\omega}{X}$ of Vrijdag paper vs. this thesis

Plant	Poles	Zeros	DC-gain [$rad\ s^{-1}\ mm^{-1}$]
This thesis	−0.0180, −0.8043	−0.0487	0.4948
Vrijdag paper	−0.0248, −0.8146	−0.0628	0.4953

This transfer contains two poles and one zero, since the pitch actuator is not in the transfer. Again, nearly identical values for the poles, zeros and DC-gains are found.

The third figure shows the transfer from the fuel rack position to the ship speed.

Table 2-19: Poles and zeros for $\frac{v_s}{X}$ of Vrijdag paper vs. this thesis

Plant	Poles	Zeros	DC-gain [$m\ s^{-1}\ mm^{-1}$]
This thesis	−0.0180, −0.8043	–	0.3613
Vrijdag paper	−0.0248, −0.8146	–	0.3286

This contains two poles and no zeros.

The third column shows the transfer from the ship resistance disturbance to the three outputs. Once again the first figure is empty, since the ship resistance disturbance has no influence on the propeller pitch. The second figure shows the transfer from the ship resistance disturbance to the shaft speed.

Table 2-20: Poles and zeros for $\frac{\omega}{d_{c_1}}$ of Vrijdag paper vs. this thesis

Plant	Poles	Zeros	DC-gain $[rad\ s^{-1}]$
This thesis	−0.0180, −0.8043	–	−2.2570
Vrijdag paper	−0.0248, −0.8146	–	−2.0098

Again, two very similar poles and no zeros are found, with a nearly identical DC-gain.

The third figure shows the transfer from the ship resistance disturbance to the ship speed.

Table 2-21: Poles and zeros for $\frac{v_s}{d_{c_1}}$ of Vrijdag paper vs. this thesis

Plant	Poles	Zeros	DC-gain $[m\ s^{-1}]$
This thesis	−0.0180, −0.8043	−0.7736	−2.6763
Vrijdag paper	−0.0248, −0.8146	−0.7766	−2.2734

This contains two poles and one zero, which are found at almost identical locations.

The fourth and final column shows the transfer from the advance velocity disturbance to the three outputs. Again the first figure is empty, since there is no transfer from the advance velocity disturbance to the propeller pitch. The second figure contains the transfer from the advance velocity disturbance to the shaft speed.

Table 2-22: Poles and zeros for $\frac{\omega}{u_x}$ of Vrijdag paper vs. this thesis

Plant	Poles	Zeros	DC-gain $[rad\ m^{-1}]$
This thesis	−0.0180, −0.8043	−0.0142	0.6719
Vrijdag paper	−0.0248, −0.8146	−0.0161	0.5764

The third and final figure shows the transfer from the advance velocity disturbance to the ship speed.

Table 2-23: Poles and zeros for $\frac{v_s}{X}$ of Vrijdag paper vs. this thesis

Plant	Poles	Zeros	DC-gain $[m\ s^{-1}\ mm^{-1}]$
This thesis	−0.0180, −0.8043	−0.1019	−0.2559
Vrijdag paper	−0.0248, −0.8146	−0.1643	−0.4006

Overall, the presented juxtaposition between the model derived in this paper and the model in the Vrijdag paper shows near identical systems. All transfer functions contain the same number of poles and zeros, which were found at near identical locations. Furthermore, the DC-gains between the models showed great similarity. The differences that are present between the two models are most likely the result of small differences in used parameters, such as the open water propeller diagrams or the engine parameters. Concluding, the high correlation between the magnitude plots and the values of the poles, zeros and DC-gains bodes well for the accuracy of the model derived and linearized in this thesis.

Now that the model has been verified against the model derived in the Vrijdag paper, the synthesis of advance velocity observers can commence in the next chapter.

Chapter 3

Observer Synthesis

This chapter covers the theory, implementation and tuning of several different types of advance velocity observers. The goal of the observers is to accurately estimate the advance velocity, even when disturbances on advance velocity or other variables are present. The observers that will be covered are: Luenberger Observer, Shaft Kalman Filter, Power Balance Estimator, Measured Shaft Acceleration Observer, I&I Observer and the Random Walk Kalman Filter. For each observer structure, first the method will be covered. Secondly, the properties of the observer will be highlighted. Thirdly, the tuning of the observer is discussed. Finally, a frequency analysis will be performed for each observer.

3-1 Luenberger Observer

The first observer under consideration is the Luenberger observer. This observer was applied to Fixed Pitch Propeller (FPP) propulsion systems by Smogeli et al. (2006) and Bakkeheim et al. (2007).

3-1-1 Method

The structure of this observer is shown in Figure 3-1.

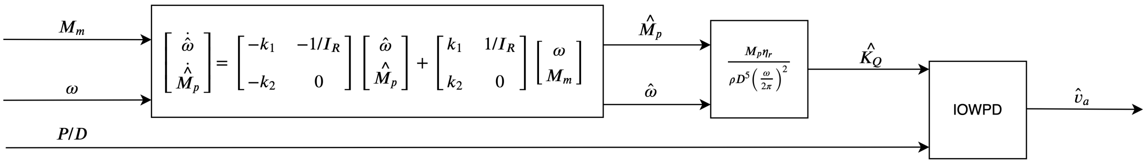

Figure 3-1: Block diagram of Luenberger observer

This observer uses dynamics of the shaft to estimate the propeller torque. The dynamics of the propeller shaft are defined in Eq. (2-18), and can be rewritten to yield:

$$\dot{\omega} = \frac{M_m - M_p}{I_R} \tag{3-1}$$

In this equation, M_m is a measured variable, but M_p is unknown. This can be solved by modeling the propeller torque as a Wiener process, where the change in the propeller torque is modeled as a zero mean white noise [14]:

$$\dot{M}_p = w_{M_p} \tag{3-2}$$

This results in the following state-space equation for the shaft:

$$\begin{aligned}
x &= \begin{bmatrix} \omega \\ M_p \end{bmatrix}, \quad u = M_m, \quad y = \omega \\
\dot{x} &= \begin{bmatrix} 0 & -1/I_R \\ 0 & 0 \end{bmatrix} x + \begin{bmatrix} 1/I_R \\ 0 \end{bmatrix} u + \begin{bmatrix} 0 \\ 1 \end{bmatrix} w_{M_p} \\
y &= \begin{bmatrix} 1 & 0 \end{bmatrix} x
\end{aligned} \tag{3-3}$$

The states are the shaft speed and the propeller torque, the input is the measured shaft torque and the noise is described by w_{M_p}. The measured output is defined as the shaft speed. This leads to the following observer equation:

$$\dot{\hat{x}} = A\hat{x} + Bu + K(y - \hat{y}) = (A - KC)\hat{x} + Bu + Ky \tag{3-4}$$

In this thesis, variables with a hat indicate the variable or state is estimated. The observer equation results in:

$$\begin{aligned}
\hat{x} &= \begin{bmatrix} \hat{\omega} \\ \hat{M}_p \end{bmatrix}, \quad u = \begin{bmatrix} \omega \\ M_m \end{bmatrix} \\
\dot{\hat{x}} &= \begin{bmatrix} -k_1 & -1/I_R \\ -k_2 & 0 \end{bmatrix} \hat{x} + \begin{bmatrix} k_1 & 1/I_R \\ k_2 & 0 \end{bmatrix} u
\end{aligned} \tag{3-5}$$

The inputs to the observer are the measured shaft speed and the measured shaft torque. The states of the observer are the estimated shaft speed and the estimated propeller torque. This ensures the correct variables are available to the observer through the input, and the estimated propeller torque and shaft speed are available as states. This observer structure results in the following error dynamics:

$$\dot{\tilde{x}} = \dot{x} - \dot{\hat{x}} = (A - KC)\tilde{x} \tag{3-6}$$

The error must asymptotically approach zero, so the error dynamics must be asymptotically stable. Therefore, the observer gains must be chosen such that $A - KC$ is Hurwitz.

After the propeller torque has been calculated, it is possible to estimate the advance velocity. The estimated shaft speed and propeller torque are used to calculate the estimated torque coefficient, with an altered version of Eq. (2-5):

$$\hat{K}_Q(\hat{J}(\hat{\omega}, \hat{v}_a), {}^{P}\!/_{D}) = \frac{\hat{M}_p \eta_r}{\rho D^5 \frac{\hat{\omega}}{2\pi}^2} \tag{3-7}$$

This results in the estimated torque coefficient. Next, the Inverse Open Water Propeller Diagrams (IOWPD) can be used to determine the estimated advance ratio. It is only possible to invert the open water propeller diagram if it is monotonic. In other words, if a certain torque coefficient and pitch can result in two or more possible advance ratios, this means that part of the open water propeller diagram is not monotonic. In this case, it becomes unclear which advance ratio is the correct value. Fortunately, as long as the $^P/_D$ remains between 0.6 and 1.4 and the propeller operation remains in the first quadrant, the open-water propeller diagram remains monotonic. Propeller operation in the first quadrant means that both the advance velocity and shaft speed remain positive. In this thesis and during normal operation of a ship propulsion system, all these conditions are met at all times. This means the open-water propeller diagram is always monotonic and therefore invertible. After the estimated advance ratio is known, the estimated advance velocity is calculated using:

$$\hat{v}_a = \frac{\hat{\omega}}{2\pi}\hat{J}(\hat{\omega}, \hat{v}_a)D \tag{3-8}$$

This results in the estimated advance velocity.

3-1-2 Properties

The Luenberger observer is a simple observer structure, that can be easily tuned to alter its performance. Any value for k_1 and k_2 that ensures that $(A - KC)$ is Hurwitz, will lead to an asymptotically stable observer. If higher gains are chosen, the observer will react more quickly to errors between the observed and actual output. However, this also means the observer will become more sensitive to noise. Therefore, the tuning of this observer, as is the case with many observers, concerns the trade off between a quick response and a good noise rejection. Due to the fact that the gains can be directly altered, the behavior of the system with different observer gains is very transparent. This can be used to gain insight into the system and observer. This is different from e.g. a Kalman filter, where the gains are not directly tuned, but the covariance of the noise is altered. Usually, for this observer, instead of directly tuning the gains k_1 and k_2, the poles of $A - KC$ are placed at a convenient location. This will be further highlighted in Section 3-1-3.

The observer requires the following data to estimate the advance velocity: measured shaft speed, measured shaft torque, propeller pitch, shaft inertia, density of seawater, propeller diameter and inverse open water propeller diagrams. Usually, in a real scenario, it is not very difficult to obtain these data. However, it should be noted that this approach relies heavily on the reliability and accuracy of the open water propeller diagram.

3-1-3 Tuning

The choice was made to show a juxtaposition of three different observer tunings. The first tuning contains very high gains, to show how the observer will respond with very fast dynamics. The second tuning has lower gains, to show slower dynamics, but a better noise rejection. A third tuning wil feature moderate gains, to approach a more realistic tuning. In essence, higher gains mean the measurements are trusted more than the model the observer is based upon, and vice versa. A result of this is that it is also possible to tune the observer to the expected disturbances. If the shaft speed measurement is trusted more, k_1 can be lower. However, this does not work in the same way for the shaft torque. The gain k_2 has an influence on how quickly the propeller torque can change, not on the trust placed in the measurement of shaft torque. This is due to the fact that the shaft torque is not an output of the shaft model, contrary to the shaft speed. The gains are obtained using pole placement. The MATLAB command `place` is used to obtain a gain K that will place the eigenvalues of $A - KC$ at the desired location. All eigenvalues of $A - KC$ must be smaller than zero. If this is the case, then $A - KC$ is Hurwitz, and the estimated states will always asymptotically converge to the real values. This means the observer itself is asymptotically stable. If the eigenvalues are chosen to be zero or higher than zero, the observer will marginally stable or unstable, respectively. This means the estimated states will not always converge to the real values, and might even diverge, blowing up to infinity. This could lead to a highly unstable observer. The further left the poles are placed in the imaginary plane, the quicker the observer dynamics, but the lower the noise rejection will be. This presents a trade off between noise rejection and quick observer dynamics.

For the first tuning, the observer poles are chosen very far left from the imaginary axis, e.g. with poles at $p_{1,2} = [-10^5 \quad -10^4]$. This results in a very high gain of $K = [1.1 \cdot 10^5 \quad -1.4 \cdot 10^{13}]$. If the poles of $A - KC$ are placed closer to the imaginary axis, the observer dynamics should be slower, but react less intensely to noise. To examine this, for the second tuning the poles of $A - KC$ were placed at $p_{1,2} = [-10 \quad -1]$. This results in a much lower gain of $K = [1.1 \cdot 10 \quad -1.4 \cdot 10^5]$.

In order to provide a fair comparison with the other observers, a moderate tuning was also created. This tuning features moderate gains, in order to provide a balance between noise rejection and time domain performance. This tuning had its poles at $p_{1,2} = [-10^2 \quad -10]$. This resulted in a gain of $K = [1.1 \cdot 10^2 \quad -1.4 \cdot 10^7]$.

3-1-4 Frequency Analysis

In order to compare the behavior of the observer with different gains in the frequency domain, a Bode magnitude plot was created for all three gains. This can be found in Figure 3-2. The top left figure shows the transfer from the measured shaft speed to the estimated shaft speed. The most favorable Bode magnitude plot would show a flat line at 0 dB, indicating a perfect transfer from the measured shaft speed to the estimated shaft speed.

Table 3-1: Poles and zeros for $\frac{\hat{\omega}}{\omega}$ of Luenberger observer

Gain	Poles	Zeros	DC-gain [−]
Low	$-1, -10$	$-9.091 \cdot 10^{-1}$	1
Moderate	$-10, -10^2$	-9.091	1
High	$-10^4, -10^5$	$-9.091 \cdot 10^3$	1

This shows the poles are exactly where they were placed during the observer synthesis. Furthermore, the transfer contains one zero. First, the zero takes effect for all observers, but at a slightly higher frequency the slowest pole comes into effect as well, almost creating pole zero cancellation. Finally, the faster pole comes in to play at higher frequencies, leading to a slope of $-20\ dB\ dec^{-1}$ as the frequency goes to infinity. In the pictured range of $[10^{-2}\ 10^2]\ rad\ s^{-1}$, the gain is almost always 1 in this transfer, which is the DC-gain. Only the low gain observer shows a significant drop in magnitude at higher relevant frequencies because the pole is not as fast. Although all three tunings show this drop, it happens at the lowest frequency when the gain is lowest. This means all observers show a

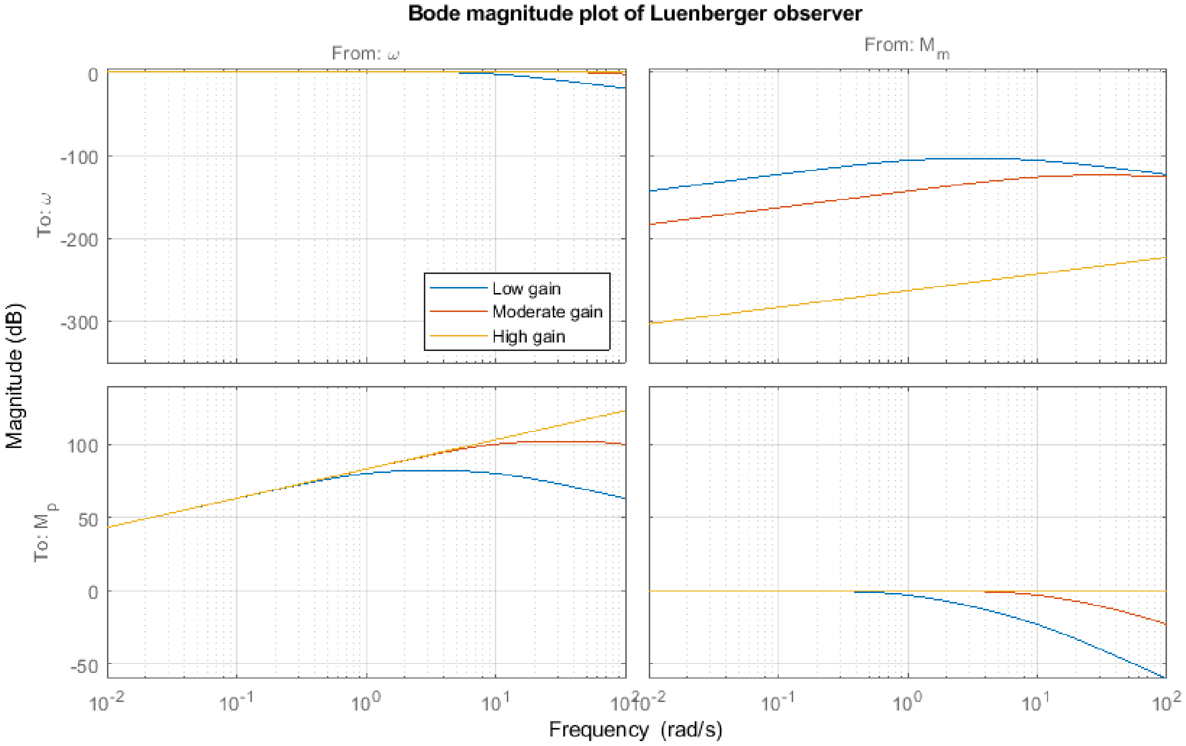

Figure 3-2: Bode magnitude plot of Luenberger observer

good transfer from the measured shaft speed to the estimated shaft speed at all relevant frequencies, except the low gain. This will show a deviation at higher frequencies.

The bottom left figure shows the transfer from the measured shaft speed to the estimated propeller torque.

Table 3-2: Poles and zeros for $\frac{\hat{M}_p}{\omega}$ of Luenberger observer

Gain	Poles	Zeros	DC-gain $[N\ m\ s\ rad^{-1}]$
Low	$-1, -10$	$1.55 \cdot 10^{-15}$	$2.24 \cdot 10^{-11}$
Moderate	$-10, -10^2$	$-1.28 \cdot 10^{-14}$	$-1.85 \cdot 10^{-10}$
High	$-10^4, -10^5$	$-1.40 \cdot 10^{-11}$	$-2.02 \cdot 10^{-7}$

This shows a very slow zero, and the poles where they were placed. This means the zero is in effect at very low frequencies, resulting in a slope of 20 $dB\ dec^{-1}$ at low frequencies. After the two poles, the slope to high frequencies is $-20\ dB\ dec^{-1}$.

The top right figure shows the transfer from the measured shaft torque to the estimated shaft speed.

Table 3-3: Poles and zeros for $\frac{\hat{\omega}}{M_m}$ of Luenberger observer

Gain	Poles	Zeros	DC-gain $[rad\ N^{-1}\ m^{-1}\ s^{-1}]$
Low	$-1, -10$	0	0
Moderate	$-10, -10^2$	0	0
High	$-10^4, -10^5$	0	0

This, again, shows the poles where they were placed during the controller synthesis. Furthermore, this transfer contains a zero at a frequency of 0 $rad\ s^{-1}$. This leads to a DC-gain of zero.

Finally, the bottom right figure shows the transfer from the measured shaft torque to the estimated propeller torque.

Table 3-4: Poles and zeros for $\frac{\hat{M}_p}{M_m}$ of Luenberger observer

Gain	Poles	Zeros	DC-gain $[-]$
Low	$-1, -10$	$-$	1
Moderate	$-10\ -10^2$	$-$	1
High	$-10^4, -10^5$	$-$	1

This contains the two poles, and no zeros. This results in a DC-gain of 1, and a slope of $-20\,dB\,dec^{-1}$ as the frequency goes to infinity. This concludes the frequency domain analysis of the Luenberger observer. The time domain performance of this observer will be investigated in Chapter 4-3.

3-2 Shaft Kalman Filter

The second observer is the Shaft Kalman Filter (SKF). This is a variation on the Luenberger observer, with a similar structure, but different observer gains.

3-2-1 Method

The structure of this observer is shown in Figure 3-3.

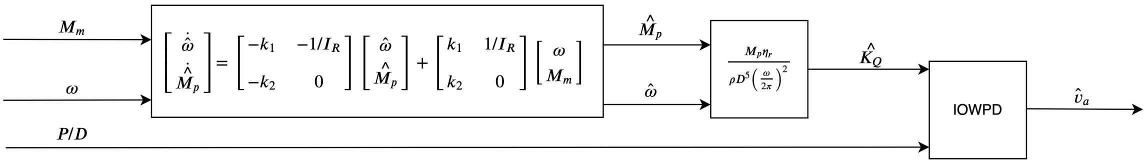

Figure 3-3: Block diagram of Shaft Kalman Filter

The Shaft Kalman filter is very similar to the Luenberger observer in its structure, but the way the gains are calculated are different. For this observer, the same structure as in Section 3-1 can be used. However, instead of directly providing the observer gains k_1 and k_2, the covariance of the noise present in the system is provided. Two noise covariances are defined: the output noise covariance $\boldsymbol{R}$, and the process noise covariance $\boldsymbol{Q}$. The output noise is noise that is applied to the measured output, in this case the shaft speed. The process noise is noise that is present in the system. In this case, the process noise on the propeller torque is much higher than the process noise on the shaft acceleration, since the change in propeller torque is driven by noise via a Wiener process. After the noise covariances are supplied, the Kalman gains are calculated to minimize the covariance of the error, as shown in [28, p. 162].

3-2-2 Properties

The Kalman filter is again straightforward to apply, but more difficult to tune than the Luenberger observer. The tuning of a Kalman filter can often be an iterative process, where the covariances are tuned based on the observer performance. The actual gains are calculated by solving an Algebraic Riccati Equation, which leads to a less intuitive relation between tuning variables and observer performance. However, when noise is present in the system, the Kalman filter aims to minimize the error covariance, which can be a powerful tool.

The data required by this observer includes the following: measured shaft speed, measured shaft torque, propeller pitch, shaft inertia, density of seawater, propeller diameter and inverse open water propeller diagrams. Similar to the Luenberger observer, all aforementioned information is usually readily available, but the accuracy and reliability of the open water propeller diagram is paramount to the accuracy and reliability of the observer.

3-2-3 Tuning

Since the Luenberger observer is used to provide insight into the effect tuning has on performance and noise rejection, the SKF will only be tuned to provide a good trade off between noise rejection and time domain performance. This will provide a fair comparison between the observers. The used process covariance is $Q = \mathtt{diag}[5 \quad 10^{13}]$, and the output covariance of the SKF is $R = 1$. It is possible to fine tune these covariances based on the expected measurement noise. If a lot of measurement noise on the shaft speed is expected, the output covariance should be higher, and vice versa.

3-2-4 Frequency Analysis

In order to analyze the frequency domain characteristics of the SKF, a Bode magnitude plot was created. This can be found in Figure 3-4. The top left figure shows the transfer from measured shaft speed to estimated shaft speed.

Table 3-5: Poles and zeros for $\frac{\hat{\omega}}{\omega}$ of Shaft Kalman Filter

Poles	Zeros	DC-gain [−]
$-10.53 \pm 10.41i$	-10.42	1

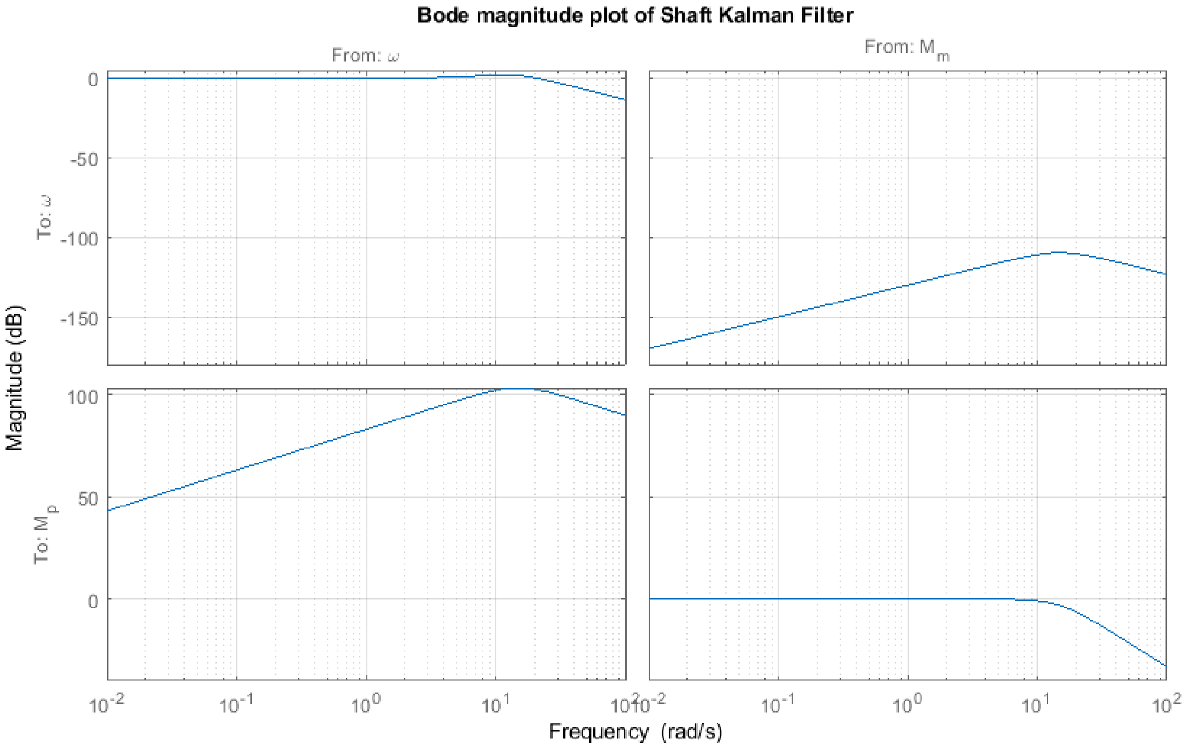

Figure 3-4: Bode magnitude plot of Shaft Kalman Filter

This shows the SKF contains a stable complex pole pair with a negative real part. Furthermore, this transfer contains one zero at roughly the same frequency as the complex pole pair. This means the magnitude stays around the DC-gain of 1 until the poles and zero are reached, at which point the magnitude drops at a slope of $-20\ dB\ dec^{-1}$.

The top right figure shows the transfer from measured shaft torque to estimated shaft speed. Again, the most favorable Bode magnitude plot would show a flat line at 0 dB, indicating a perfect transfer from the measured shaft speed to the estimated shaft speed.

Table 3-6: Poles and zeros for $\frac{\hat{\omega}}{M_m}$ of Shaft Kalman Filter

Poles	Zeros	DC-gain $[rad\ N^{-1}\ m^{-1}\ s^{-1}]$
$-10.53 \pm 10.41i$	0	0

This shows the same complex pole pair, but with a zero at 0. This means the magnitude has a slope of $20\ dB\ dec^{-1}$ before the pole pair, and a slope of $-20\ dB\ dec^{-1}$ after the pole pair. The zero at 0 also brings a DC-gain of zero.

The bottom left figure shows the transfer from measured shaft speed to estimated propeller torque.

Table 3-7: Poles and zeros for $\frac{\hat{M}_p}{\omega}$ of Shaft Kalman Filter

Poles	Zeros	DC-gain $[N\ m\ s\ rad^{-1}]$
$-10.53 \pm 10.41i$	$4.06 \cdot 10^{-15}$	$5.85 \cdot 10^{-11}$

This transfer contains the same complex pole pair, and a very slow zero at $4.06 \cdot 10^{-15}$. This results in a very small DC-gain, and the same slopes as the transfer from measured shaft torque to estimated shaft speed. The bottom right figure shows the transfer from measured shaft torque to estimated propeller torque.

Table 3-8: Poles and zeros for $\frac{\hat{M}_p}{M_m}$ of Shaft Kalman Filter

Poles	Zeros	DC-gain $[-]$
$-10.53 \pm 10.41i$	–	1

This contains the complex pole pair and no zeros. This results in a constant magnitude until the complex pole pair, after which the magnitude drops at $-40dBdec^{-1}$. This transfer has a DC-gain of 1. This concludes the frequency domain analysis of the Shaft Kalman Filter. The time domain performance of this observer will be investigated in Chapter 4-3.

3-3 Power Balance Estimator

The third estimator is the Power Balance Estimator (PBE). This observer was applied to a ship propulsion system by Brevik (2016), and to wind turbine systems by Soltani et al. (2013).

3-3-1 Method

The structure of this observer is shown in Figure 3-5.

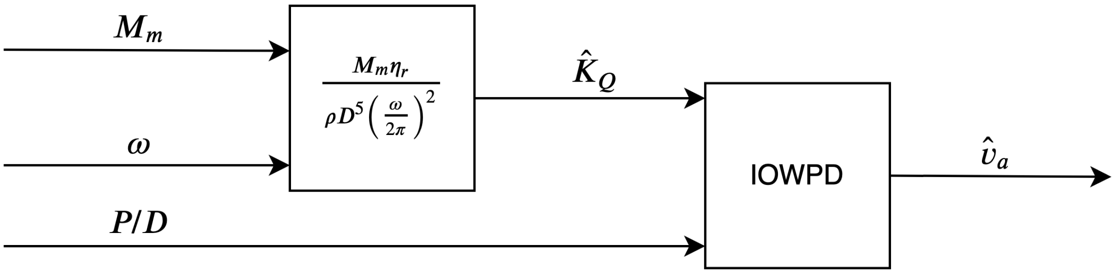

Figure 3-5: Block diagram of Power Balance Estimator

The PBE is probably the most simple estimator. It assumes that there are no dynamics present in the system, and neglects the acceleration of the propeller shaft. This can be shown using Eq. (2-18):

$$M_m = \cancelto{0}{\dot{\omega} I_R} + M_p \tag{3-9}$$

This means in Eq. (2-18), $\dot{\omega}$ is zero, and therefore $M_m = M_p$. The shaft torque is available for measurement, and therefore, the advance velocity can be calculated in the same manner as in Section 3-1-1.

3-3-2 Properties

Due to the fact that shaft accelerations are neglected, the PBE should be relatively accurate when the shaft speed does not change. However, when a large shaft acceleration is present, the second term in Eq. (3-9) becomes large enough to lead to inaccuracies in the advance velocity estimation. Due to its nature, no observer tuning is required or even possible.

This observer requires less information than the previous observers, since the shaft inertia is not required to calculate the propeller torque. This only leaves: measured shaft speed, measured shaft torque, propeller pitch, density of seawater, propeller diameter and inverse open water propeller diagrams. The PBE does not provide an estimate of the shaft speed, while e.g. the Kalman Filter does provide this estimate. This means that this observer will not attempt to remove any noise in the measured shaft speed. Again, although the aforementioned information is usually readily available, it should be noted that this observer is only as accurate and reliable as the open water propeller diagram it is based upon.

3-3-3 Tuning

As explained in Section 3-3-2, the Power Balance Estimator cannot be tuned.

3-3-4 Frequency Analysis

Due to the fact that the PBE contains no dynamics, it is not insightful to perform a frequency analysis. The output is a direct function of the input. Therefore, the transfer from inputs to outputs would be a constant gain, dependent on the working point of the observer. The time domain performance of this observer will be investigated in Chapter 4-3.

3-4 Measured Shaft Acceleration

The fourth estimator is the Measured Shaft Acceleration (MSA) observer. This observer relies on measurements of shaft acceleration to estimate the advance velocity.

3-4-1 Method

The structure of this observer is shown in Figure 3-6.

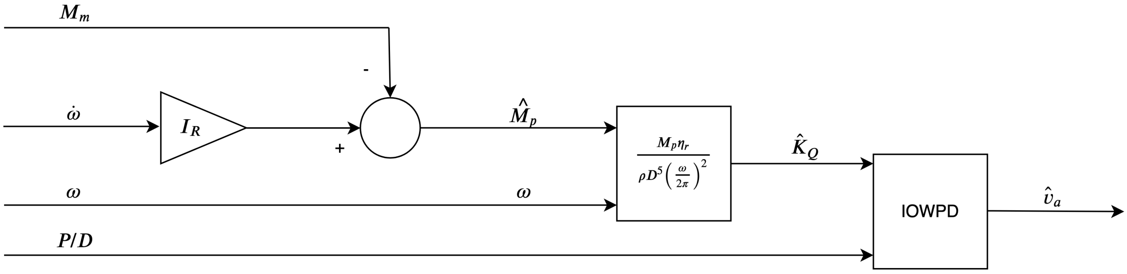

Figure 3-6: Block diagram of MSA observer

The MSA observer makes use of the assumption that not only the shaft speed but also the shaft acceleration is available as a measurement. This means the propeller torque can be directly calculated using an altered version of Eq. (2-18):

$$M_p = M_m - I_R \dot{\omega} \tag{3-10}$$

After this, the advance velocity can be calculated in the same manner as in Section 3-1-1.

3-4-2 Properties

Due to the nature of this observer, no observer tuning is required or possible. A problem with the MSA observer is the acquisition of the information regarding shaft acceleration. Direct differentiation of the measured shaft speed to obtain the shaft acceleration is not practically possible, since differentiation highly amplifies noise present in a signal. Therefore, the ship must contain a sensor specifically designed to measure the shaft acceleration for this observer to be feasible. This means that a change to the system is likely necessary to use this observer, since besides measurements of shaft speed, a measurement of shaft acceleration is also required. In order to illustrate the difficulty in taking the derivative of the shaft speed to acquire the shaft acceleration, a variation on the MSA is also implemented. This variation does not use a measurement of the shaft acceleration, but rather the derivative of the shaft speed. This is calculated using the following transfer function:

$$\frac{\dot{\omega}}{\omega} = \frac{s}{0.1s + 1} \tag{3-11}$$

The choice was made to use a time constant of 0.1 to calculate the derivative, since the highest frequency disturbance that is expected has a frequency of $4\,rad\ s^{-1}$. This ensures all relevant frequencies are included in the derivative, but higher frequencies originating from sensor noise are omitted in the derivative. This time constant can be tuned, with a lower time constant leading to more accurate time domain tracking, but less robustness to noise. Higher time constants will lead to less accurate time domain advance velocity tracking, but to more measurement noise robustness. This leads to the aforementioned trade off in observer design.

In Chapter 4, a comparison will be made between the observer with and without acceleration measurements.

This observer requires the following data: measured shaft speed and acceleration, measured shaft torque, propeller pitch, shaft inertia, density of seawater, propeller diameter and inverse open water propeller diagrams. Furthermore, this observer also does not provide an estimate of the shaft speed. Finally, the model synthesized in Section 2-6 contains a first order model of the propeller shaft, neglecting any torsional vibrations in the propeller shaft. In a real scenario, these torsional vibrations originating from the diesel engine could negatively affect the accuracy of the MSA observer. As with other observers, the accuracy of the open water propeller diagrams is crucial for the performance of this observer.

3-4-3 Tuning

As explained in Section 3-4-2, the Measured Shaft Acceleration Observer cannot be tuned.

3-4-4 Frequency Analysis

Again, due to the fact that the observer contains no dynamics, a frequency analysis would not provide any useful insight. The advance velocity is a direct function of the inputs, leading to a static gain based on the working point of the observer. The time domain performance of this observer will be investigated in Chapter 4-3.

3-5 I&I Observer

The fifth observer is the Immersion and Invariance (I&I) observer. This observer was applied to wind turbine systems by Ortega et al. (2012). Here, it was used to directly estimate the effective wind speed for a wind turbine system, where only the generator torque and the shaft speed were available for measurement. As this is very similar to the system treated in this thesis, the same observer will be applied to examine its performance.

3-5-1 Method

The structure of this observer is shown in Figure 3-7.

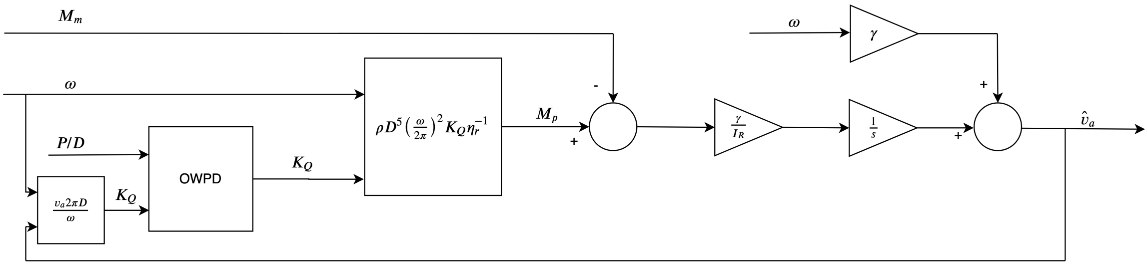

Figure 3-7: Block diagram of I&I observer

The observer consists of two equations:

$$
\begin{aligned}
\dot{\hat{\zeta}} &= \gamma \left(\frac{M_p - M_m}{I_R} \right) \\
\hat{v}_a &= \hat{\zeta} + \gamma \omega
\end{aligned}
\tag{3-12}
$$

Here, M_m is the measured shaft torque and M_p is the propeller torque. The propeller torque can be calculated using the estimated advance velocity and the measured shaft speed, using the open water propeller diagrams in combination with Eq. (2-6). Substituting Eq. (2-6) in Eq. (3-12) gives:

$$\begin{aligned}\dot{\hat{\zeta}} &= \gamma \left(\frac{\rho D^5 \left(\frac{\omega}{2\pi}\right)^2 K_Q(J(\omega, \hat{v}_a), {}^{P}\!/\!{}_{D})\eta_r^{-1} - M_m}{I_R} \right) \\ \hat{v}_a &= \hat{\zeta} + \gamma\omega\end{aligned} \tag{3-13}$$

Here, ζ represents the scaled shaft speed, and γ is the I&I tuning gain.

3-5-2 Properties

The I&I observer requires the following information on the system: measured shaft speed, measured shaft torque, propeller pitch, shaft inertia, density of seawater, propeller diameter and open water propeller diagrams. However, no inverse open water propeller diagram is required. This means the open water propeller diagram does not need to be monotonic, as it does not need to be inverted. As the observer only contains one tuning variable, γ, the observer is easy to tune. Higher values will lead to a more aggressive observer which will respond well to high frequency disturbances. On the other hand, higher gains will also lead to more noise in the estimated signals. Once again, this presents a trade off between tracking performance and noise rejection. This observer also does not provide an estimate of the shaft speed. Once more, much trust is placed in the accuracy of the open water propeller diagram. Inaccuracies in this diagram will lead to inaccuracies of the observer.

3-5-3 Tuning

In order to judge the performance of this estimator, a juxtaposition of three different observer tunings will be made, similar to the Luenberger observer. The first tuning will have a very high γ, which results in a very accurate and quick estimation, but will result in a high sensitivity to noise. The second tuning will have a lower γ, which results in slower observer dynamics, but a more robust response to measurement noise. The third and final tuning will contain a moderate gain, to provide a trade off between noise rejection and quick dynamics. The high gain was chosen to be $\gamma = 20$, the moderate gain is $\gamma = 4$ and the low gain is $\gamma = 1$.

3-5-4 Frequency Analysis

In order to analyze the I&I observer in the frequency domain, the observer was linearized and a Bode magnitude plot was created. This plot can be found in Figure 3-8. Only two working points and two gains are shown, to provide a clear picture. The left figure shows the transfer from the measured shaft speed to the estimated advance velocity.

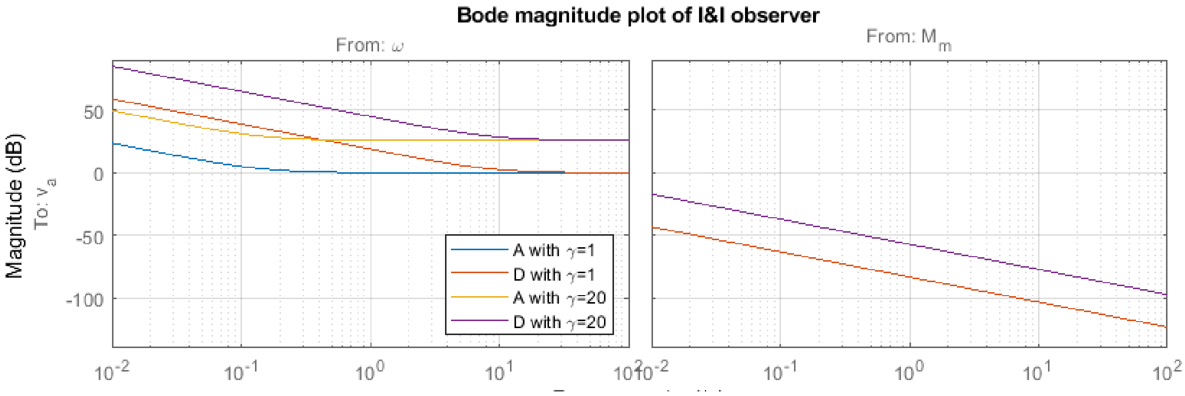

Figure 3-8: Bode magnitude plot of I&I observer

Table 3-9: Poles and zeros for $\frac{\hat{v}_a}{\omega}$ of I&I observer

Working point	Gain	Poles	Zeros	DC-gain $[m\, rad^{-1}]$
A	1	0	-0.1481	∞
D	1	0	-8.6677	∞
A	20	0	-0.1481	∞
D	20	0	-8.6677	∞

This shows that this transfer contains a pole at $0\, rad\ s^{-1}$, and a zero at -0.1481 or -8.6677, depending on the linearization point of the observer. Changing the gain has no effect on the location of the poles. Raising the gain does raise the DC-gain, as can be seen from Figure 3-8. However, the DC-gain is always infinity, due to the pole at zero.

The right figure shows the transfer from the measured shaft torque to the estimated advance velocity.

Table 3-10: Poles and zeros for $\frac{\hat{v}_a}{M_m}$ of I&I observer

Working point	Gain	Poles	Zeros	DC-gain $[N^{-1}\ s^{-1}]$
A	1	0	–	∞
D	1	0	–	∞
A	20	0	–	∞
D	20	0	–	∞

This transfer contains a pole at $0\ rad\ s^{-1}$, and no zeros. Again, increasing the gain does increase the DC-gain, as can be seen from Figure 3-8. This transfer has a DC-gain of infinity, again due to the pole at zero. This concludes the frequency domain analysis of the I&I observer. The time domain performance of this observer will be investigated in Chapter 4-3.

3-6 Random Walk Kalman Filter

The sixth and final observer is the Random Walk Kalman Filter (RWKF). This observer was applied to wind turbine systems by Selvam et al. (2009).

3-6-1 Method

The structure of this observer is shown in Figure 3-9.

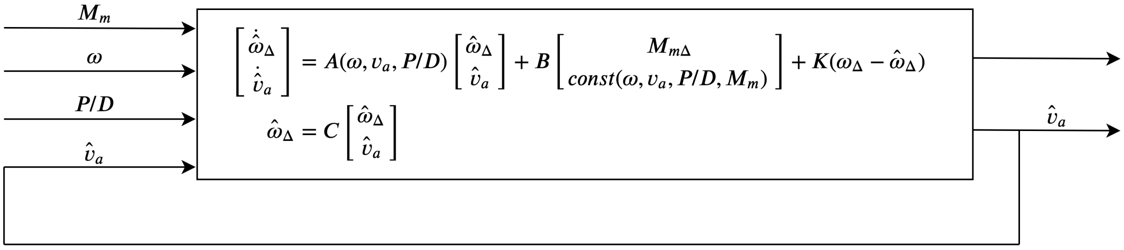

Figure 3-9: Block diagram of Random Walk Kalman Filter

The RWKF is unlike any other observer treated in this thesis. This observer uses a linearized version of the shaft differential equation in combination with a random walk model to observe the advance velocity. The observer synthesis starts with Eq. (2-18):

$$\dot{\omega} I_R = M_m - M_p \tag{3-14}$$

Next, the propeller torque from Eq. (2-5) can be substituted for M_p, and both sides can be divided by I_R:

$$\dot{\omega} = \frac{M_m - \rho D^5 \left(\frac{\omega}{2\pi}\right)^2 K_Q(J(\omega, v_a), {}^{P}\!/{}_{D})\eta_r^{-1}}{I_R} \tag{3-15}$$

This is the first differential equation needed to create the observer. Unfortunately, the measured torque M_m also changes with a changing shaft speed, so a second differential equation must be created. This is performed by substituting Eq. (2-17) into Eq. (3-15):

$$\dot{\omega} = \frac{M_b i_{gb} \eta_{trm} - \dot{\omega} I_L - \rho D^5 \left(\frac{\omega}{2\pi}\right)^2 K_Q(J(\omega, v_a), {}^{P}\!/{}_{D})\eta_r^{-1}}{I_R} \tag{3-16}$$

Next, $\dot{\omega}$ can be moved to the left side, and Eq. (2-13) can be substituted into Eq. (3-16):

$$\dot{\omega} = \frac{(a i_{gb} \omega + bX + c) i_{gb} \eta_{trm} - \rho D^5 \left(\frac{\omega}{2\pi}\right)^2 K_Q(J(\omega, v_a), {}^{P}\!/{}_{D})\eta_r^{-1}}{I} \tag{3-17}$$

This results in the second differential equation needed to create the observer, which is identical to the shaft speed in Eq. (2-20). Next, the goal is to include a random walk algorithm to observe the advance velocity. Therefore, besides ω, an extra state v_a, the advance velocity, is added. The input to the observer is the measured shaft torque. Therefore, in order to linearize this nonlinear differential equation, the differential equations must be linearized to the shaft speed, advance velocity and shaft torque. Firstly, because Eq. (3-15) contains the measured shaft torque in its original form, this equation will be used for the constant term and for the linearization to the measured shaft torque and the advance velocity. Secondly, because Eq. (3-17) contains only the shaft speed and not the measured torque, this equation will be used to linearize to the shaft speed. This results in the following linearized state-space representation of the shaft speed:

$$\begin{aligned}\dot{\omega}_\Delta = &\begin{bmatrix}\tfrac{1}{I}(ai_{gb}^2\eta_{trm} - \rho D^5 \tfrac{1}{4\pi^2}\eta_r^{-1}(2\omega_{eq}K_{Q,eq} + \omega_{eq}^2\tfrac{\delta K_{Q,eq}}{\delta \omega})) & -\tfrac{1}{I}\rho D^5 \tfrac{1}{4\pi^2}\eta_r^{-1}\omega_{eq}^2\tfrac{\delta K_{Q,eq}}{\delta v_a}\end{bmatrix}\begin{bmatrix}\omega_\Delta \\ v_{a\Delta}\end{bmatrix} \\ &+ \frac{1}{I_R}M_{m\Delta} + \frac{1}{I_R}(M_{m,eq} - \rho D^5 \frac{1}{4\pi^2}\eta_r^{-1}\omega_{eq}^2 K_{Q,eq})\end{aligned} \tag{3-18}$$

Since the random walk model does not need to be linearized, the state regarding the advance velocity does not concern a small deviation from the chosen equilibrium, but rather the advance velocity in its original form. However, in Eq. (3-18), the linearized version of the advance velocity is used. Therefore, a correction must be applied. Starting with the definition of the linearized state as found in Eq. (2-24):

$$v_a = v_{a,eq} + v_{a\Delta} \tag{3-19}$$

This means:

$$v_{a\Delta} = v_a - v_{a,eq} \tag{3-20}$$

Therefore, $v_{a\Delta}$ in Eq. (3-18) can be replaced by $v_a - v_{a,eq}$, resulting in an extra constant term:

$$\begin{aligned}\dot{\omega}_\Delta = &\begin{bmatrix}\tfrac{1}{I}(ai_{gb}^2\eta_{trm} - \rho D^5 \tfrac{1}{4\pi^2}\eta_r^{-1}(2\omega_{eq}K_{Q,eq} + \omega_{eq}^2\tfrac{\delta K_{Q,eq}}{\delta \omega})) & -\tfrac{1}{I_R}\rho D^5 \tfrac{1}{4\pi^2}\eta_r^{-1}\omega_{eq}^2\tfrac{\delta K_{Q,eq}}{\delta v_a}\end{bmatrix}\begin{bmatrix}\omega_\Delta \\ v_a\end{bmatrix} \\ &+ \frac{1}{I_R}M_{m\Delta} + \frac{1}{I_R}(M_{m,eq} - \rho D^5 \frac{1}{4\pi^2}\eta_r^{-1}\omega_{eq}^2 K_{Q,eq} + \rho D^5 \frac{1}{4\pi^2}\eta_r^{-1}\omega_{eq}^2\frac{\delta K_{Q,eq}}{\delta v_a}v_{a,eq})\end{aligned} \tag{3-21}$$

Next, the system can be appended with the random walk model for the advance velocity:

$$\begin{aligned}\begin{bmatrix}\dot{\omega}_\Delta \\ \dot{v}_a\end{bmatrix} = &\begin{bmatrix}\tfrac{1}{I}(ai_{gb}^2\eta_{trm} - \rho D^5 \tfrac{1}{4\pi^2}\eta_r^{-1}(2\omega_{eq}K_{Q,eq} + \omega_{eq}^2\tfrac{\delta K_{Q,eq}}{\delta \omega})) & -\tfrac{1}{I_R}\rho D^5 \tfrac{1}{4\pi^2}\eta_r^{-1}\omega_{eq}^2\tfrac{\delta K_{Q,eq}}{\delta v_a} \\ 0 & 1\end{bmatrix}\begin{bmatrix}\omega_\Delta \\ v_a\end{bmatrix} \\ &+ \begin{bmatrix}\tfrac{1}{I_R} \\ 0\end{bmatrix}M_{m\Delta} + \begin{bmatrix}\tfrac{1}{I_R}(M_{m,eq} - \rho D^5 \tfrac{1}{4\pi^2}\eta_r^{-1}\omega_{eq}^2 K_{Q,eq} + \rho D^5 \tfrac{1}{4\pi^2}\eta_r^{-1}\omega_{eq}^2\tfrac{\delta K_{Q,eq}}{\delta v_a}v_{a,eq}) \\ 0\end{bmatrix}\end{aligned} \tag{3-22}$$

Furthermore, in order to use a Kalman Filter, the measured output must be defined using the C-matrix. The measured output is the shaft speed, resulting in the following C-matrix:

$$y = \begin{bmatrix}1 & 0\end{bmatrix}\begin{bmatrix}\omega_\Delta \\ v_a\end{bmatrix} \tag{3-23}$$

In order to enter the constant terms into the Kalman Filter, a change to the B-matrix must be made.

The final state-space system of the Random Walk Kalman Filter:

$$
\begin{aligned}
x &= \begin{bmatrix} \omega_\Delta \\ \upsilon_a \end{bmatrix}, \quad u = M_{m\Delta} \\
\dot{x} &= \begin{bmatrix} \frac{1}{I}(ai_{gb}^2\eta_{trm} - \rho D^5 \frac{1}{4\pi^2}\eta_r^{-1}(2\omega_{eq}K_{Q,eq} + \omega_{eq}^2 \frac{\delta K_{Q,eq}}{\delta\omega})) & -\frac{1}{I_R}\rho D^5 \frac{1}{4\pi^2}\eta_r^{-1}\omega_{eq}^2 \frac{\delta K_{Q,eq}}{\delta \upsilon_a} \\ 0 & 1 \end{bmatrix} x \\
&+ \begin{bmatrix} \frac{1}{I_R} \\ 0 \end{bmatrix} u + \begin{bmatrix} \frac{1}{I_R}(M_{m,eq} - \rho D^5 \frac{1}{4\pi^2}\eta_r^{-1}\omega_{eq}^2 K_{Q,eq} + \rho D^5 \frac{1}{4\pi^2}\eta_r^{-1}\omega_{eq}^2 \frac{\delta K_{Q,eq}}{\delta \upsilon_a}\upsilon_{a,eq}) \\ 0 \end{bmatrix} \\
y &= \begin{bmatrix} 1 & 0 \end{bmatrix} x
\end{aligned}
\tag{3-24}
$$

This results in an A, B and C matrix, which can be used in a Kalman Filter. The inputs to the Kalman Filter are $u = 0$, since the system is linearized around the actual measured shaft torque, and therefore the deviation from the linearized value, $M_{m\Delta}$, is zero. The same holds for the measured output, since the system is linearized around the measured shaft speed, and therefore the difference between the shaft speed equilibrium and the actual measured shaft speed is zero. The Kalman Filter calculates the Kalman gains at each time step, and estimates the states of Eq. (3-24). The estimated advance velocity is entered back into the algorithm to calculate the state-space system, closing the loop. Since the first state is ω_Δ, the equilibrium value ω_{eq} must be added to the first state to yield the estimated shaft speed. This concludes the method of the Random Walk Kalman Filter.

3-6-2 Properties

Due to the unique nature of the RWKF, this observer requires different information. This includes: measured shaft speed, measured shaft torque, propeller pitch, shaft inertia, density of seawater, propeller diameter, gearbox ratio, transmission efficiency, relative rotative efficiency, engine parameters from Eq. (2-4) and open water propeller diagrams, as well as its derivatives. Contrary to most other observers, this observer does not require the inverse open water propeller diagrams. However, accuracy and reliability of the open water propeller diagrams and its derivatives is essential to the accuracy and reliability of the RWKF. This observer can be tuned by altering the process and measurement noise covariances of the Kalman Filter, similar to the SKF. This is an iterative process, since, due to the Kalman Filter, it is not possible to alter the gains of the observer directly. This does not provide much insight into the operation of the observer. The Luenberger observer is different in this respect, since this observer allows for direct manipulation of the observer gains.

3-6-3 Tuning

The tuning of complex observers is often an iterative process. Where the Luenberger observer can be tuned by directly altering the observer gains, this is not possible for the RWKF. An iterative process resulted in a process covariance $Q = \texttt{diag}[10^4 \quad 10^{11}]$ and an output noise covariance $R = 1$. This results in a trade off between time domain performance and noise rejection.

3-6-4 Frequency Analysis

In order to analyze the RWKF in the frequency domain, a Bode magnitude plot was created. This plot can be found in Figure 3-10. The top left figure shows the transfer from the measured shaft speed to

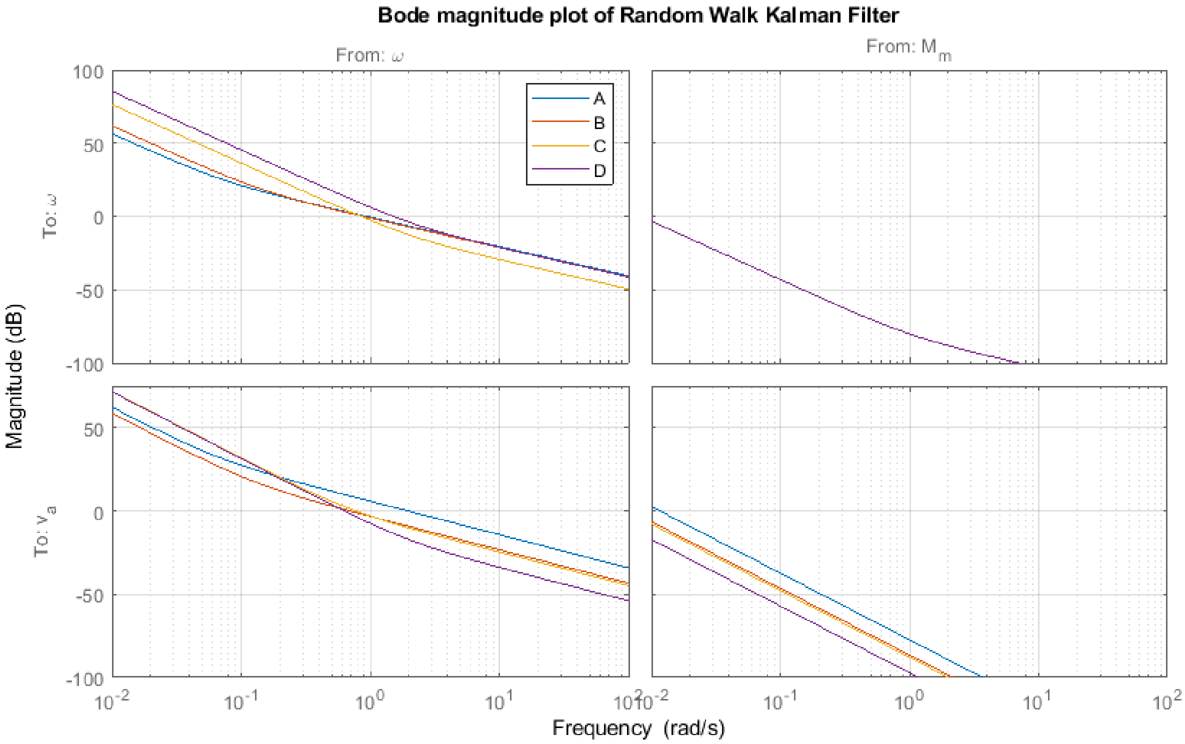

Figure 3-10: Bode magnitude plot of Random Walk Kalman Filter

the estimated shaft speed.

Table 3-11: Poles and zeros for $\frac{\hat{\omega}}{\omega}$ of RWKF

Working point	Poles	Zeros	DC-gain [−]
A	$-4.610 \cdot 10^{-10}, 3.795 \cdot 10^{-7}$	$-7.06 \cdot 10^{-2}$	$-3.77 \cdot 10^{14}$
B	$-1.577 \cdot 10^{-9}, 4.824 \cdot 10^{-8}$	$-1.414 \cdot 10^{-1}$	$-1.63 \cdot 10^{15}$
C	$7.112 \cdot 10^{-9}, 2.675 \cdot 10^{-8}$	1.983	$3.50 \cdot 10^{15}$
D	$-3.077 \cdot 10^{-9}, 7.074 \cdot 10^{-9}$	2.151	$-8.58 \cdot 10^{16}$

This contains two slow poles and a faster zero. This results in a slope of $-20\ dB\ dec^{-1}$ at higher frequencies, and a steeper slope of $-40\ dB\ dec^{-1}$ at frequencies slower than the zero. The top right figure shows the transfer from the measured shaft torque to the estimated shaft speed.

Table 3-12: Poles and zeros for $\frac{\hat{\omega}}{M_m}$ of RWKF

Working point	Poles	Zeros	DC-gain [$rad\ N^{-1}\ m^{-1}\ s^{-1}$]
A	$-4.610 \cdot 10^{-10}, 3.795 \cdot 10^{-7}$	1	$3.97 \cdot 10^{11}$
B	$-1.577 \cdot 10^{-9}, 4.824 \cdot 10^{-8}$	1	$9.12 \cdot 10^{11}$
C	$7.112 \cdot 10^{-9}, 2.675 \cdot 10^{-8}$	1	$-3.65 \cdot 10^{11}$
D	$-3.077 \cdot 10^{-9}, 7.074 \cdot 10^{-9}$	1	$3.19 \cdot 10^{12}$

This contains the same slow poles, and a zero at 1. The bottom left figure shows the transfer from the measured shaft speed to the estimated advance velocity.

Table 3-13: Poles and zeros for $\frac{\hat{v}_a}{\omega}$ of RWKF

Working point	Poles	Zeros	DC-gain $[m\ rad^{-1}]$
A	$-4.610 \cdot 10^{-10}, 3.795 \cdot 10^{-7}$	$-6.59 \cdot 10^{-2}$	$-7.33 \cdot 10^{14}$
B	$-1.577 \cdot 10^{-9}, 4.824 \cdot 10^{-8}$	$-1.239 \cdot 10^{-1}$	$-1.11 \cdot 10^{15}$
C	$7.112 \cdot 10^{-9}, 2.675 \cdot 10^{-8}$	$-6.648 \cdot 10^{-1}$	$2.03 \cdot 10^{15}$
D	$-3.077 \cdot 10^{-9}, 7.074 \cdot 10^{-9}$	-1.8686	$-1.72 \cdot 10^{16}$

This contains two slow poles, and a faster zero. This pole lies in the relevant region of the shaft speed. The bottom right figure shows the transfer from the measured shaft torque to the estimated advance velocity.

Table 3-14: Poles and zeros for $\frac{\hat{v}_a}{M_m}$ of RWKF

Working point	Poles	Zeros	DC-gain $[N^{-1}\ s^{-1}]$
A	$-4.610 \cdot 10^{-10}, 3.795 \cdot 10^{-7}$	–	$7.72 \cdot 10^{11}$
B	$-1.577 \cdot 10^{-9}, 4.824 \cdot 10^{-8}$	–	$6.23 \cdot 10^{11}$
C	$7.112 \cdot 10^{-9}, 2.675 \cdot 10^{-8}$	–	$-2.12 \cdot 10^{11}$
D	$-3.077 \cdot 10^{-9}, 7.074 \cdot 10^{-9}$	–	$6.37 \cdot 10^{11}$

This contains the same two slow poles, and no zeroes. This results in a slope of $-40\ dB\ dec^{-1}$ at higher frequencies. This concludes the frequency domain analysis of the RWKF. The time domain performance of this and all other observers will be investigated in the next chapter.

Chapter 4

Observer Performance

This chapter will cover the performance of the observers in the time domain. In order to provide an insightful comparison between the different observers, several different load cases are introduced in Section 4-1. After this, the performance evaluation metric is discussed in Section 4-2. Finally, the performance of the different observers is compared in Section 4-3.

4-1 Load Cases

Eight individual load cases are used to investigate the performance of the observers. These include:

1. Step on fuel rack position
2. Step on desired pitch ratio
3. Low frequency sine on advance velocity disturbance
4. High frequency sine on advance velocity disturbance
5. Sine on ship resistance disturbance
6. Ramp on ship resistance disturbance
7. JONSWAP wave spectrum on advance velocity disturbance
8. Measurement noise on observer inputs

All load cases are applied when the system is at an equilibrium, so when no acceleration or deceleration of the ship or the shaft is present at the start of the load case. The load cases are applied one by one to the corresponding input or disturbance. Only one input or disturbance is perturbed at a time, while all others are constant. For instance, if a step is put on the pitch $^{P}/_{D}$, all other inputs and disturbances are constant. The values that are used for these constant inputs and disturbances are $X = 22\ mm$, $^{P}/_{D_d} = 1.4$, $u_x = 0$ and $d_{c_1} = 1$. These constant inputs and disturbances result in a constant shaft and ship speed of $\omega = 10.51\ rad\ s^{-1}$ and $v_s = 8.73\ m\ s^{-1}$, respectively. Next, each individual load case will be highlighted.

4-1-1 Step on fuel rack position

The first load case includes a step on the fuel rack position X. This load case is used to observe the response of the observer to a sudden change in the input of the diesel engine. For the engine fuel rack position X, a step is made from 20 mm to 27.5 mm. This corresponds to a 24.62% increase in shaft speed at a pitch of ${}^{P}/_{D_d} = 1.4$. The step is made when the system has reached an equilibrium.

4-1-2 Step on desired pitch

The second load case is a step on the desired pitch angle ${}^{P}/_{D_d}$ to test the performance of the observers in the case of a rapidly changing setpoint for the pitch actuator. In this case, a downward step is made from ${}^{P}/_{D_d} = 1.25$ to ${}^{P}/_{D_d} = 1$. This corresponds to a 23.23% increase in shaft speed at a fuel rack position of $X = 22$ mm. Again, the step is made when the system has reached an equilibrium.

4-1-3 High and low frequency sine waves on advance velocity disturbance

The third and fourth load cases are sine waves on the advance velocity disturbance u_x. These load cases were chosen to gauge the performance of the observers when confronted with a sinusoidally changing disturbance on the advance velocity, which is common when waves are acting on the propulsion system. Two different sine waves are applied. Both have an amplitude of 1 $m\ s^{-1}$, but different frequencies. The first frequency is 0.15 $rad\ s^{-1}$, which is a frequency that results in a high gain from the advance velocity disturbance u_x to the shaft speed ω, as shown in Section 2-7-3, in the text accompanying Table 2-12. Since the observers use information from measurements of the shaft speed, a high gain between the advance velocity disturbance and the shaft speed should result in a more accurate estimate of the advance velocity. The second frequency that is used is 4 $rad\ s^{-1}$. This frequency corresponds to a lower gain from the advance velocity disturbance to the shaft speed as shown in Section 2-7-3, so it is expected that this frequency of disturbance results in a lower observer accuracy. Both frequencies are realistic wave encounter frequencies.

4-1-4 Ramp on ship resistance coefficient

The fifth load case is a ramp on the ship resistance coefficient d_{c_1}. This ramp is used to model a slowly increasing resistance, e.g. due to increasing wind. This disturbance moves linearly from $d_{c_1} = 1$ to $d_{c_1} = 1.75$ over the span of three minutes. Again, the step is made when the system has reached an equilibrium.

4-1-5 Sine wave on ship resistance coefficient

The sixth load case is a sine wave on the ship resistance coefficient. This sine is used to model the changing resistance on the hull of the ship due to clusters of waves. Since single waves have a very small impact on the ship speed due to the very large mass of the ship, only clusters of waves will significantly impact the ship speed. These clusters occur at a much lower frequency than the waves themselves, so the frequency of this sine wave was taken to be 0.0785 $rad\ s^{-1}$.

4-1-6 JONSWAP wave spectrum on advance velocity disturbance

The seventh load case uses a JONSWAP [29] wave spectrum which is applied to the advance velocity disturbance u_x. This load case is used to model a realistic scenario for actual waves. Here, head waves are simulated with a significant wave height of $2.9\ m$ and a peak period of $9.3s$ at 6 Beaufort, describing the wind speed. The immersion of the propeller centre is modeled at $-4\ m$. A pseudo random algorithm is applied, in order to ensure the waves are identical each time the algorithm is used. Head waves with a high wind speed are used to model a rough sea. This leads to high frequency and high amplitude disturbances on the advance velocity, increasing the difficulty of accurately estimating the advance velocity.

4-1-7 Measurement noise on observer inputs

In the eighth and final load case, noise is applied to the input signals of the observers, while a high frequency advance velocity disturbance is present. This load case is used to investigate whether the observers are resistant to noise on the measured inputs, during a challenging scenario with a high frequency advance velocity disturbance. Input measurement noise is a common occurrence when the inputs to the observers originate from sensors in the ship propulsion system. In order to simulate measurement noise, white Gaussian noise is applied in an additive manner to the observer inputs M_m, ω, $\dot{\omega}$ and $^P/_D$. The simulation is repeated with 20 different seeds of uncorrelated white noise on each observer input. The Signal to Noise Ratio (SNR) of the input signals is varied from $0\ dB$ to $100\ dB$, and the Variance Accounted For (VAF) is calculated for each SNR. This results in a plot showing the VAF for each value of the SNR. This is not a single line, but rather a range which is a result of the different noise seeds. In order to obtain a single metric for noise robustness, the SNR where a VAF of 95% of the noiseless VAF is reached, is calculated using the mean result of all noise seeds.

Figure 4-1 provides an overview of the different load cases, shown within the same time frame as the results.

4-2 Evaluation Metrics

In order to evaluate the performance of the different observers, the Variance Accounted For (VAF) and the Signal to Noise Ratio (SNR) are used.

The VAF is calculated using the following formula [28, p. 383]:

$$\text{VAF} = max\left(0, \left(1 - \frac{var(v_a - \hat{v}_a)}{var(v_a)}\right)\right) \cdot 100\% \tag{4-1}$$

This results in a percentage between 0 % and 100 %. A higher VAF means the observer is more accurate, and has a smaller estimation error.

The SNR is calculated using the following formula:

$$\text{SNR} = 10 \cdot log_{10} \frac{(\text{RMS}\,(signal))^2}{(\text{RMS}\,(noise))^2} \tag{4-2}$$

This results in a value in decibel. The lower the value, the more noisy the signal is. If the SNR is exactly 0 dB, the power of the noise is equal to the power of the signal.

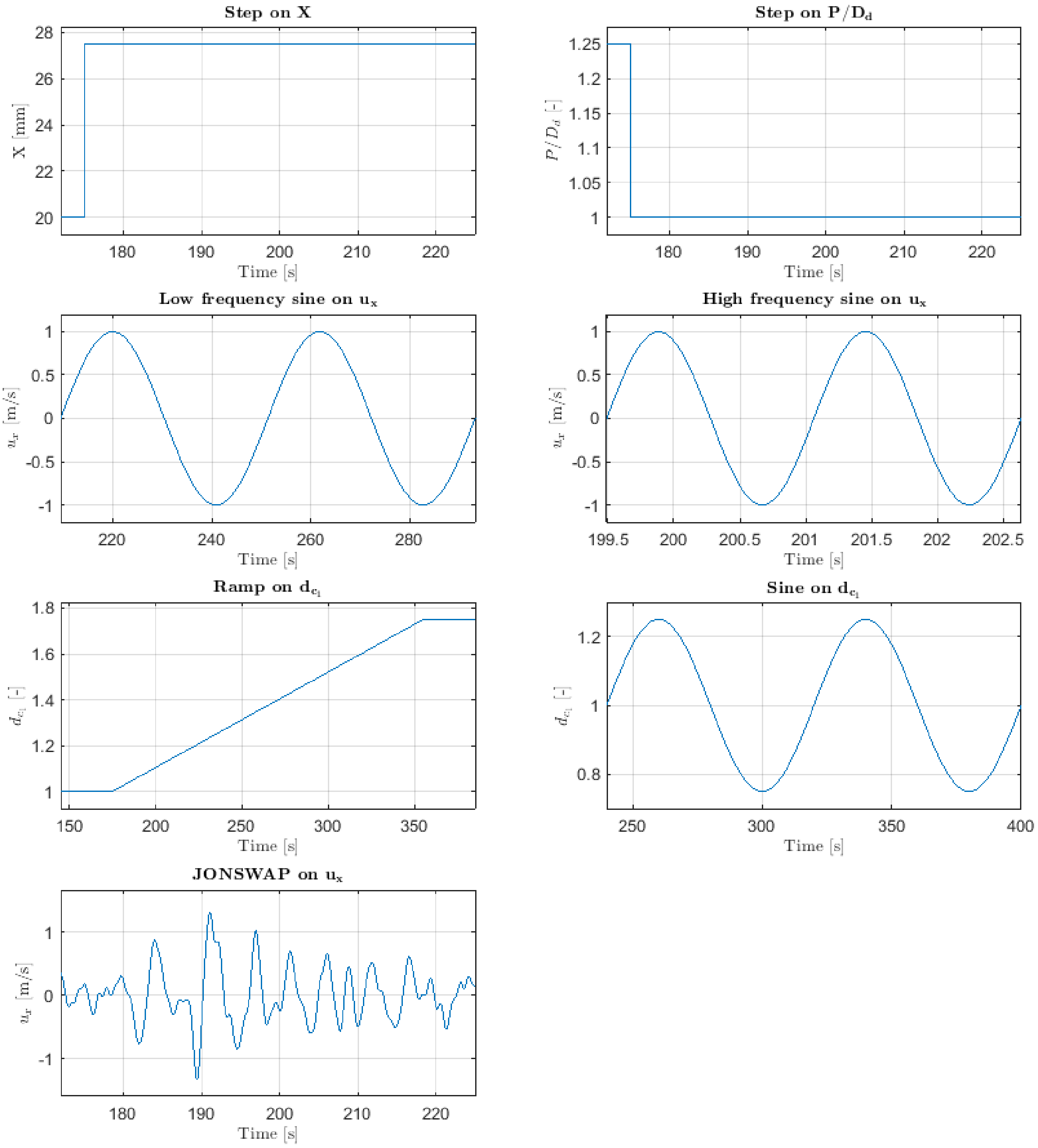

Figure 4-1: Overview of load cases

4-3 Performance Comparison

The eleven different combinations of observers and tunings were run with all test cases described in Section 4-1. The time domain results for the estimated advance velocity for all observers and tunings can be found in Appendix A-1. Table 4-1 shows the found VAF values for all combinations of test cases and observers. Furthermore, the average VAF and the Standard Deviation (SD) are also shown.

Table 4-1: VAF [%] values for each test case, including average and standard deviation

	X	${}^{P}/{}_{D_d}$	$u_x \sim \downarrow$	$u_x \sim \uparrow$	$d_{c_1} \diagup$	$d_{c_1} \sim$	JON.	Avg.	SD
Luenb. (low)	87.02	0	99.61	0	99.96	99.50	0	55.16	51.79
Luenb. (mod.)	99.81	79.79	99.88	82.89	99.96	99.61	97.00	94.13	8.85
Luenb. (high)	99.95	84.58	99.90	99.96	99.96	99.62	99.79	97.68	5.78
SKF	99.78	79.60	99.88	78.33	99.96	99.61	96.48	93.38	9.93
PBE	99.50	23.60	99.86	96.29	99.97	99.63	98.03	88.13	28.48
MSA	99.95	84.58	99.90	99.96	99.96	99.62	99.79	97.68	5.78
MSA without $\dot{\omega}$	99.91	84.22	99.89	99.43	99.96	99.62	99.68	97.53	5.87
I&I (low)	100	99.94	99.86	49.54	100	99.97	86.75	90.87	18.88
I&I (mod.)	100	100	99.99	93.73	100	100	98.90	98.95	2.34
I&I (high)	100	100	100	99.73	100	100	99.95	99.95	0.10
RWKF	99.53	74.18	99.92	95.66	100	99.98	97.13	95.20	9.42

This table contains color labeling to improve clarity. If the VAF value is VAF $< 90\%$, the color is red, indicating poor performance. If the VAF value is $90\% \leq$ VAF $< 97.5\%$, the color is orange, indicating moderate performance. If the VAF value is VAF $\geq 97.5\%$, the color is green, indicating good performance. This shows that some test cases are more difficult for the observers than others. The step on the fuel rack position is handled well by all observers, except the Luenberger observer with low gains. This observer shows a low VAF of 87.02%, while all other observers give a VAF of at least 99%. This is due to the fact that the Luenberger observer with low gains cannot keep up with fast changes in the shaft speed, due to the very low gains.

The step on the desired propeller pitch is a difficult test case for almost all observers. Only the Immersion and Invariance (I&I) observer performs well in this scenario, with high VAF values. This could be attributed to the fact that the I&I observer uses the forward open water propeller diagram inside the estimation loop. This means a change in pitch has a direct effect on the variables inside the closed loop of the observer. Most other observers use the inverse open water propeller diagram in a feedforward manner to calculate the advance velocity.

The third test case scenario, where a low frequency sine wave is applied to the advance velocity disturbance, is observed very well by all observers. However, when the frequency of the advance velocity disturbance is increased, only some observers perform well. This is due to the fact that the transfer from the advance velocity disturbance to the shaft speed is much higher at low frequencies, and vice versa. This is shown in Section 2-7-3. Only the observers with more aggressive tunings, such as the Luenberger with high gains and the I&I observer with high gains perform very well in this scenario. Furthermore, the Measured Shaft Acceleration (MSA) observers perform well, since they have information regarding the acceleration of the shaft. This information is not available to any other observer.

The fifth and sixth test case are handled very well by all observers. This is due to the fact that the ramp and sine on the ship resistance disturbance do not contain any high frequency components. The ramp is very gradual, and the sine has a low frequency. Again, this is as was expected in Section 2-7-3.

The seventh test case contains the JONSWAP input on the advance velocity disturbance. This contains both low and high frequency components. This paints a similar picture to the high frequency disturbance on u_x, with more aggressive observers yielding better results.

When looking at the average values, it is clear that observers with higher gains outperform the observers with lower gains. The Luenberger observer with low gains shows the poorest performance, with an average VAF of 55%. The Luenberger observer with moderate gains performs slightly better, but both are outperformed by the Luenberger observer with high gains.

The Power Balance Estimator (PBE) does not yield a good result, with an average VAF of 88%. This is a direct result of the structure of the observer, where shaft acceleration is neglected. If shaft acceleration is high, this observer is very likely to produce a high estimation error. Both the MSA observer with and without measurements of shaft acceleration perform very well, even when high frequency disturbances are present. This is expected, since these observers use the acceleration of the shaft. This information is not available to any other observer.

The absolute best results, when no measurement noise is present, are found when looking at the I&I observer. This observer, when tuned with high gains, achieves an excellent average VAF of 99.95%. The standard deviation shows that observers with a high average VAF are also likely to have a low standard deviation. The coefficient of variation is much higher for observers with a low average VAF, and vice versa. This shows that observers that perform poorly on average, have a high variance. This is due to the fact that some test cases are inherently easier for all observers, while others are only performed well by some, leading to a high variance.

Table 4-2 shows the average VAF for each observer, as well as the data required by the observer. Furthermore, shown is the SNR that is required for the input signals of the observer, in order to reach a VAF value of at least 95% of the noiseless VAF. This was obtained as a result of test case eight, and its full results can be found in Appendix A-2.

Table 4-2: Average VAF, SNR [dB] required to reach a VAF of 95% of the noiseless VAF, and required data for each observer

	Avg. VAF [%]	SNR [dB]	Required data
Luenb. (low)	55.16	–	ω, M_m, $^P/_D$, I_R, ρ, D, IOWPD
Luenb. (moderate)	94.13	43.7	"
Luenb. (high)	97.68	67.6	"
SKF	93.38	40.4	ω, M_m, $^P/_D$, I_R, ρ, D, IOWPD
PBE	88.13	39.6	ω, M_m, $^P/_D$, ρ, D, IOWPD
MSA	97.68	39.6	ω, $\dot{\omega}$, M_m, $^P/_D$, I_R, ρ, D, IOWPD
MSA with derivative	97.53	47.8	ω, M_m, $^P/_D$, I_R, ρ, D, IOWPD
I&I (low)	90.87	39.2	ω, M_m, $^P/_D$, I_R, ρ, D, OWPD
I&I (moderate)	98.95	48.0	"
I&I (high)	99.95	59.8	"
RWKF	95.20	38.3	ω, M_m, $^P/_D$, I_L, I_R, ρ, D, i_{gb}, η_{trm}, η_r, a, b, c, OWPD and derivatives

The contents of this table are also color coded to improve clarity. The average VAF values are coded in the same manner as in Table 4-1. The SNR values required on the input signals of the observers in order to reach 95% of the noiseless VAF are coded in the following manner. If SNR $\leq 40\ dB$, the color is green, indicating good noise performance. If $40\ dB <$ SNR $\leq 50\ dB$, the color is orange, indicating moderate noise performance. Finally, if SNR $> 50\ dB$, the value is red, indicating poor noise performance.

When looking at the Luenberger observer, it is clear that higher gains lead to more accurate noiseless tracking of the advance velocity, but also to more sensitivity to measurement noise. When the Luenberger observer is tuned with low gains, the VAF when a high frequency advance velocity disturbance is applied is zero. Therefore, the SNR required to reach 95% of this value is not defined. For the I&I observer, higher gains also lead to more accurate noiseless performance, but also to less measurement noise robustness. Furthermore, the I&I observer clearly outperforms the Luenberger observer, with more accurate advance velocity tracking at comparable levels of noise robustness. The I&I observer is capable of providing the absolute best tracking at high gains, at the cost of measurement noise robustness.

Another interesting fact is that the Shaft Kalman Filter (SKF) only provides marginal increases in noise robustness when compared to the Luenberger observer. When looking at the PBE, it provides poor tracking of the advance velocity, but is very robust to measurement noise.

The MSA with measurements of shaft acceleration provides excellent tracking while also being very robust to measurement noise. In this regard, it seems to defy the trade off that is present in all other observers. However, the downside to this observer is that it requires an accurate measurement of the shaft acceleration. This data is not always available in ship propulsion systems. If the shaft acceleration is not available, but rather obtained by differentiating the shaft speed, the average VAF remains nearly identical when compared to the MSA observer where the shaft acceleration is available. However, the measurement noise robustness increases by more than 20%, from an SNR of $39.6\ dB$ to an SNR of $47.8\ dB$ required to reach a VAF of 95% of the VAF when no noise is present. This confirms the suspicion raised in Section 3-4-2; it is not practically possible to obtain the shaft acceleration by differentiating the shaft speed, as this significantly decreases the measurement noise robustness. If the shaft acceleration is only available through differentiation of a shaft speed signal, other observers provide a better combination of accurate noiseless tracking and measurement noise robustness.

Finally, the Random Walk Kalman Filter (RWKF) shows moderate noiseless tracking, with good noise rejection. This observer provides a very good trade off between advance velocity tracking and measurement noise rejection.

Table 4-2 clearly illustrates the trade off that is always present in the design of observers. If high gains are chosen, the noiseless tracking of the observed variable is very accurate, but the observer is very sensitive to measurement noise. On the other hand, if lower gains are chosen, the noiseless tracking is less accurate, but the observer is more robust to measurement noise. This is a consequence of the design of observers. Higher gains mean the measurements are trusted more than the model, and lower gains mean the model is deemed more trustworthy than the measurements. If the model, on which the observer is based, is perfect, the gains can be lower, leading to more favorable measurement noise rejection. If the model is not perfect, the gains must be higher, leading to more sensitivity to measurement noise. This confirms the fact that when applying observers to estimate unknown variables, the focus must be on the accuracy of the model, and the accuracy of the measurements. This leads to more accurate estimations. A possible solution to the trade off might be to tune the observers to specific disturbances. If little measurement noise is expected, but high frequency disturbances are present, the

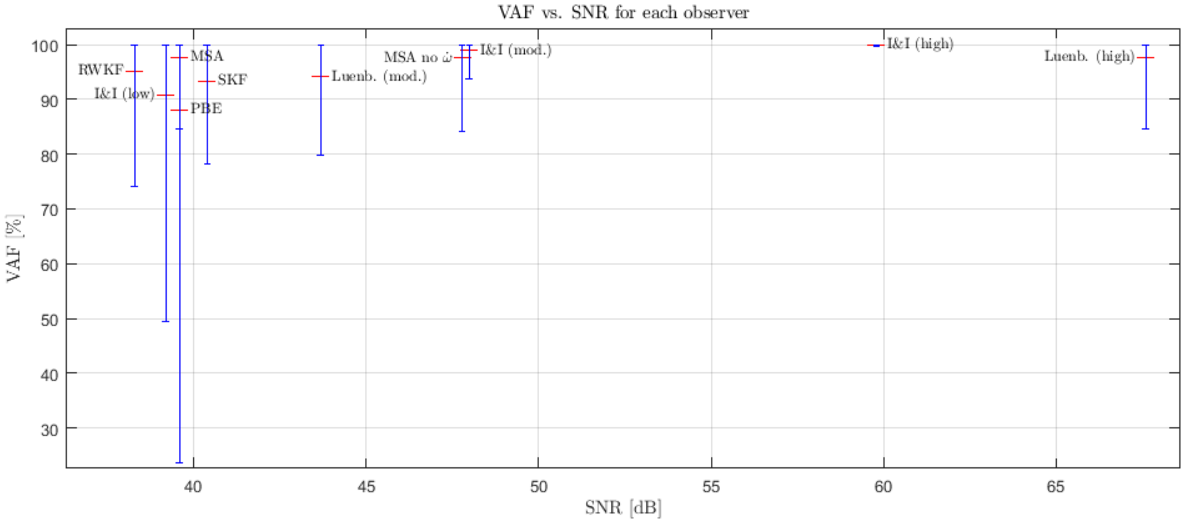

Figure 4-2: Average VAF vs. SNR [dB] required to reach a VAF of 95% for each observer

observer gains should be higher. Conversely, if the measurements are noisy, but the disturbances do not contain high frequencies, the gains can be lower.

Figure 4-2 shows the average noiseless VAF for each observer, against the SNR of the input signals required to reach at least 95% of the noiseless VAF. Furthermore, the minimum and maximum VAF values are shown, to give an indication of the spread of the results. This further confirms the aforementioned trade off between robustness against measurement noise and advance velocity tracking. An ideal observer would occupy the top left section of the figure, with high noiseless VAF values, and a low SNR required to reach a VAF of 95% of the noiseless VAF. The farther right an observer is placed, the less robust to measurement noise it is. The farther down an observer is placed, the less accurate its noiseless advance velocity tracking is.

The trade off between measurement noise robustness and noiseless tracking accuracy is driven home by Figure 4-3. This figure shows the noiseless VAF and the inverse of the SNR required to reach 95 % of the noiseless VAF, for different observer gains. This was performed for the I&I observer, using the high frequency advance velocity disturbance load case as described in Section 4-1. The inverse SNR was used instead of the SNR to better illustrate the trade off. It is clearly visible that, as the observer gain increases, the noiseless VAF increases. However, the inverse SNR required to reach 95 % of the noiseless VAF decreases. This means that a higher gain leads to a higher noiseless accuracy, but also to less measurement noise robustness. Therefore, the optimal observer gain is highly dependent on the required noiseless VAF, and the amount of noise present in the measurements.

The data leads to the following recommendations: if reliable shaft acceleration data is available, the MSA observer is the best option. This observer provides the best compromise between noiseless advance velocity tracking and input noise robustness. If this data is not available due to limitations in the sensor outfitting of the ship propulsion system, the selection becomes slightly more convoluted. If input noise robustness is most important, the best option is a RWKF or an I&I observer with low gains. If noiseless advance velocity tracking is most important, an I&I observer with high gains is the best option. It is also possible to continuously adjust the gains of the I&I observer, according to the disturbances. If high frequency advance velocity disturbances are expected, the gains should be higher. However, this will lead to a lower input noise robustness. If a compromise between noise robustness

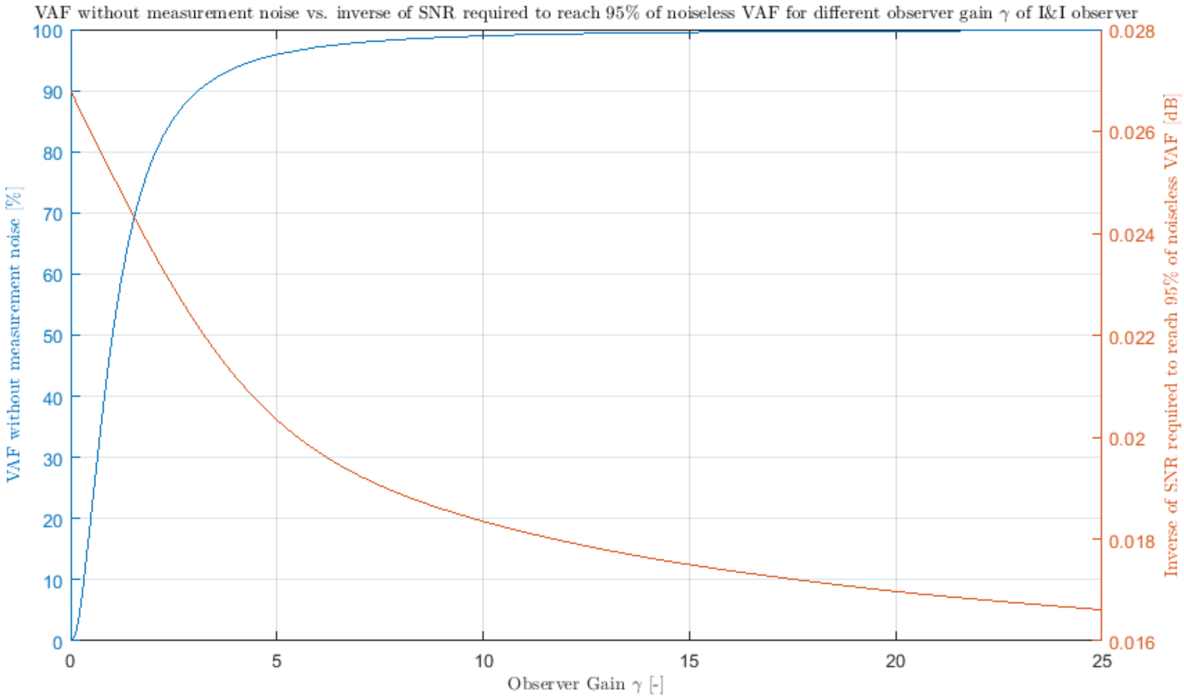

Figure 4-3: VAF without measurement noise and inverse of SNR required to reach 95 % of noiseless VAF as a function of observer gain γ for I&I observer

and noiseless advance velocity tracking is desired, the RWKF becomes the best option. This observer provides a good compromise between noiseless advance velocity tracking and noise robustness. However, the RWKF does require a lot of information regarding the propulsion system, most notably the engine parameters as described in Eq. (2-15).

This concludes the observer performance analysis. The next chapter will focus on the observer sensitivity analysis.

Chapter 5

Observer Sensitivity Analysis

A lot of a priori information about the propulsion system is necessary for an accurate estimation of the advance velocity. Some observers require more information than others, but all observers rely on certain known parameters for their estimation. If the provided information is inaccurate, this will lead to inaccuracies in the advance velocity estimation. This chapter will analyze the sensitivity of the observers to errors in the available information.

In order to test the sensitivity of the observers to errors, several different inaccuracies in the available data will be introduced. Keep in mind that these inaccuracies are only introduced to the observers, not to the ship propulsion model. In order to keep the analysis clear, only one load case will be used to analyze the different combinations of errors and observers. The load case that was selected for this is the high frequency advance velocity disturbance introduced in Section 4-1-3. This load case was chosen because it is a difficult scenario for the observers, and it provides the most clear distinction between good and bad performance. The next section will describe the different test cases that will be implemented.

5-1 Test Cases

Six individual test cases are used to investigate the sensitivity of the observers to errors in the available data. These include:

1. Multiplicative errors on shaft inertia
2. Multiplicative errors on OWPD
3. Errors in propeller expanded area ratio

Next, each individual test case will be highlighted.

5-1-1 Multiplicative error on shaft inertia

These test cases cover an error in shaft inertia used by the observers. Since all observers use the shaft inertia, an error in the shaft inertia could cause a significant error in the advance velocity estimation. Two errors of ±10% are used to model a significant error in the shaft inertia.

5-1-2 Multiplicative errors on OWPD

The next two test cases involve multiplicative errors in the Open Water Propeller Diagrams (OWPD). The correct diagrams for K_Q and K_T are increased and decreased by ±10%. Next, the necessary derivative and inverse diagrams are calculated. These diagrams are then used by the observers.

5-1-3 Errors in propeller expanded area ratio

The final two errors are introduced in the form of inaccurate propeller expanded area ratios. The Expanded Area Ratio (EAR) is a parameter describing the geometry of the propeller, and is used to calculate the OWPD. The correct value for the EAR for the used propeller is $EAR = 0.9$. Two inaccurate OWPD are calculated with ratios of $EAR = 0.6$ and $EAR = 1$. Next, the necessary derivative and inverse diagrams are calculated. These diagrams are then used by the observers.

5-2 Performance Comparison

The six different test cases were combined with the eleven different combinations of observers and tunings. The time domain results for the different observers with inaccuracies can be found in Appendix A-3. Table 5-1 shows the changes in Variance Accounted For (VAF) values as a result of the different inaccuracies. The column with "VAF" shows the VAF that is reached when no inaccuracy is present. The next six columns describe the change in VAF as a result of the inaccuracies. The final two columns show the Root Mean Square (RMS) and the Standard Deviation (SD) of the change in VAF.

Table 5-1: Change in VAF as a result of different inaccuracies

	VAF	$I \downarrow$	$I \uparrow$	OWPD ↓	OWPD ↑	EAR ↓	EAR ↑	RMS	SD
Luenb. (low)	0	0	0	0	0	0	0	0	0
Luenb. (mod.)	82.89	0	0	+1.10	−0.40	−3.01	+0.46	1.33	1.26
Luenb. (high)	99.96	0	0	−0.78	−1.72	−1.64	−0.05	1.02	0.82
SKF	78.33	0	+0.01	−2.22	+1.41	−5.09	+1.05	2.38	2.45
PBE	96.29	0	0	+1.81	−6.19	+2.60	+1.42	2.90	3.12
MSA	99.96	+0.01	−0.09	−0.78	−1.72	−1.63	−0.05	1.02	0.80
MSA without $\dot{\omega}$	99.43	+0.01	−0.08	−0.45	−2.16	−1.28	−0.15	1.04	0.86
I&I (low)	49.54	+4.52	−4.05	−3.82	+2.17	−4.58	+1.19	3.62	3.88
I&I (mod.)	93.73	+0.85	−0.97	−0.87	−0.64	+1.08	+0.09	0.82	0.76
I&I (high)	99.73	−0.04	−0.03	−0.74	+1.13	−0.73	−0.18	0.63	0.46
RWKF	95.66	0	0	+2.61	−3.59	+1.86	+1.49	2.06	2.25

Again, the contents of this table are color coded to improve readability. The average VAF values are coded in the same manner as in Table 4-1. The change in VAF values are coded in the following manner. If the change in VAF is VAF $> \pm 3\%$, the color is red, indicating poor performance. If the change in VAF is $\pm 3\% \geq$ VAF $> \pm 1.5\%$, the color is orange, indicating moderate performance. If the change in VAF is VAF $\leq \pm 1.5\%$, the color is green, indicating good performance. Both negative and positive changes are considered undesired, since both positive and negative changes indicate high sensitivity to data inaccuracies. Furthermore, if the VAF value increases, the measurement noise robustness generally decreases, due to the aforementioned trade off.

Table 5-1 shows that the observers are more robust to some inaccuracies than to others. For instance, almost all observers are very robust to errors in the shaft inertia. Only the Immersion and Invariance (I&I) observer with low gains shows large changes when faced with an incorrect shaft inertia. Errors in the OWPD lead to much larger changes in the VAF. Especially the Random Walk Kalman Filter (RWKF), Power Balance Estimator (PBE) and I&I observer with low gains are not very robust to multiplicative errors in the OWPD. The RWKF also relies on derivatives of the OWPD, so this could lead to larger deviations. If a grossly incorrect EAR is chosen, almost all observers struggle to maintain accuracy. This can be seen in the scenario where an EAR of 0.6 is chosen. Only the I&I observer with high gains reports a change of less than 1 %. If a minor error in the EAR is present, almost all observers perform well. This can be seen in the scenario where the EAR was chosen to be 1.

When looking at the individual observers, it is clear that the observer that is most robust to data inaccuracies is the I&I observer with high gains. Moderate gains lead to slightly higher sensitivity, while low gains result in significant sensitivity to data inaccuracies. The same can be said for the Luenberger observer, where higher gains result in less sensitivity to data inaccuracies. This leads to the conclusion that higher gains lead to more robustness to data errors. This is in accordance with the theory explained in Section 4-3; when the gains are higher, the measurements are trusted more than the model and vice versa. When an error is introduced in one or more of the model parameters, the model becomes less accurate. In that case, it makes sense to trust the measurements more than the model. This leads to more robustness to model inaccuracies when higher observer gains are used. The Luenberger observer has a change in VAF of zero for all scenarios, but this is due to the fact that the VAF without introduced errors is also zero. The Shaft Kalman Filter (SKF), PBE and RWKF all perform moderately well, with RMS changes in VAF of 2.38 %, 2.9 % and 2.06 %. Both the Measured Shaft Acceleration (MSA) observers with and without measurements of $\dot{\omega}$ are very robust to data errors, with RMS changes in VAF of 1.02 % and 1.04 %.

The conclusions that can be drawn from this data are clear. The most significant model inaccuracies in terms of changes in VAF, are multiplicative errors in the OWPD and high errors in the EAR. Errors in the shaft inertia are much less significant. Furthermore, the observers that are most robust to data errors are the Luenberger observer with high gains, the MSA observer and the I&I observer with high gains.

Chapter 6

Conclusion & Recommendations

This final chapter will draw conclusions based on the performed research in Section 6-1. Furthermore, suggestions for future research are made in Section 6-2.

6-1 Conclusion

Now that the research is complete, it is possible to draw conclusions based on the findings in this thesis. The research question as posed in the introduction was:

What is the most effective observer structure for estimating the advance velocity of a marine propulsion system with a controllable pitch propeller?

The research has revealed that this is not a straightforward question to answer. There is no definitive best option regarding the most effective observer structure, since some observers are more suited to a specific task than others. As seen in Table 4-2 and Figure 4-3, there exists an inherent trade off in the design of observers; if the observer is more robust to noise in the available measurements, the noiseless tracking is less accurate. On the other hand, if the noiseless advance velocity tracking of the observer is very accurate, the observer is less robust to measurement noise. This is due to the fact that when the gains of the observer are higher, the measurements are trusted more than the model and vice versa. Lower observer gains lead to less accurate noiseless estimates, but more robustness to measurement noise, since the measurements are trusted less. This can be seen in Table 4-2, where the Luenberger and Immersion and Invariance (I&I) observers with higher gains have better tracking accuracy when no noise is present, but less noise robustness when compared to the lower gain variants. This means the observer should be tuned to the exact disturbances and noise levels that are expected. If less measurement noise is present, the gains can be higher and vice versa.

Chapter 5 revealed that observers with higher gains are more robust to errors in the model used by the observer. This is in line with the idea that higher gains mean the measurements are trusted more than the observer. If the observer model contains errors or inaccuracies, the measurements should be trusted more, and therefore the gains should be higher. Furthermore, the errors that lead to the most significant estimation errors were multiplicative errors in the Open Water Propeller Diagrams (OWPD), and high errors in the Expanded Area Ratio (EAR). Errors in shaft inertia were much less significant. Therefore, the more accurate the OWPD, the more accurate the observer.

If more information regarding the system is available, the trade off between noise robustness and noiseless accuracy is less significant. This can also be seen in Table 4-2, where the Measured Shaft Acceleration (MSA) observer performed well in the time domain with and without noise. This is due to the fact that this observer had access to the shaft acceleration, which other observers did not. Unfortunately, this acceleration data is not always available in marine propulsion systems. If the shaft acceleration is obtained through differentiating the shaft speed, the observer does not perform well when measurement noise is present. This can be attributed to the fact that when a noisy signal is differentiated, the noise is amplified.

Taking all this into account, it is possible to answer the research question.

If accurate shaft acceleration data is available, the MSA observer is the most effective advance velocity observer. If this data is unavailable due to limitations in the sensor outfitting of the propulsion system, a choice must be made. If measurement noise robustness is paramount, the Random Walk Kalman Filter (RWKF) or an I&I observer with low gains is most effective. If absolute accuracy is most important, and the measured variables are virtually free of noise, the I&I observer with high gains is most effective. Tuning the I&I observer to the expected noise is a promising strategy. If a compromise between noise robustness and noiseless accuracy is required, the RWKF is the best option. However, this observer requires a lot of in depth information regarding the propulsion system.

6-2 Recommendations

The following recommendations for future research are made:

- Test observers in cavitation tunnel and full scale propulsion system

  In this thesis, the observers have only been tested on a mathematical model. It would be very interesting to see how the observers perform when applied to a physical system. Firstly, the observers could be tested in a cavitation tunnel, where many parameters of the propulsion system can be controlled and monitored. If the cavitation tunnel tests are successful, the observers could be applied to a full scale propulsion system aboard an actual ship.

- Add multivariable control using estimated advance velocity

  Acquiring an estimate of the advance velocity in a ship propulsion system is not a goal in itself. The purpose of an estimated advance velocity is that it can be used for advanced control techniques, as illustrated in Chapter 1. Therefore, applying the synthesized observers in combination with advanced control algorithms is a interesting goal, and one that should be examined further.

- Extend model and observers to operate outside first quadrant

The synthesized mathematical model and observers are only designed for and tested in the first quadrant, i.e. when both the advance velocity and the shaft speed are positive. For dynamic positioning and maneuvering purposes, it would be interesting to extend both the model and the observers to be able to operate outside the first quadrant.

- Changing observer gains according to noise and disturbances

  As seen in Section 4-3, it might be beneficial to tune the observers to the specific disturbances and noise levels that are expected. Furthermore, the observers could be extended to automatically alter their tuning to the encountered disturbances. This is an interesting concept to investigate in future research.

- Extend observers to electric motors

  The model and observers in this thesis were only focused on diesel engines, but could also be extended to ship propulsion plants with electric motors. The model itself could easily be changed to use electric motors by changing Eq. (2-13) to a variant describing electric motors. Most observers do not need to be changed to accommodate propulsion systems with electric motors, although the RWKF contains specific linearizations based on the engine torque. These must be recalculated based on the electric motor torque.

Appendix A

Simulation Results

This appendix contains the time domain results from the test case simulations for each observer in Section A-1. Section A-2 shows the results for the noise simulations for all observers. The time domain results for the sensitivity analysis can be found in Section A-3.

A-1 Time Domain Results

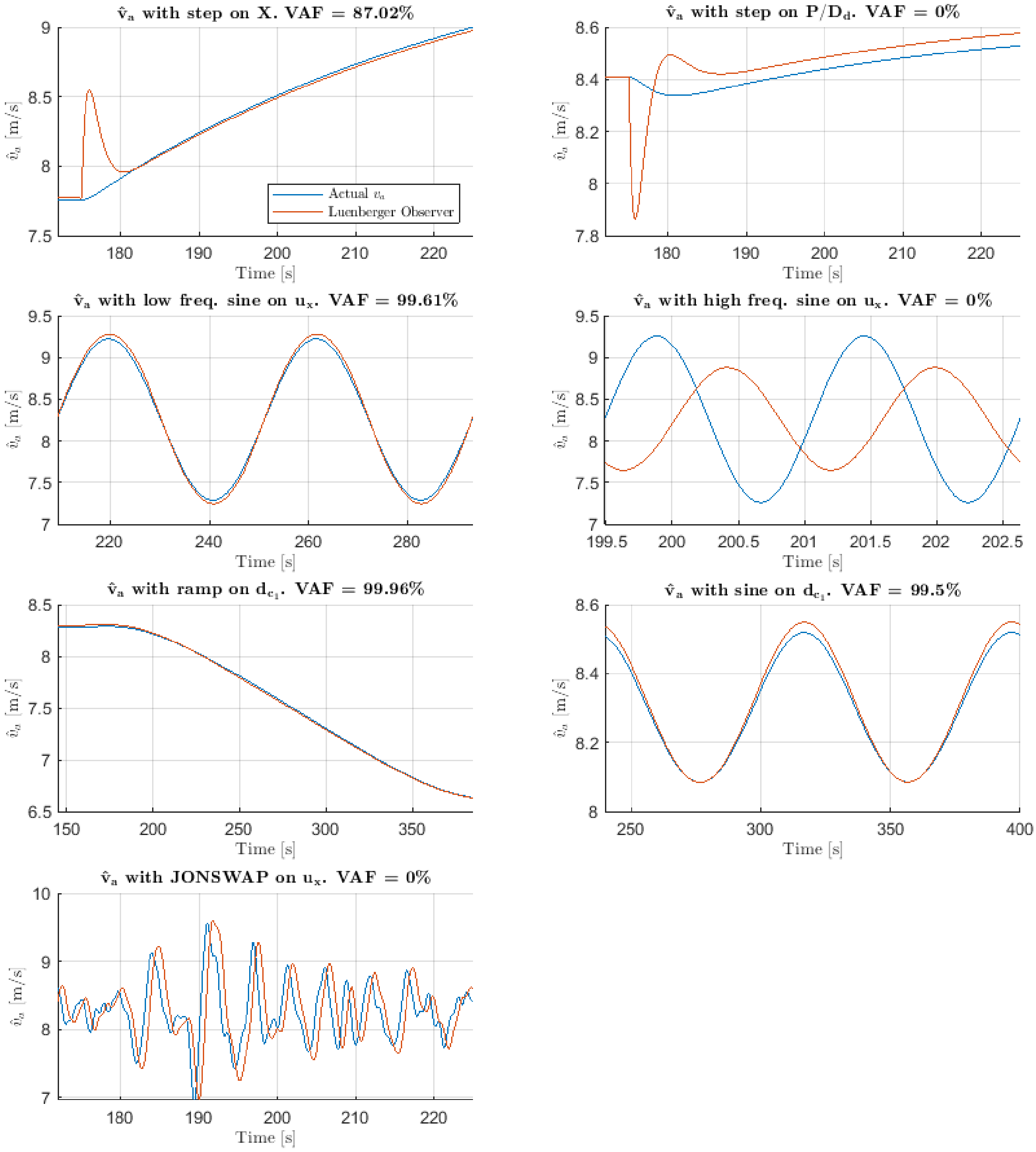

Figure A-1: Advance Velocity estimated by Luenberger Observer with low gains

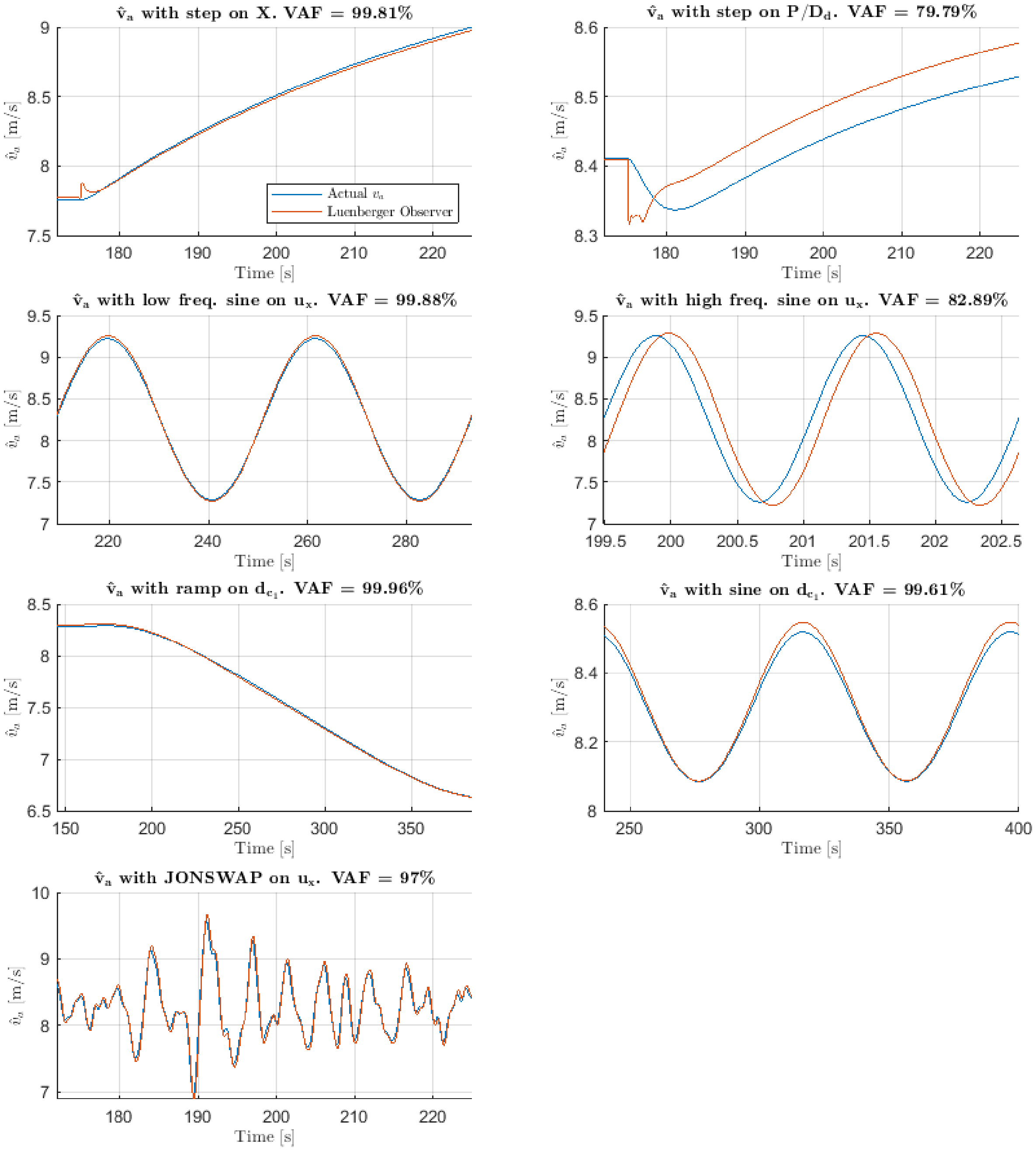

Figure A-2: Advance Velocity estimated by Luenberger Observer with moderate gains

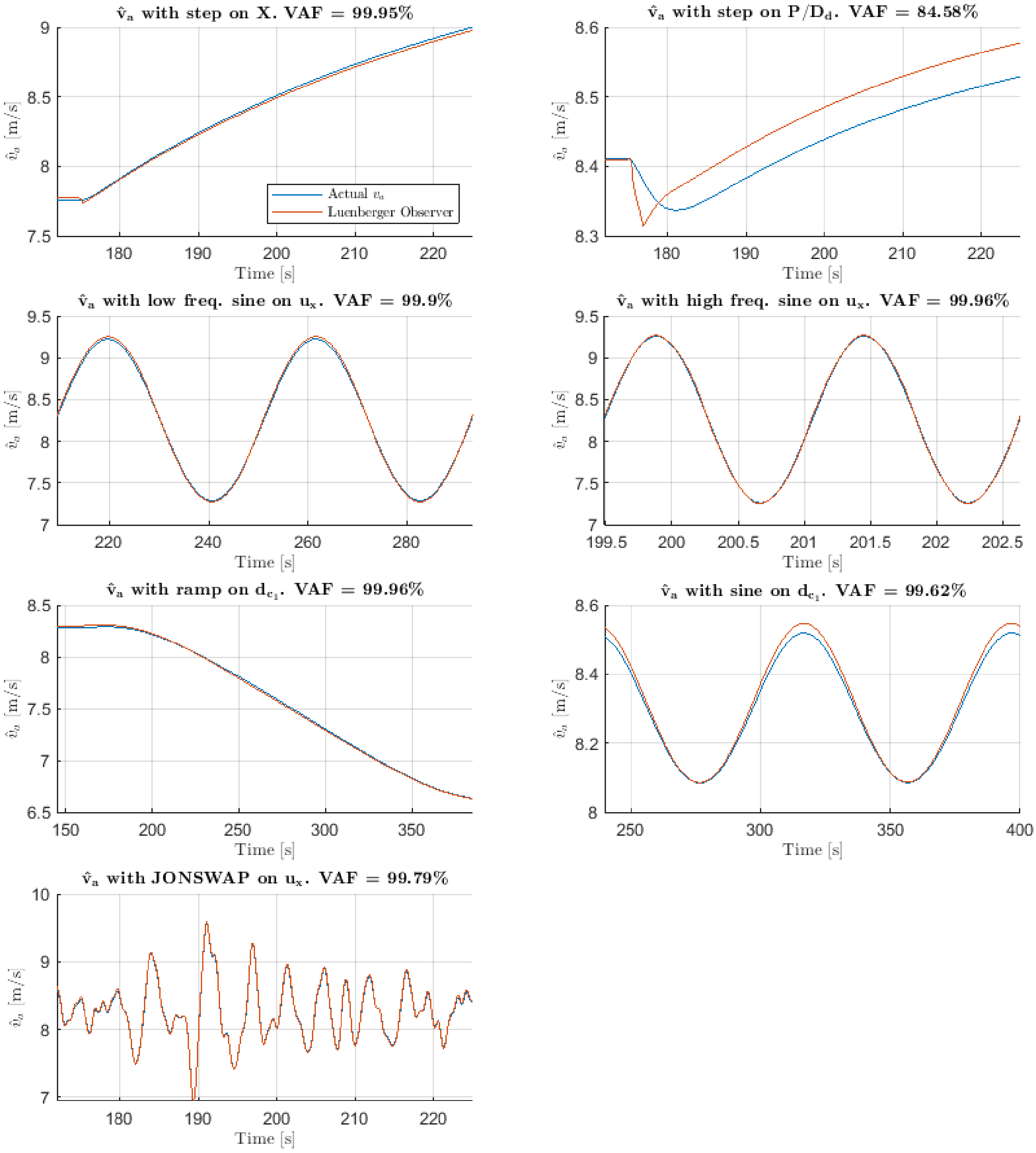

Figure A-3: Advance Velocity estimated by Luenberger Observer with high gains

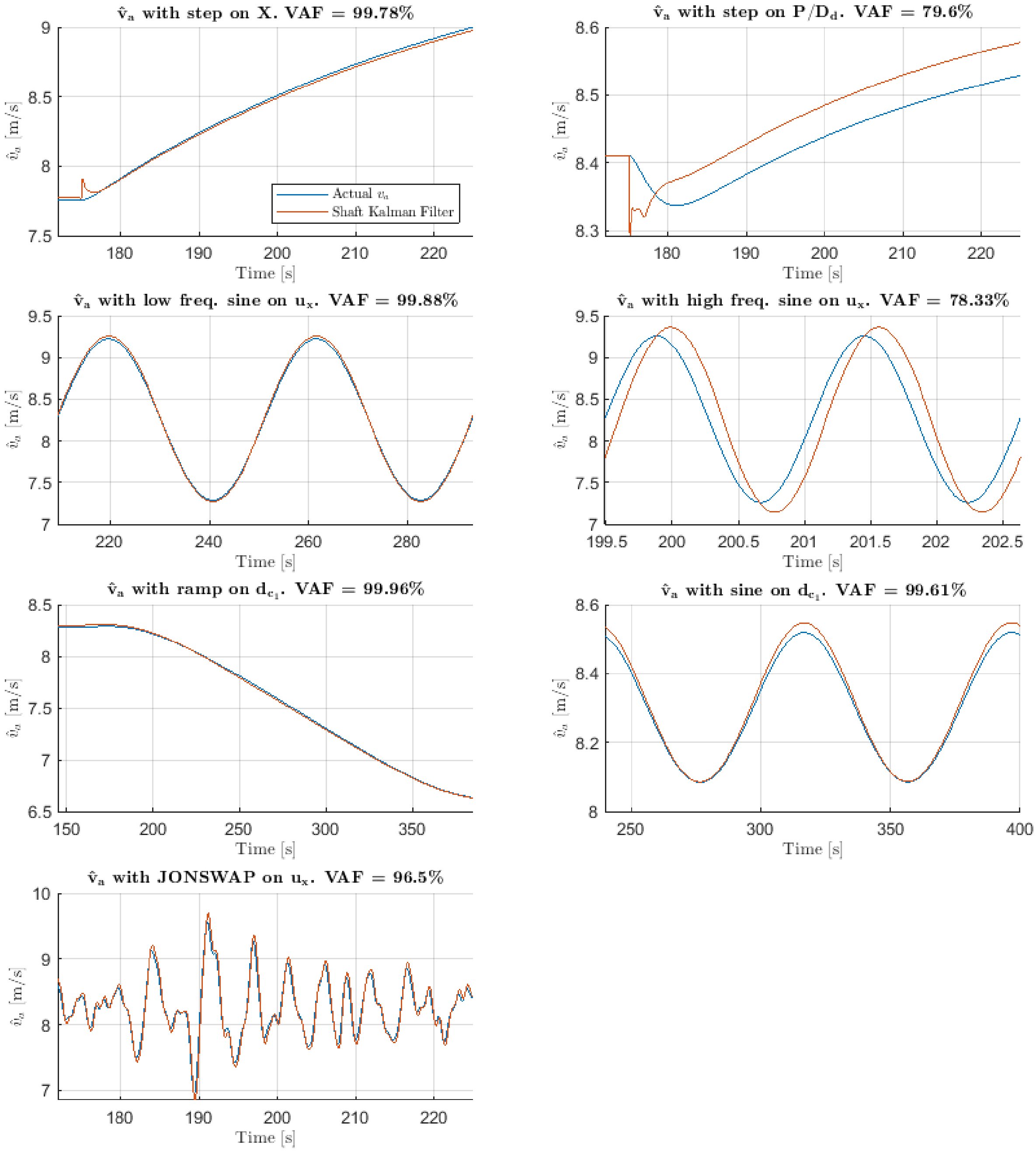

Figure A-4: Advance Velocity estimated by Shaft Kalman Filter

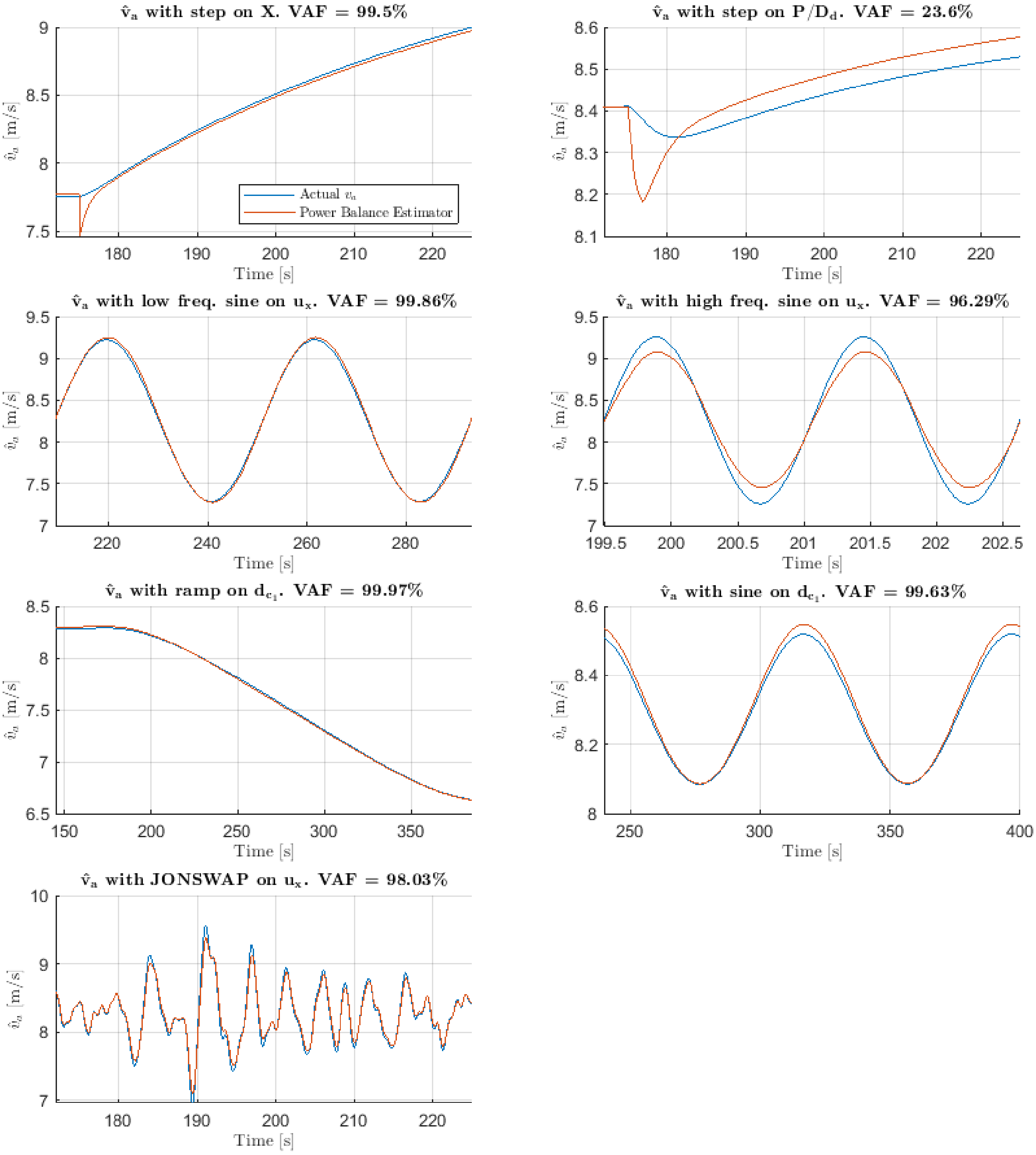

Figure A-5: Advance Velocity estimated by Power Balance Estimator

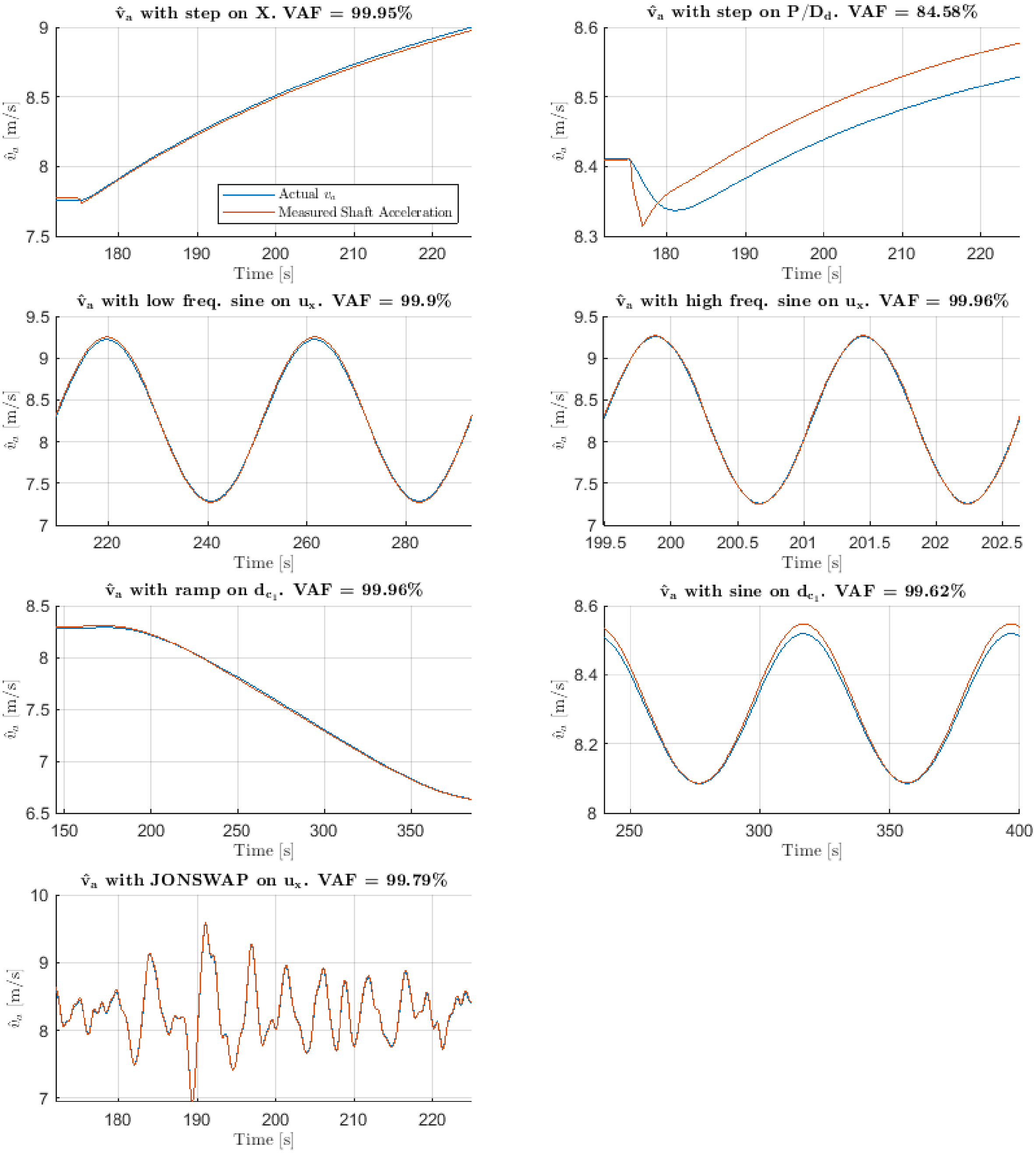

Figure A-6: Advance Velocity estimated by Measured Shaft Acceleration Observer

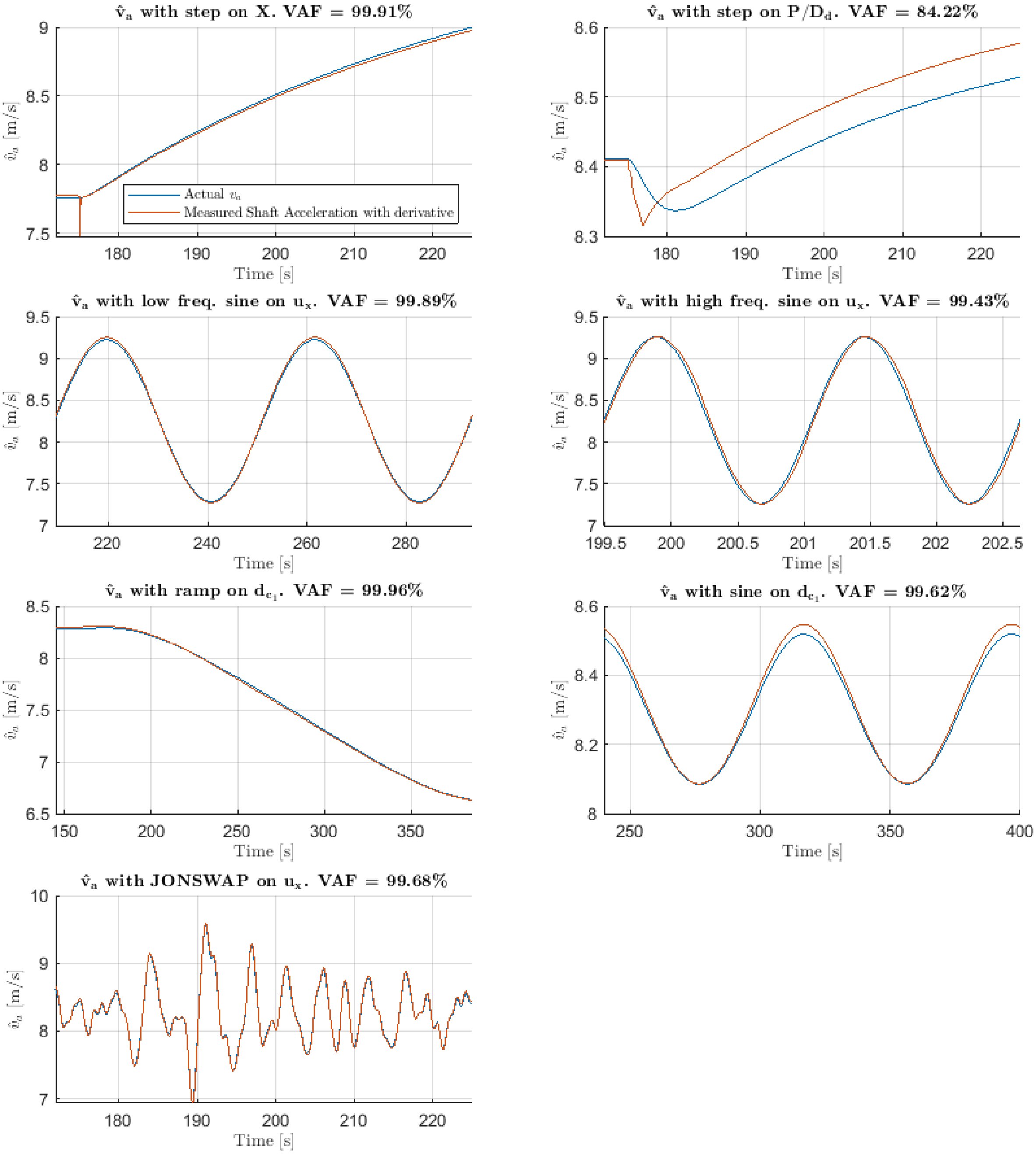

Figure A-7: Advance Velocity estimated by Measured Shaft Acceleration Observer without shaft acceleration measurement

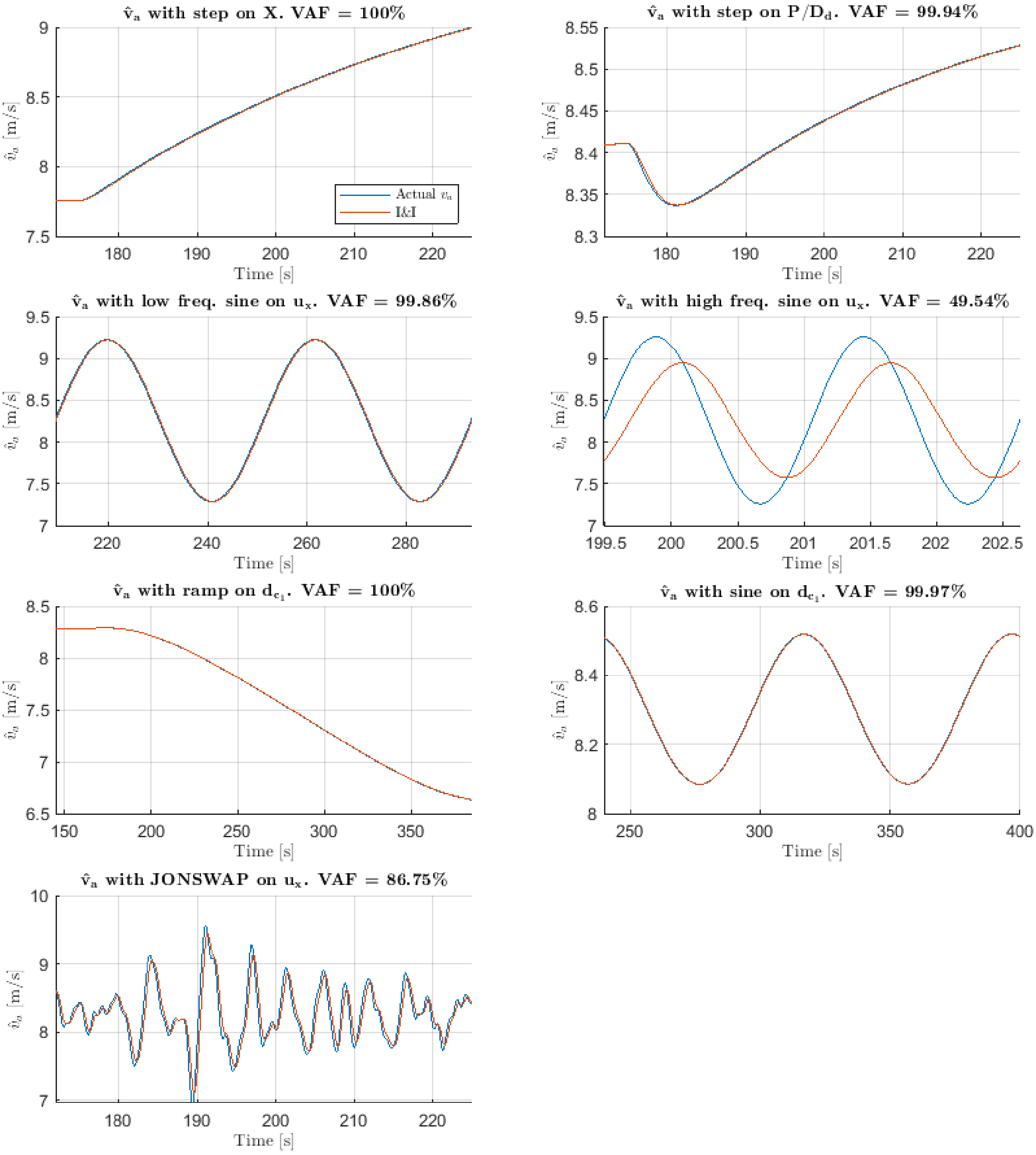

$\hat{\mathbf{v}}_\mathbf{a}$ **with step on X. VAF = 100%**

$\hat{\mathbf{v}}_\mathbf{a}$ **with step on P/D$_\mathbf{d}$. VAF = 99.94%**

$\hat{\mathbf{v}}_\mathbf{a}$ **with low freq. sine on u$_\mathbf{x}$. VAF = 99.86%**

$\hat{\mathbf{v}}_\mathbf{a}$ **with high freq. sine on u$_\mathbf{x}$. VAF = 49.54%**

$\hat{\mathbf{v}}_\mathbf{a}$ **with ramp on d$_{\mathbf{c}_1}$. VAF = 100%**

$\hat{\mathbf{v}}_\mathbf{a}$ **with sine on d$_{\mathbf{c}_1}$. VAF = 99.97%**

$\hat{\mathbf{v}}_\mathbf{a}$ **with JONSWAP on u$_\mathbf{x}$. VAF = 86.75%**

Figure A-8: Advance Velocity estimated by Immersion & Invariance Observer with $\gamma = 1$

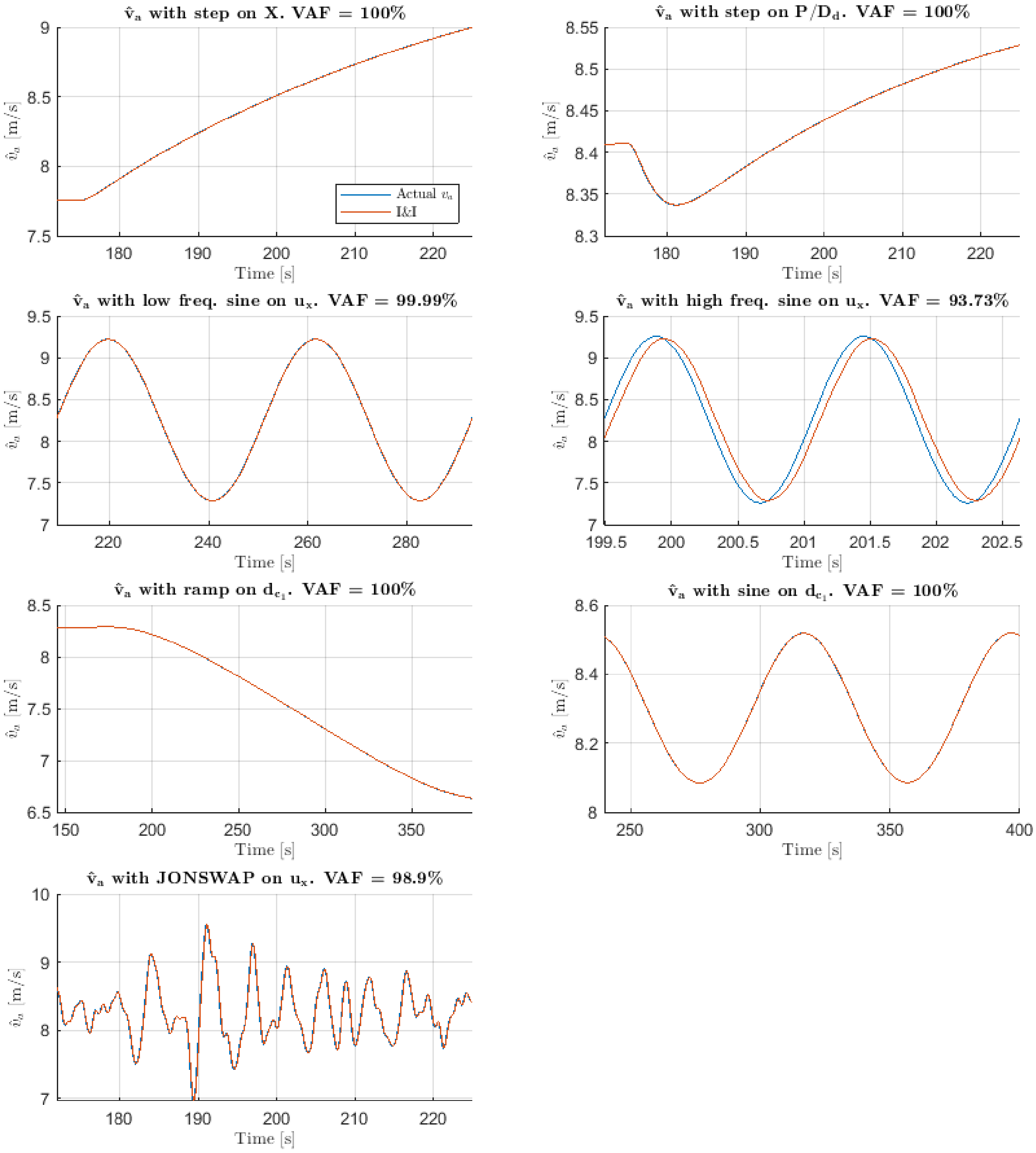

Figure A-9: Advance Velocity estimated by Immersion & Invariance Observer with $\gamma = 4$

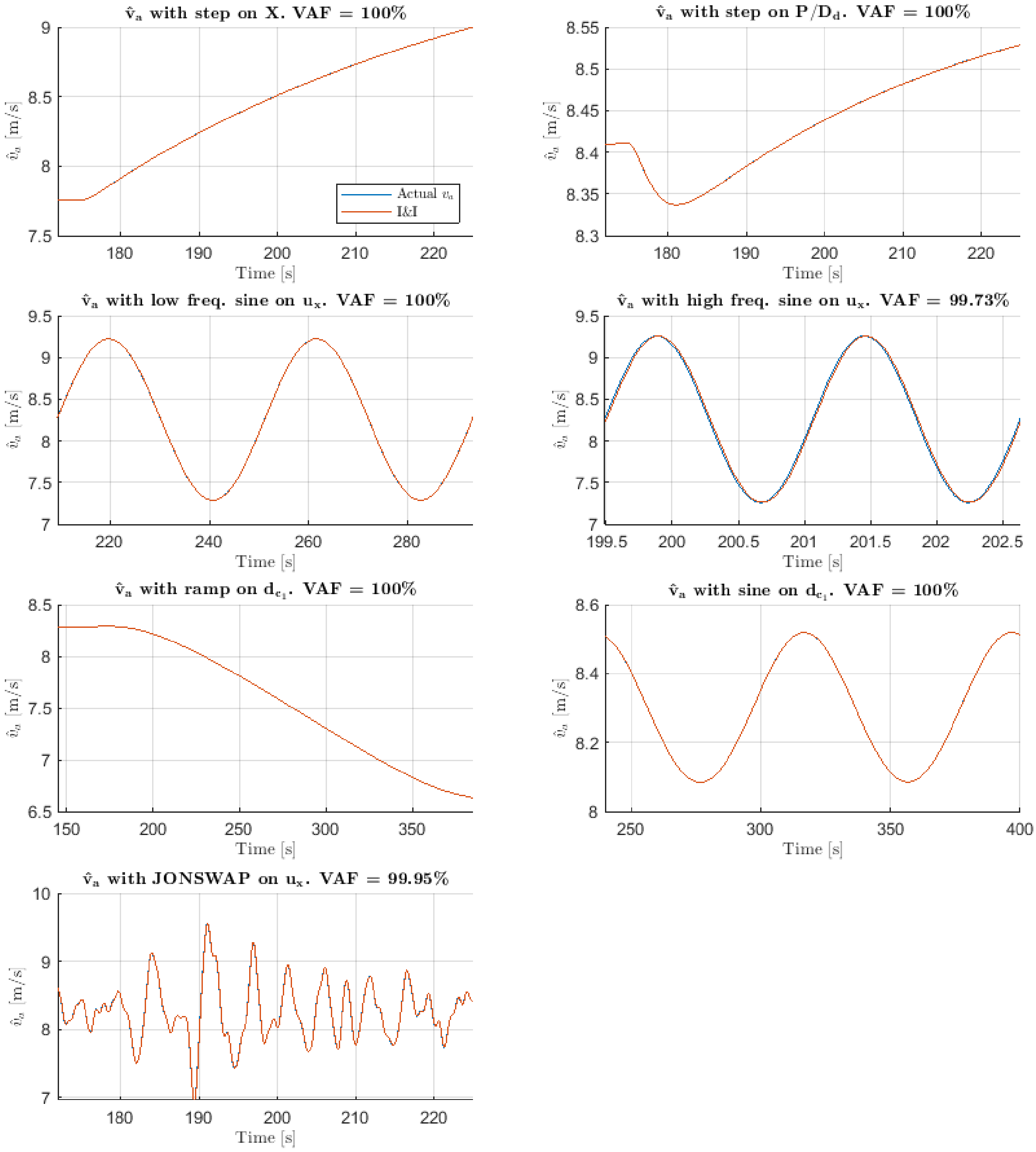

Figure A-10: Advance Velocity estimated by Immersion & Invariance Observer with $\gamma = 20$

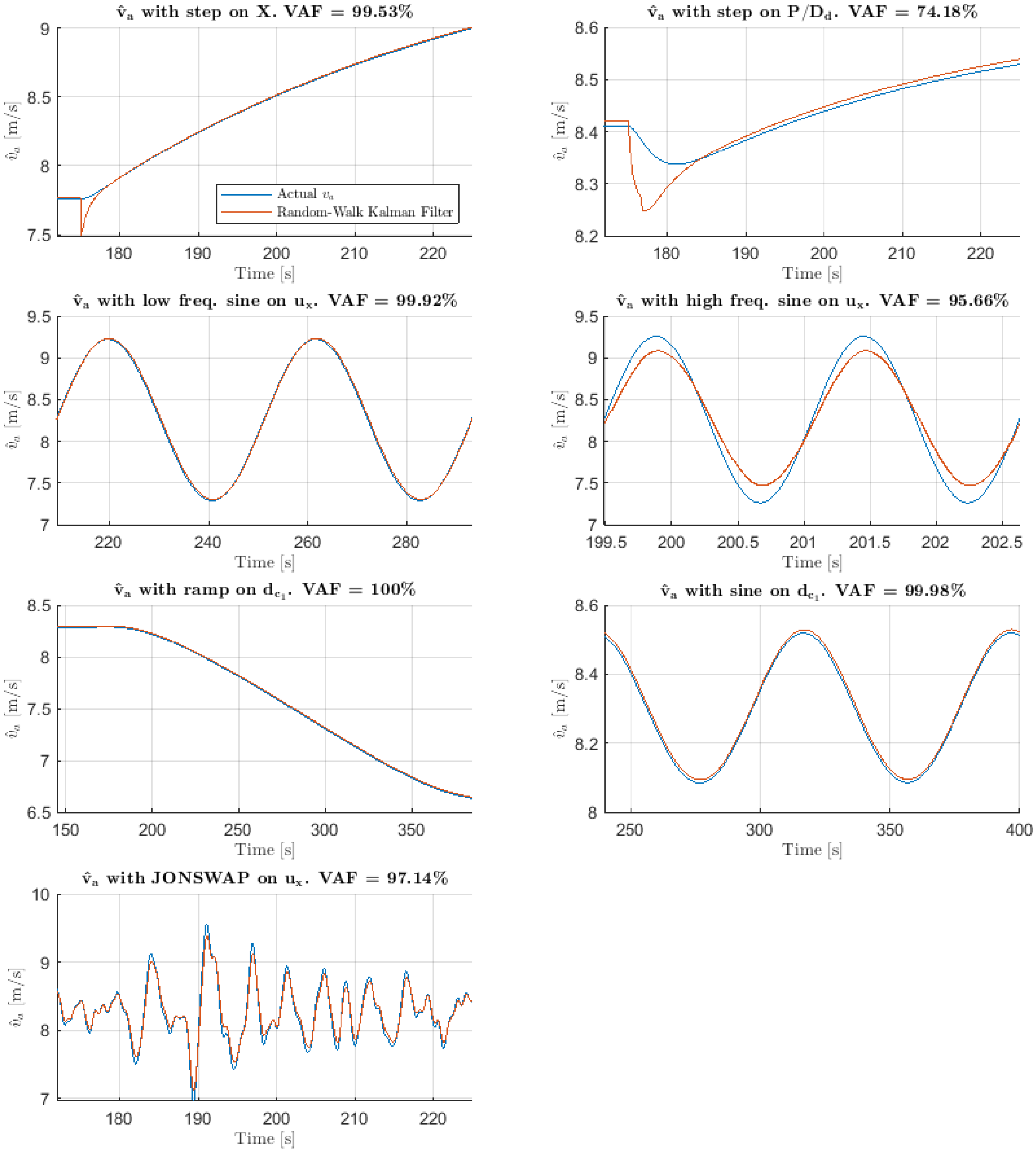

Figure A-11: Advance Velocity estimated by Random Walk Kalman Filter

A-2 Noise Results

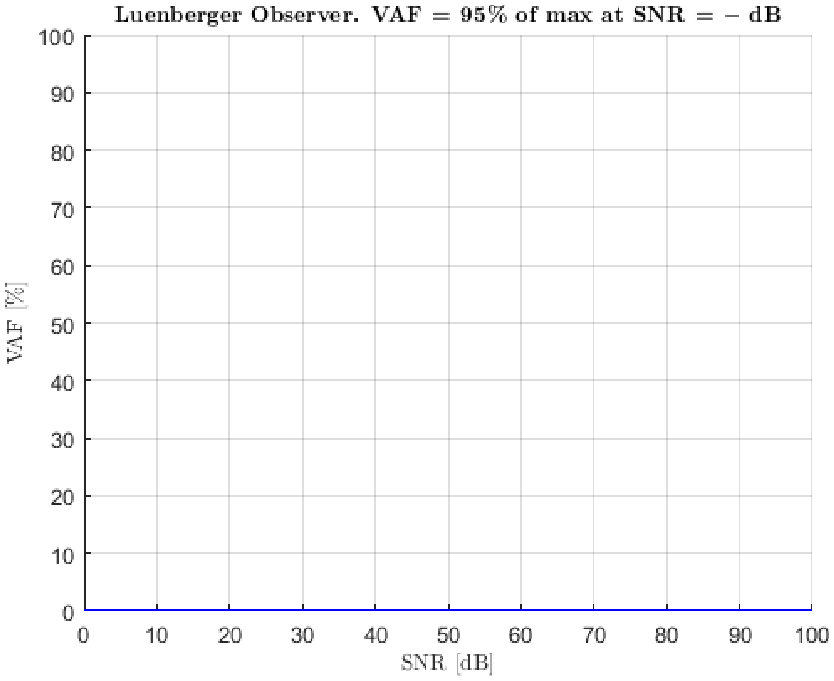

Figure A-12: VAF against SNR for Luenberger Observer with low gains

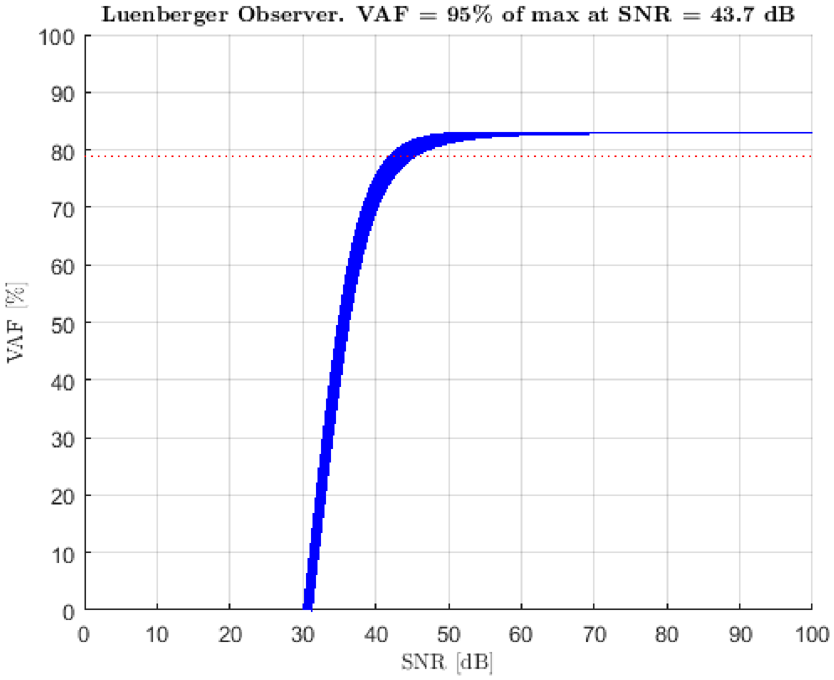

Figure A-13: VAF against SNR for Luenberger Observer with moderate gains

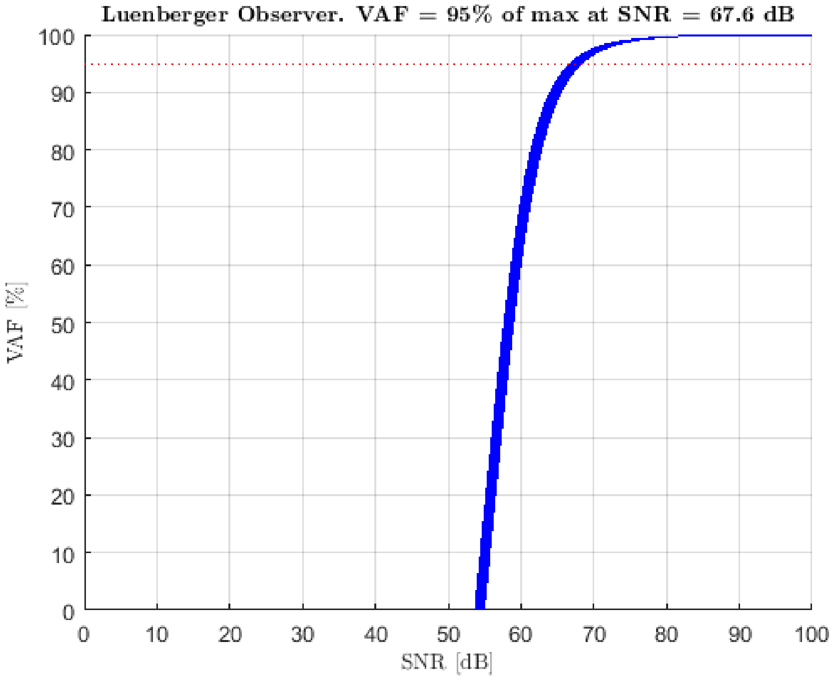

Figure A-14: VAF against SNR for Luenberger Observer with high gains

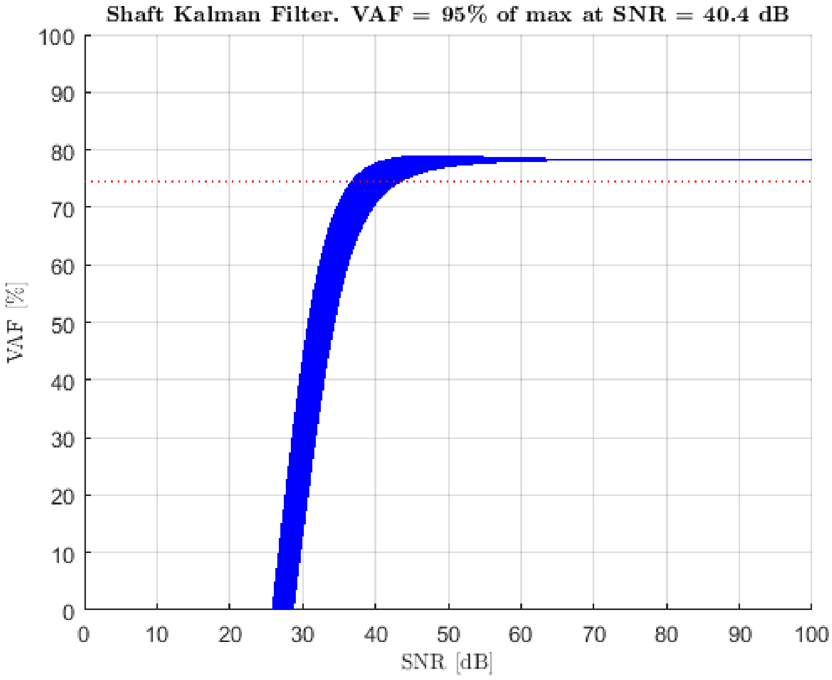

Figure A-15: VAF against SNR for SKF

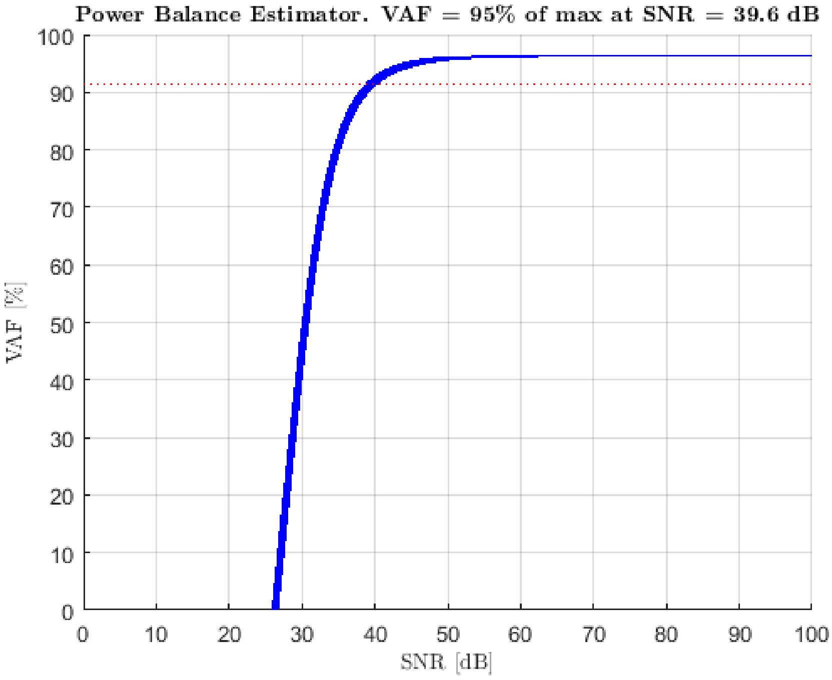

Figure A-16: VAF against SNR for Power Balance Estimator

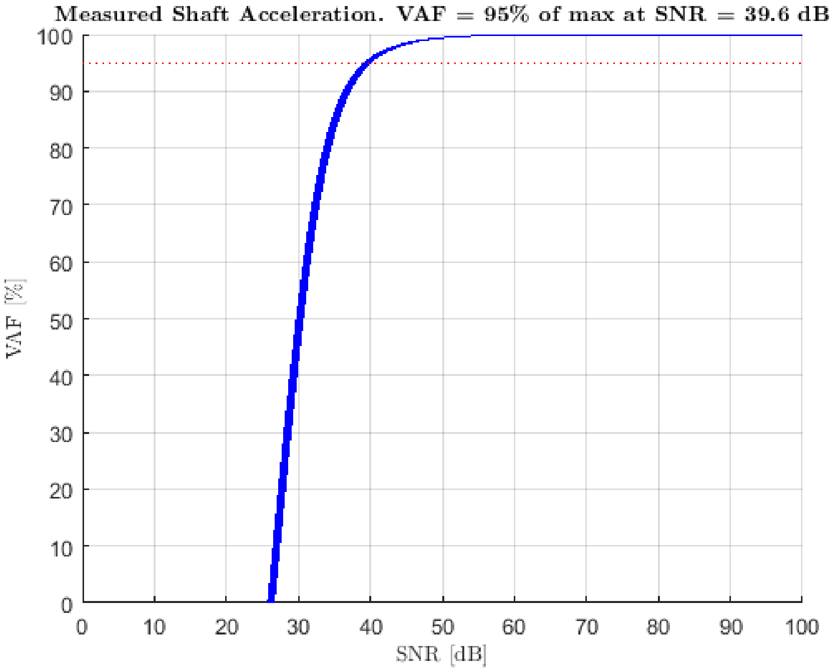

Figure A-17: VAF against SNR for Measured Shaft Acceleration Observer

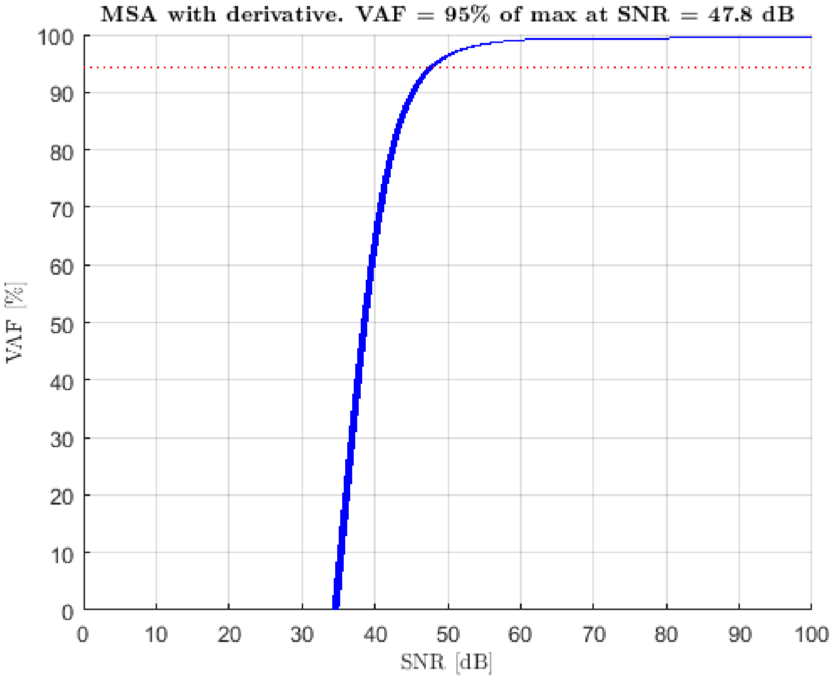

Figure A-18: VAF against SNR for Measured Shaft Acceleration Observer without acceleration measurement

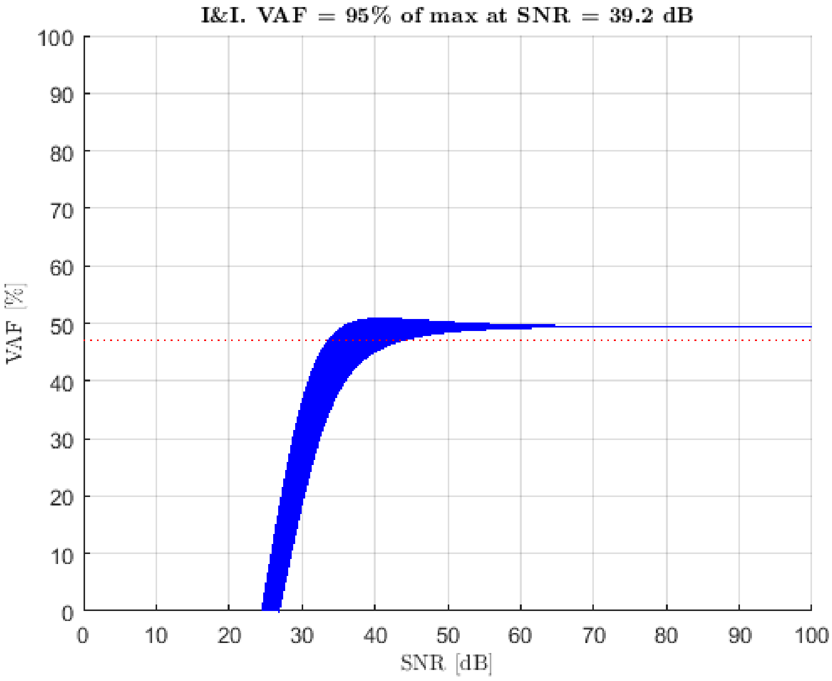

Figure A-19: VAF against SNR for Immersion & Invariance Observer with $\gamma = 1$

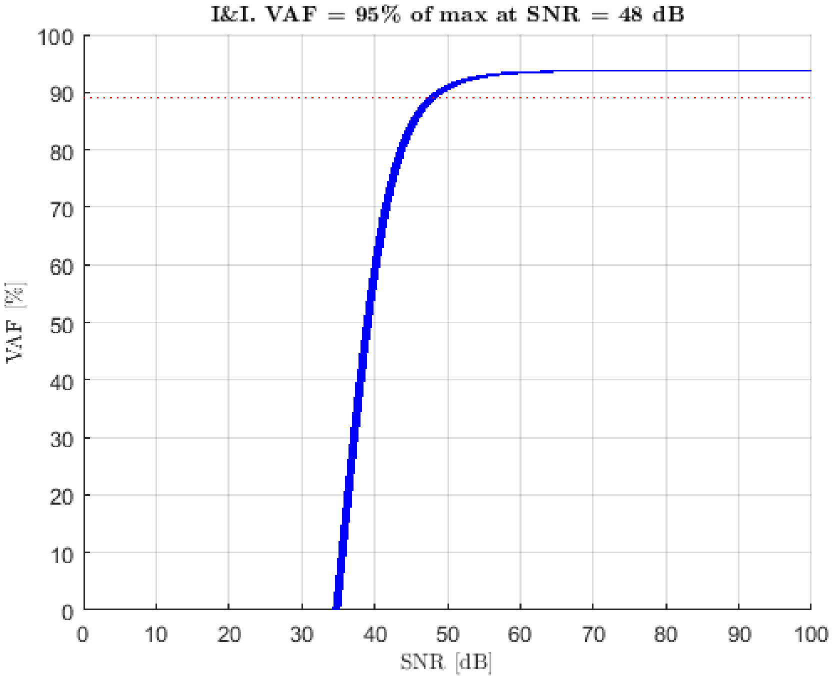

Figure A-20: VAF against SNR for Immersion & Invariance Observer with $\gamma = 4$

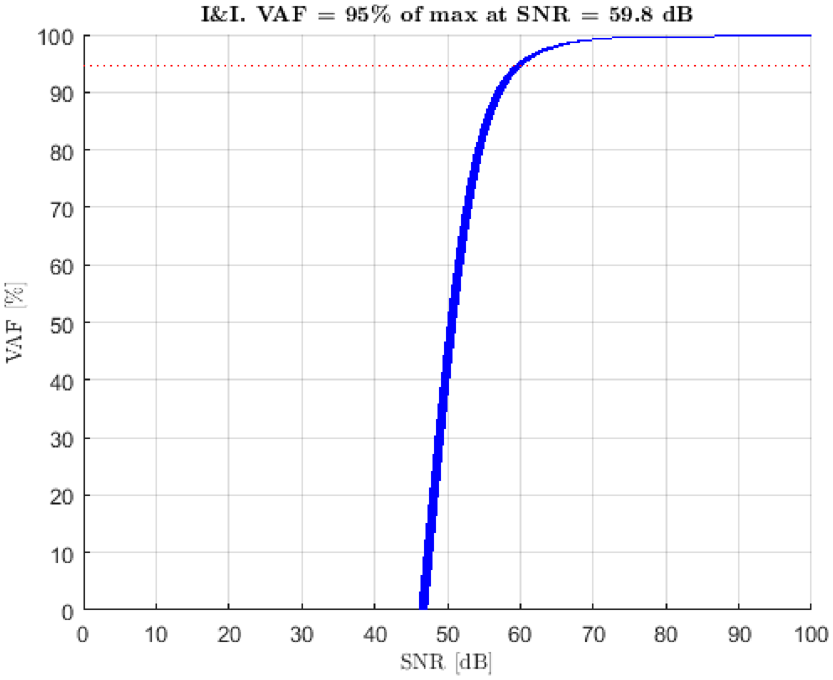

Figure A-21: VAF against SNR for Immersion & Invariance Observer with $\gamma = 20$

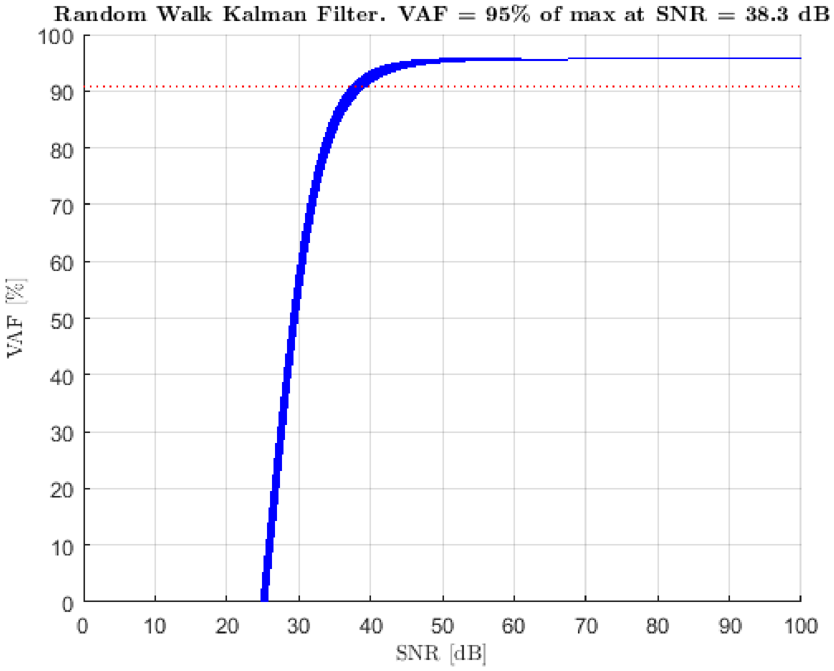

Figure A-22: VAF against SNR for Random Walk Kalman Filter

A-3 Time Domain Results Sensitivity Analysis

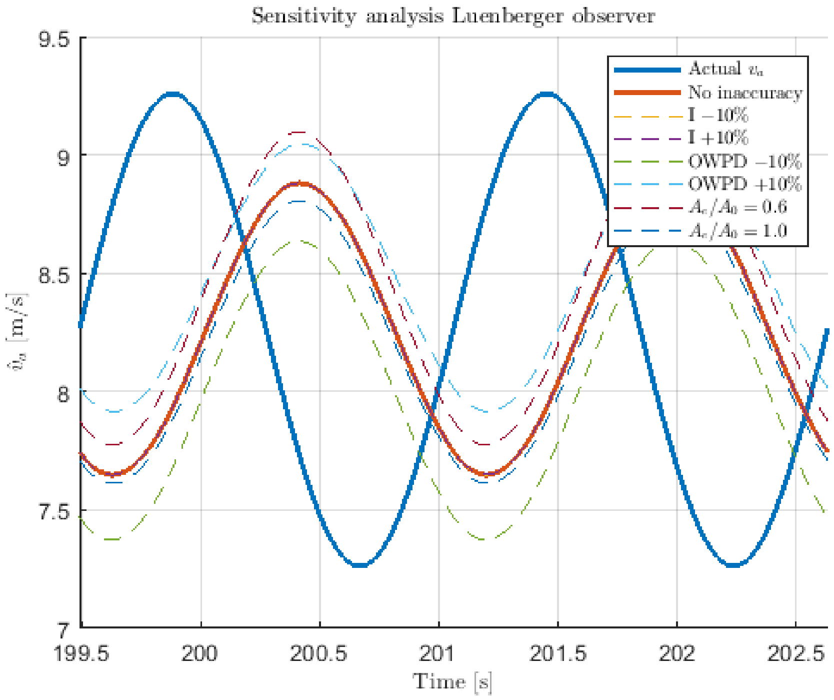

Figure A-23: Advance Velocity estimated by Luenberger Observer with low gains with different inaccuracies

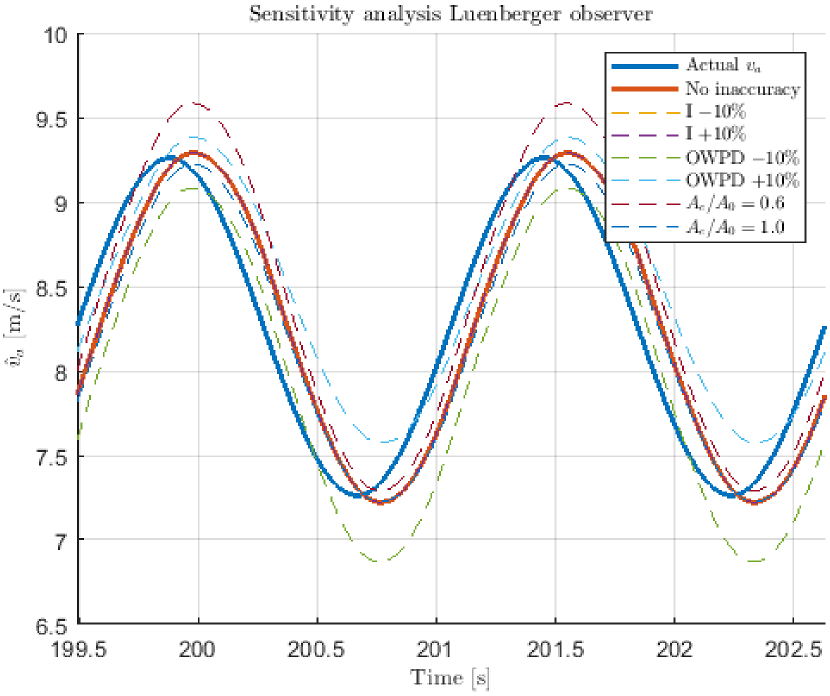

Figure A-24: Advance Velocity estimated by Luenberger Observer with moderate gains with different inaccuracies

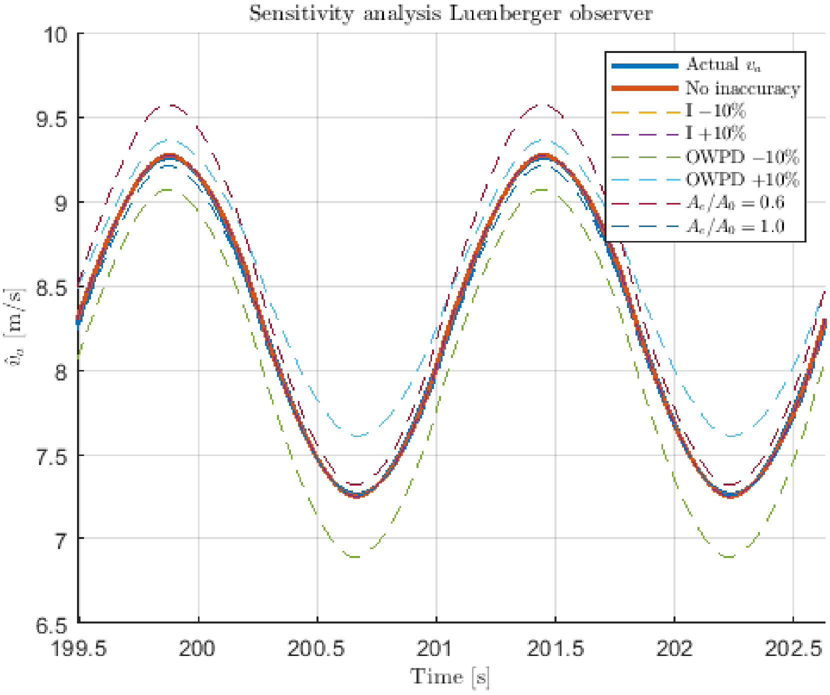

Figure A-25: Advance Velocity estimated by Luenberger Observer with high gains with different inaccuracies

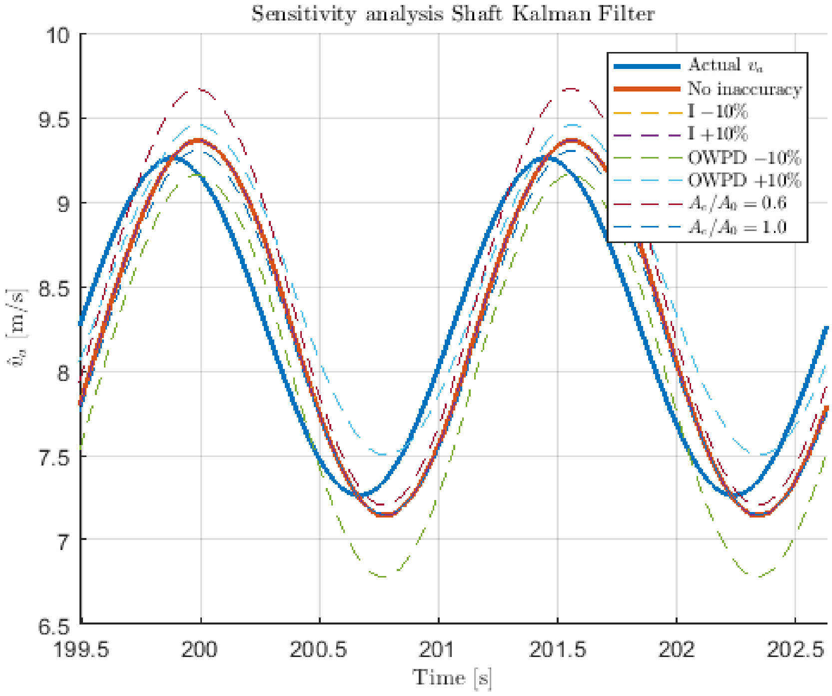

Figure A-26: Advance Velocity estimated by Shaft Kalman Filter with different inaccuracies

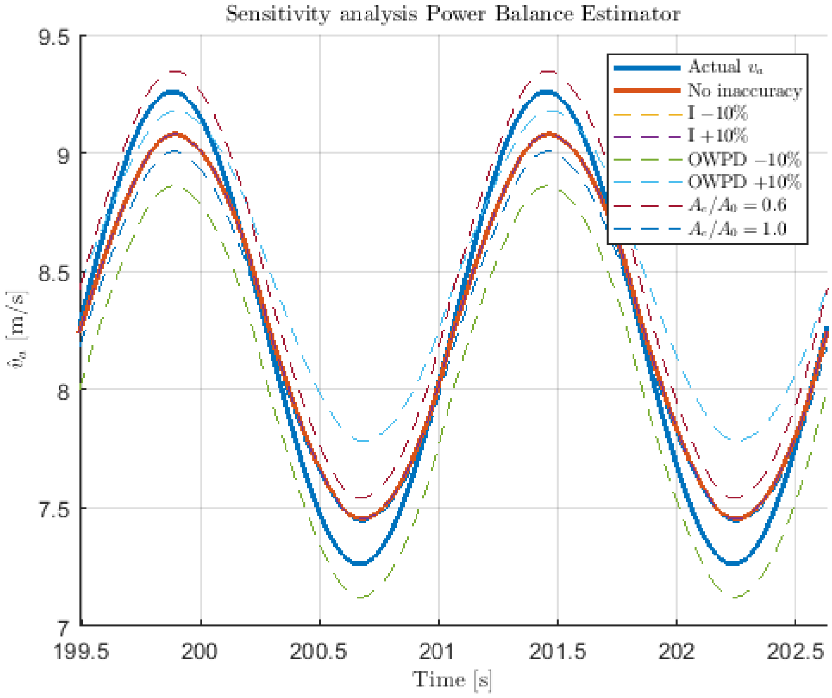

Figure A-27: Advance Velocity estimated by Power Balance Estimator with different inaccuracies

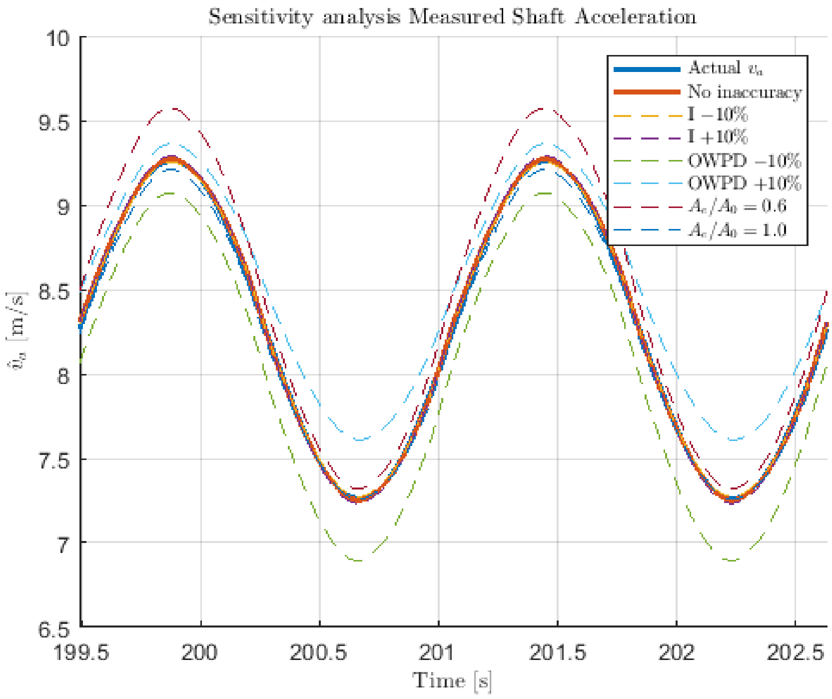

Figure A-28: Advance Velocity estimated by Measured Shaft Acceleration Observer with different inaccuracies

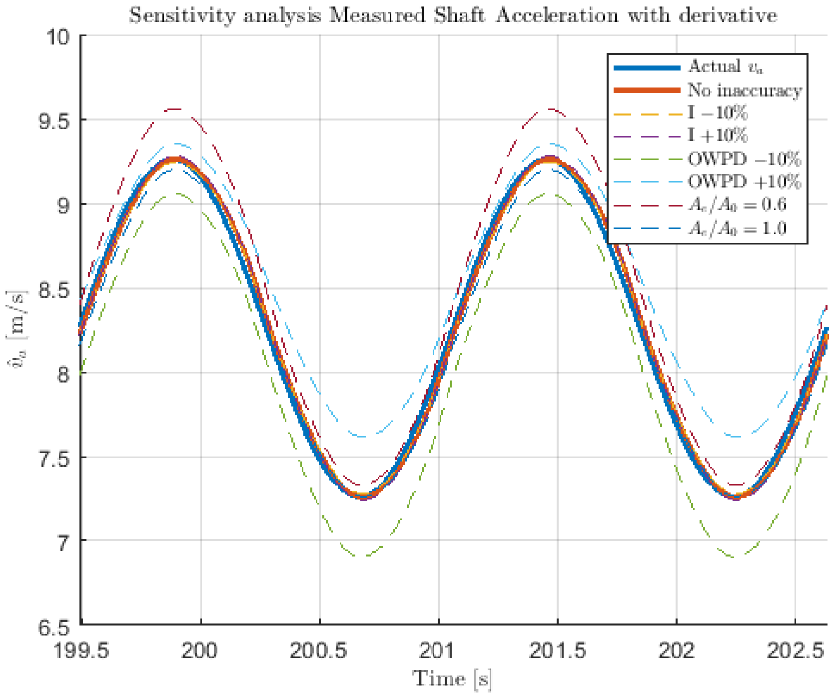

Figure A-29: Advance Velocity estimated by Measured Shaft Acceleration Observer without shaft acceleration measurement with different inaccuracies

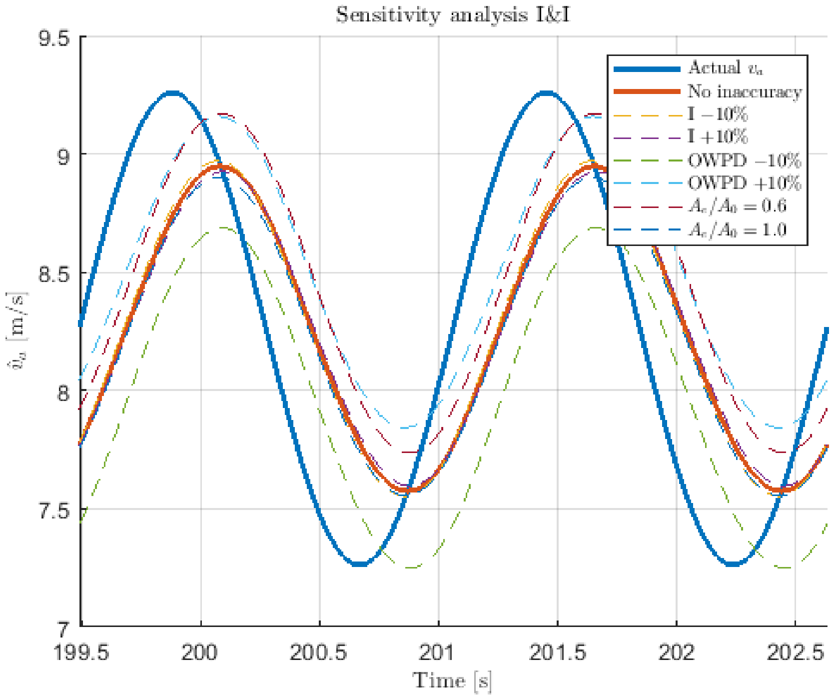

Figure A-30: Advance Velocity estimated by Immersion & Invariance Observer with $\gamma = 1$ with different inaccuracies

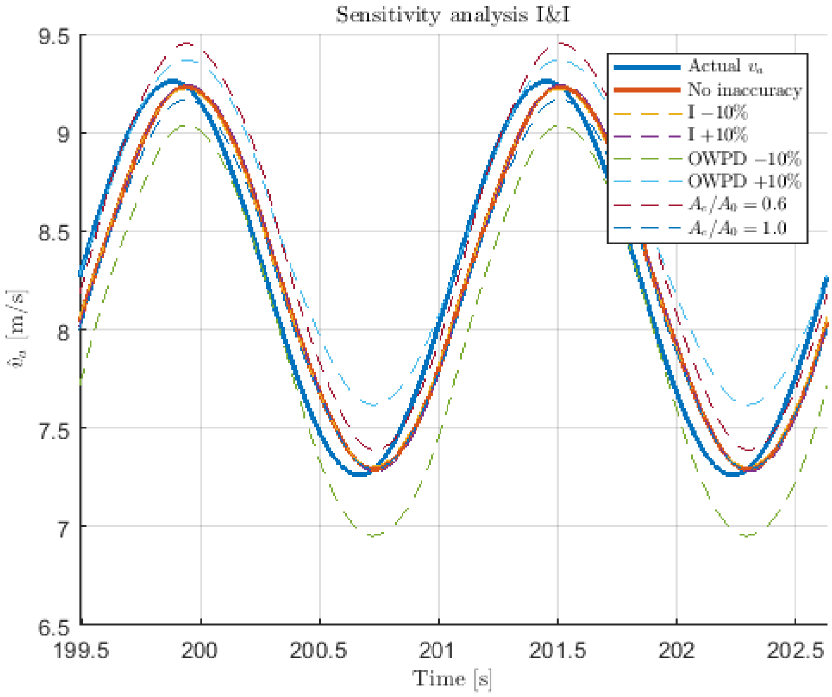

Figure A-31: Advance Velocity estimated by Immersion & Invariance Observer with $\gamma = 4$ with different inaccuracies

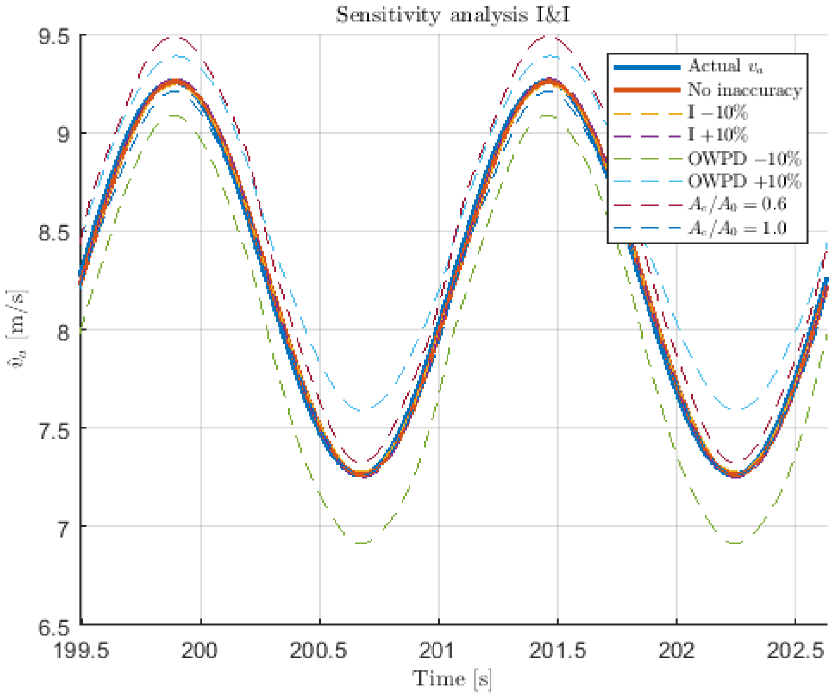

Figure A-32: Advance Velocity estimated by Immersion & Invariance Observer with $\gamma = 20$ with different inaccuracies

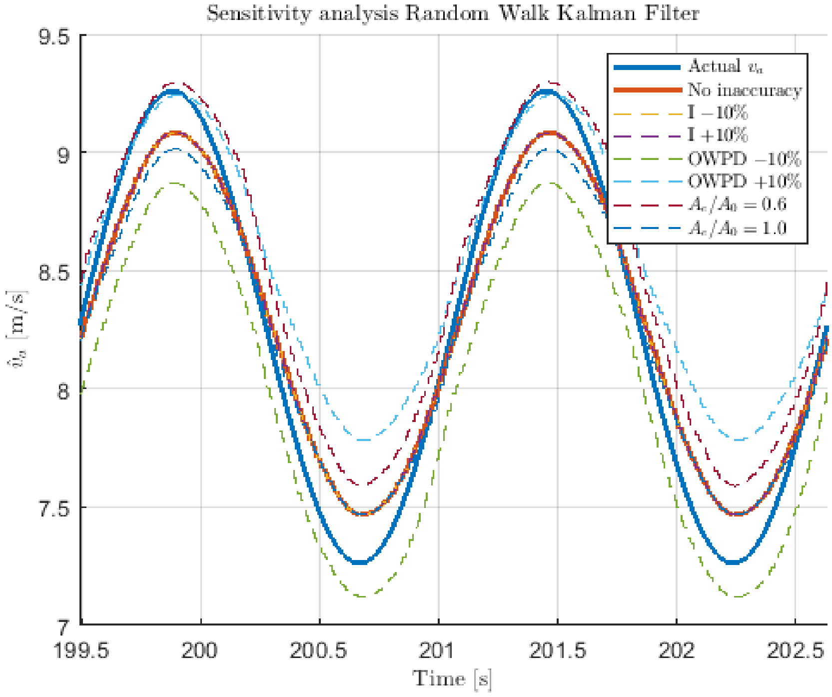

Figure A-33: Advance Velocity estimated by Random Walk Kalman Filter with different inaccuracies

Appendix B

Implementation

The choice was made to implement the ship propulsion model and the advance velocity observers in MATLAB R2018a in combination with SIMULINK. The ship propulsion model was implemented using S-functions in SIMULINK, to increase computational efficiency. The observers were also implemented in SIMULINK using a combination of S-functions and other available SIMULINK blocks. Both were run using an m-file in MATLAB. The following system parameters were used:

Table B-1: List of system parameters and their values

Parameter	Value	Unit
ρ	1025	$kg\ m^{-3}$
a	-45.5	$N\ m\ s\ rad^{-1}$
b	1428.6	$N\ m\ mm^{-1}$
c	-7381	$N\ m$
η_r	1	$-$
η_{trm}	0.95	$-$
τ_p	2	s
c_1	$3.3062 \cdot 10^3$	$-$
D	4.2	m
I_L	53697	$kg\ m^2$
I_R	14411	$kg\ m^2$
I	68108	$kg\ m^2$
i_{gb}	7.38	$-$
k_p	2	$-$
m_s	$3.3 \cdot 10^6$	kg
t	0.07	$-$
w	0.05	$-$

Bibliography

[1] A. Vrijdag and D. Stapersma, “Extension and application of a linearised ship propulsion system model,” *Ocean Engineering*, vol. 143, pp. 50–65, 2017.

[2] D. Stapersma, P. Schulten, and H. Grimmelius, “A fresh view on propulsion control,” in *Proceedings of the 7th international naval engineering conference. Amsterdam, The Netherlands*, pp. 221–40, 2004.

[3] A. Brevik, “Optimal kontrol av kontrollerbar pitch propell,” Master’s thesis, NTNU, 2016.

[4] Ø. N. Smogeli, “Control of marine propellers: from normal to extreme conditions,” 2006.

[5] O. Smogeli, J. Hansen, A. Serensen, and T. A. Johansen, “Anti-spin control for marine propulsion systems,” in *2004 43rd IEEE Conference on Decision and Control (CDC)(IEEE Cat. No. 04CH37601)*, vol. 5, pp. 5348–5353, IEEE, 2004.

[6] J. Bakkeheim, L. Pivano, T. A. Johansen, and Ø. N. Smogeli, “Integrator reset anti-spin for marine thrusters operating in four-quadrants and extreme sea conditions,” *IFAC Proceedings Volumes*, vol. 40, no. 17, pp. 205–210, 2007.

[7] L. Pivano, T. A. Johansen, and Ø. N. Smogeli, “A four-quadrant thrust controller for marine propellers with loss estimation and anti-spin: theory and experiments,” *Marine Technology*, vol. 46, no. 4, pp. 229–242, 2009.

[8] J. Bakkeheim, T. A. Johansen, Ø. N. Smogeli, and A. J. Sorensen, “Lyapunov-based integrator resetting with application to marine thruster control,” *IEEE Transactions on Control Systems Technology*, vol. 16, no. 5, pp. 908–917, 2008.

[9] F. Dullens *et al.*, “Modeling and control of a controllable pitch propeller,” *Technische Universiteit Eindhoven Department Mechanical Engineering Dynamics and Control Group*, 2009.

[10] A. Vrijdag, D. Stapersma, and T. Van Terwisga, “Control of propeller cavitation in operational conditions,” *Journal of Marine Engineering & Technology*, vol. 9, no. 1, pp. 15–26, 2010.

[11] R. Geertsma, R. Negenborn, K. Visser, M. Loonstijn, and J. Hopman, “Pitch control for ships with diesel mechanical and hybrid propulsion: Modelling, validation and performance quantification,” *Applied energy*, vol. 206, pp. 1609–1631, 2017.

[12] R. Geertsma, K. Visser, and R. Negenborn, “Adaptive pitch control for ships with diesel mechanical and hybrid propulsion,” *Applied energy*, vol. 228, pp. 2490–2509, 2018.

[13] L. L. Whitcomb and D. R. Yoerger, “Preliminary experiments in model-based thruster control for underwater vehicle positioning,” *IEEE Journal of Oceanic Engineering*, vol. 24, no. 4, pp. 495–506, 1999.

[14] Ø. N. Smogeli and A. J. Sørensen, “Adaptive observer design for a marine propeller,” *IFAC Proceedings Volumes*, vol. 39, no. 1, pp. 326–331, 2006.

[15] C. Guibert, E. Foulon, N. Aït-Ahmed, and L. Loron, “Thrust control of electric marine thrusters,” in *31st Annual Conference of IEEE Industrial Electronics Society, 2005. IECON 2005.*, pp. 6–pp, IEEE, 2005.

[16] K. Z. Østergaard, P. Brath, and J. Stoustrup, “Estimation of effective wind speed,” 2007.

[17] M. N. Soltani, T. Knudsen, M. Svenstrup, R. Wisniewski, P. Brath, R. Ortega, and K. Johnson, “Estimation of rotor effective wind speed: A comparison,” *IEEE Transactions on Control Systems Technology*, vol. 21, no. 4, pp. 1155–1167, 2013.

[18] R. Ortega, F. Mancilla-David, and F. Jaramillo, “A globally convergent wind speed estimator for wind turbine systems,” *International Journal of Adaptive Control and Signal Processing*, vol. 27, no. 5, pp. 413–425, 2013.

[19] K. Selvam, S. Kanev, J. W. van Wingerden, T. van Engelen, and M. Verhaegen, “Feedback–feedforward individual pitch control for wind turbine load reduction,” *International Journal of Robust and Nonlinear Control: IFAC-Affiliated Journal*, vol. 19, no. 1, pp. 72–91, 2009.

[20] D. Stapersma and A. Vrijdag, “Linearisation of a ship propulsion system model,” *Ocean Engineering*, vol. 142, pp. 441–457, 2017.

[21] M. Figari and M. Altosole, “Dynamic behaviour and stability of marine propulsion systems,” *Proceedings of the Institution of Mechanical Engineers, Part M: Journal of Engineering for the Maritime Environment*, vol. 221, no. 4, pp. 187–205, 2007.

[22] A. Vrijdag and D. Schuttevaer, “A systems and control approach to propeler cavitation in a seaway,” 2018.

[23] M. Altosole and M. Figari, “Effective simple methods for numerical modelling of marine engines in ship propulsion control systems design,” *Journal of Naval Architecture and Marine Engineering*, vol. 8, no. 2, pp. 129–147, 2011.

[24] P. Kidd, N. Munro, C. Thiruarooran, and D. Winterbone, “Linear modelling of ship propulsion plants,” *Proceedings of the Institution of Mechanical Engineers, Part A: Power and Process Engineering*, vol. 199, no. 1, pp. 53–58, 1985.

[25] D. Stapersma, “Interaction between propulsor and engine,” in *Proceedings of the 34th WEGEMT School "Developments in the Design of Propulsors and Propulsion Systems"*, 2000.

[26] T. I. Fossen and M. Blanke, “Nonlinear output feedback control of underwater vehicle propellers using feedback form estimated axial flow velocity,” *IEEE Journal of oceanic Engineering*, vol. 25, no. 2, pp. 241–255, 2000.

[27] A. Vrijdag and Y. Sang, “Fingerprinting the ship propulsion system: low hanging fruit or mission impossible?,” 2018.

[28] M. Verhaegen and V. Verdult, *Filtering and System Identification*. Cambridge University Press, 2007.

[29] T. Pérez and M. Blanke, “Simulation of ship motion in seaway,” *Department of Electrical and Computer Engineering, The University of Newcastle, Australia, Tech. Rep. EE02037*, 2002.

Glossary

List of Acronyms

3mE	Mechanical, Maritime and Materials Engineering
CPP	Controllable Pitch Propeller
DCSC	Delft Center for Systems and Control
EAR	Expanded Area Ratio
FPP	Fixed Pitch Propeller
I&I	Immersion and Invariance
IOWPD	Inverse Open Water Propeller Diagrams
MSA	Measured Shaft Acceleration
M&TT	Maritime and Transport Technology
OWPD	Open Water Propeller Diagrams
PBE	Power Balance Estimator
RMS	Root Mean Square
RWKF	Random Walk Kalman Filter
SD	Standard Deviation
SKF	Shaft Kalman Filter
SNR	Signal to Noise Ratio
VAF	Variance Accounted For

List of Symbols

η	Efficiency [$-$]
γ	I&I gain [$-$]
ω	Shaft speed [$rad\ s^{-1}$]
ρ	Density of water [$kg\ m^{-3}$]
τ_p	Pitch actuator time constant [s]
ζ	Scaled shaft speed [$rad\ s^{-1}$]
$^P/_D$	Propeller pitch ratio [$-$]
$^P/_{D_d}$	Desired pitch ratio [$-$]
a	Engine constant [$N\ m\ s\ rad^{-1}$]
b	Engine constant [$N\ m\ mm^{-1}$]
c	Engine constant [$N\ m$]
c_1	Quadratic resistance coefficient [$-$]
D	Propeller diameter [m]
d_{c_1}	Ship resistance disturbance [$-$]
F_p	Propeller thrust [N]
I	Propeller shaft rotational moment of inertia [$kg\ m^2$]
i	Ratio [$-$]
J	Advance ratio [$-$]
k_p	Number of propellers [$-$]
K_Q	Propeller torque coefficient [$-$]
K_T	Propeller thrust coefficient [$-$]
M	Torque [$N\ m$]
m_s	Ship mass [kg]
Q	Kalman Filter Process Noise Covariance [$-$]
Q	Open water torque [$N\ m^{-1}$]
R	Kalman Filter Output Noise Covariance [$-$]
R	Ship resistance [N]
T	Open water thrust [N]
t	Thrust deduction factor [$-$]
u_x	Advance velocity disturbance [$m\ s^{-1}$]
v_a	Advance velocity [$m\ s^{-1}$]
v_s	Ship speed [$m\ s^{-1}$]
w	Wake fraction [$-$]
w_{M_p}	Zero-mean white noise [$-$]
X	Fuel rack position [mm]
$_\Delta$	Linearized
$_B$	Brake

eq	Equilibrium
e	Engine
gb	Gearbox
L	Left
m	Measured
p	Propeller
R	Right
trm	Transmission
$\wedge$	Estimated